COUPLED HYDROMECHANICAL ANALYSIS IN THE PRESENCE OF DISCONTINUITIES

COUPLED HYDROMECHANICAL ANALYSIS IN THE PRESENCE OF DISCONTINUITIES

BY

AMIR ARSALAN JAMEEI, M.S.

A THESIS

SUBMITTED TO THE DEPARTMENT OF CIVIL ENGINEERING

AND THE SCHOOL OF GRADUATE STUDIES

OF MCMASTER UNIVERSITY

IN PARTIAL FULFILMENT OF THE REQUIREMENTS

FOR THE DEGREE OF

DOCTOR OF PHILOSOPHY

Doctor of Philosophy (2022) McMaster University

(Civil Engineering) Hamilton, Ontario, Canada

TITLE:	Coupled Hydromechanical Analysis in the Presence of Discontinuities
AUTHOR:	Amir Arsalan Jameei M.S. (Civil Engineering), University of Guilan, Iran B.S. (Civil Engineering), University of Guilan, Iran
SUPERVISOR:	Professor Stanislaw Pietruszczak
NUMBER OF PAGES:	xvi, 132

Preface

This Ph.D. thesis is an integrated article thesis composed of five main chapters, all dealing with the coupled hydromechanical analysis in the presence of discontinuities. The thesis incorporates three distinct journal papers provided in chapters 2-4. In what follows, a brief overview of the material that is covered in each chapter is provided, followed by details of the cooperation between authors of each paper.

Chapter 1 presents a review on the hydromechanical analysis of deformable solids in the presence of discontinuities and provides a discussion on the motivation, objectives, and research plan of this thesis.

Chapter 2 presents an article on the development of a new constitutive law with embedded discontinuity for the coupled hydromechanical analysis of fractured porous media. The article is published in *International Journal for Numerical and Analytical Methods in Geomechanics*. A.A. Jameei and Dr. S. Pietruszczak developed the formulation used in this paper and A.A. Jameei implemented it in the FE simulations. The article was drafted by A.A. Jameei and revised and finalized by Dr. Pietruszczak.

Chapter 3 presents an article on the evolution of flow characteristics during the propagation of localized damages in rocks. The article is published in *Minerals, Special Issue: The Hydro-mechanics of Crystalline Rocks*. A.A. Jameei derived the evolution law for hydraulic conductivity and developed the FE code to perform the simulations. The article was drafted by A.A. Jameei. The research developments were supervised

by Dr. S. Pietruszczak who revised and submitted the final manuscript.

Chapter 4 presents an article on the development of a consistent CLED-FE approach to study the hydromechanical coupling and shear band evolution of sparsely fractured rocks. The article is submitted to a peer reviewed journal. A.A. Jameei developed the FE framework and implemented it to perform the simulations. The article was drafted by A.A. Jameei. The research developments were supervised by Dr. S. Pietruszczak who revised and submitted the final manuscript.

Chapter 5 summarizes the main conclusions of the thesis, outlines the strength and limitations of the proposed approach, and provides some suggestions for future work.

Abstract

In this thesis, a new continuum framework for the coupled hydromechanical analysis of fractured porous media is proposed. This formulation represents an extension of the constitutive law with embedded discontinuity (CLED) for the assessment of both hydraulic and mechanical properties in the regions intercepted by discontinuities. The constitutive relations governing the hydromechanical response are derived by averaging the fluid pressure gradient and the discontinuous displacement fields over a selected referential volume of the material, subject to some physical constraints. Within this approach, an internal length scale parameter is employed in the definition of the equivalent hydraulic conductivity as well as the tangential stiffness operators. An evolution law is derived governing the variation of hydraulic conductivity with continuing deformation in order to explicitly account for the hydromechanical coupling. The governing field equations are formulated following the general form of balance equations in the superimposed interacting continua. An enhanced mixed u-p finite element formulation is presented which considers the effect of progressive evolution of the fracture aperture in the weak statements of balance equations. Fully implicit temporal discretization is employed, and the finite element formulation is stabilized by invoking the Polynomial-Pressure-Projection (PPP) technique. The proposed methodology is verified by a comprehensive numerical study dealing with a steady-state flow through fractured media, time-dependent consolidation in the presence of a discontinuity, 3D

simulation of an axial splitting test carried out on a saturated sample under displacement and fluid pressure-controlled conditions, and assessment of the evolution and coalescence of localized damage zones in sparsely fractured crystalline rocks. Both discrete and smeared damage tracing strategies have been employed. For the discrete damage tracing in the compression regime, the bifurcation analysis has been carried out. A comprehensive CLED-FE code based on the proposed approach, and an analogous IE-FE code, have been developed for the coupled hydromechanical analysis of porous media.

To those fighting for their right to dissent

Acknowledgements

I would like to express my deepest gratitude to my esteemed supervisor and mentor, Dr. Stanislaw Pietruszczak for his guidance, encouragement, and dedicated support throughout my doctoral studies. His vast years of experience, extensive knowledge in Computational Mechanics, and sharp vision formed the basis of this thesis. In addition, this research would have not been possible without the invaluable feedback from my dedicated committee members. I would like to thank Dr. Peijun Guo for his constructive comments and our conversations which greatly expanded my knowledge and influenced my research. I would also like to thank Dr. Chidiac for his fruitful comments and many useful scholarly discussions we had during my studies.

I am also extremely thankful to my former supervisor, Dr. Mehdi Veiskarami for his treasured support and advice. My gratitude also goes to my family, Roya Vahedi, Aida Jameei, Alaleh Jameei, and Mohsen Sarikhani for their unconditional love, motivation, and endless patience. A special thank you to my partner, Kavindya Weeratunga, who has been instrumental in the completion of my Ph.D. studies through her unwavering love, belief, and encouragement. Finally, I would like to thank my peers and closest friends who have positively shaped my doctoral career and supported me through all the highs and lows of this journey: Roham Akbarian, Niloufar Khodaei, Nikrouz Bahadormanesh, Pardis Mohammadpour, Shahryar Asqardoust, Amin Halali, Hojjat Mohammadi, Kianoosh Koocheki, Pouria Sarbazi, and Sina Moallemi.

Contents

List of Figures

List of Tables

Chapter 1

Introduction

This Ph.D. thesis presents a new approach for dealing with discontinuities in the fluid-infiltrated porous media. The thesis is prepared in an integrated-article format and includes three distinct journal papers in support of developing the current approach. In what follows, the motivation behind this research is provided followed by some general comments on the scope of this work.

1.1 Background and motivation

Porous media including biological tissues, concrete, soils and rock masses are, in general, multiphase materials consisting of solid skeleton infiltrated by fluid(s). Classical/rational mechanics, as named by Clifford Truesdell [1], is a branch of physics which puts together the fundamental mathematical principles for the study of mechanical behaviour of multiphase materials. In the classical mechanics, the multiphase materials are considered as superimposed interacting continua composed of immiscible mixtures (phases). In this case, the field equations of the conservation of mass, linear momentum, and moment of linear momentum hold for every phase/constituent

with explicit indication of the interaction of different phases with each other [2,3,4]. The notion of interacting continua in conjunction with the concept of volume fraction (ref. [5,6]) creates the commonly known theory of porous media [7,8,9,10,11,12]. The theory of porous media lays the foundation for the coupled hydromechanical analysis.

Despite its importance, the effect of discontinuities on the coupled hydromechanical analysis has received little attention. In general, the hydraulic conductivity along fractures or discontinuities is quite different from that in the intact region, which affects not only the flow pattern but also the strength and deformability at the structural level. This is of importance in a broad range of practical engineering problems which include those related to deep geological nuclear and hazardous waste repositories, enhancement of hydrocarbon recovery production, carbon sequestration and methane extraction from soft soils/coal beds, geothermal energy applications, etc.

In general, classical continuum mechanics suffers from inability to deal with discontinuities and localized deformation in the context of a boundary value problem. Discontinuities in the form of macrocracks exhibit strain softening response, and their geometry as well as dimensions drastically affect the deformation characteristics at the structural level. In this case, the numerical solution becomes systemically sensitive to discretization. This is due to the fact that continuum mechanics does not incorporate any internal length scale since the constitutive equations are formulated based on Noll's principle of local action [13]. In order to address the problem, the nonlocal theories have been developed which incorporate a 'characteristic dimension'. Unfortunately, the definition of this parameter is rather ambiguous and has no explicit relation to the material properties [14,15,16]. An alternative way of dealing with abrupt changes in the field variables is the use of Cosserat mechanics [17,18,19]. The Cosserat mechanics is an advanced micropolar framework of continuum mechanics where the stress tensor is nonsymmetric due to the use of couple stresses. The

primary difficulty in the use of Cosserat continuum is the identification of additional material parameters that stem from the notion of non-symmetry of the stress tensor. Another approach involves the use of interface elements, which require discretization that conforms to the geometry of fractures/localized damage [20,21,22,23]. Conformity of the finite element mesh to the geometry of discontinuity is a necessity in this technique since discontinuities are positioned at edges which are shared between two neighboring elements, and additional degrees of freedom are considered at the nodal points of those edges. In this approach, the strain-softening behaviour along discontinuities can be explicitly addressed; however, tracing the crack propagation process is not accurate and requires progressive remeshing strategies or restricting the propagation directions based on the mesh configuration. Other commonly used approach is the extended finite element method (XFEM), which incorporates enriched approximation functions based on the partition-of-unity property of finite elements [24,25,26]. Although reliable, this approach is computationally not very efficient as it employs additional degrees of freedom and requires special integration techniques.

An alternative strategy (for the single-phase solids), which does not require any additional degrees of freedom, is the incorporation of a constitutive law with embedded discontinuity (CLED) [27,28]. In this case, in a reference volume encompassing the fracture zone, the discontinuous velocity gradient is averaged subject to the constraint of continuity of traction vector. The formulation accounts for strain-softening response in the fractured zone and the macroscopic fourth-order stiffness tensor is a function of the properties of constituents as well as an internal length scale parameter, the latter defined as the ratio of the considered referential volume to the surface area of discontinuity.

The CLED methodology has been used so far in the context of the description of propagation of localized damage in a single-phase solid [29,30,31]. In this thesis, this

methodology is extended to describe the coupled hydromechanical interaction in fluid-infiltrated porous media containing fractures/discontinuities. The proposed approach is very efficient in terms of computational costs as well as implementation in finite element analyses, as compared to other existing methodologies. For the description of fluid flow in the presence of discontinuities, an enhanced Darcy's law incorporating an equivalent hydraulic conductivity is introduced, which also employs an internal length scale. In addition, an evolution law is formulated which describes the variation of equivalent hydraulic conductivity with the continuing deformation. Within the current approach, a consistent finite element formulation is derived that considers a progressive evolution of both the mechanical and hydraulic properties associated with propagation of localized damage. This formulation does not require the use of conformal meshes since the effect of discontinuity is embedded in the constitutive relations. Moreover, the onset and propagation of new macrocracks/fractures can be modeled without the need for either remeshing or refining the mesh (similar to XFEM).

1.2 General scope

As mentioned earlier, this thesis contains three distinct journal papers integrated in the body of this work and forming Chapters 2-4. In what follows, a brief overview of each of these chapters is presented.

In chapter 2, the CLED approach for the coupled hydromechanical analysis of fractured porous media is presented. This approach is developed in the context of finite element analysis of saturated porous media. The proposed methodology is verified by a set of numerical examples dealing with a steady-state flow through fractured media and a time-dependent consolidation in the presence of a discontinuity.

In chapter 3, a mathematical formulation is presented which incorporates the hydromechanical interactions associated with propagation of localized damages. The framework is verified by a numerical study involving the 3D FE simulation of an axial splitting test carried out on a saturated sample under displacement and fluid pressure-controlled conditions. The finite element analysis incorporates the Polynomial-Pressure-Projection (PPP) stabilization technique and a fully implicit time integration scheme.

In chapter 4, the evolution and coalescence of localized damage zones in sparsely fractured crystalline rocks are studied by using the developed hydromechanical CLED approach. In this study, an enhanced mixed u-p finite element formulation is developed which considers the effect of progressive evolution of the fracture aperture in the weak statements of balance equations. The response of Luc du Bonnet granite is studied using the current formulation. The analyzed sample contains a pre-existing fracture network which evolves due to formation of new coalesced macrocracks. Initiation of new macrocracks is detected by conducting bifurcation analysis. The current numerical scheme is first verified on some benchmark problems that involve the presence of a dominant fracture. The results of simulations are compared with those obtained using a very fine mesh incorporating interface elements. Later, a series of coupled analyses are carried out examining the hydromechanical response in the presence of multiple fractures.

Chapter 5 summarizes the main conclusions of this thesis and provides suggestions for potential future work pivoted around the current subject.

It should be noted that the numerical examples presented in this thesis are solved by using a CLED u-p finite element code that has been developed entirely in MATLAB by the author of this thesis

References

[1] C. Truesdell and R. Toupin, "The classical field theories," in *Principles of Classical Mechanics and Field Theory/Prinzipien der Klassischen Mechanik und Feldtheorie*, pp. 226–858, Springer, 1960.

[2] C. Truesdell and R. Toupin, "Sulle basi della termomeccanica," *Rend Linc.*, vol. 22, pp. 158–166, 1957.

[3] A. E. Green and P. M. Naghdi, "A theory of mixtures," *Archive for Rational Mechanics and Analysis*, vol. 24, no. 4, pp. 243–263, 1967.

[4] A. E. Green and P. M. Naghdi, "On basic equations for mixtures," *The Quarterly Journal of Mechanics and Applied Mathematics*, vol. 22, no. 4, pp. 427–438, 1969.

[5] L. Morland, "A simple constitutive theory for a fluid-saturated porous solid," *Journal of Geophysical Research*, vol. 77, no. 5, pp. 890–900, 1972.

[6] R. M. Bowen, "Theory of mixtures," in *Eringen AC, ed. Continuum Physics. Volume III—Mixtures and EM Field Theories. London: Academic Press*, pp. 1–127, 1976.

[7] R. M. Bowen, "Incompressible porous media models by use of the theory of mixtures," *International Journal of Engineering Science*, vol. 18, no. 9, pp. 1129–1148, 1980.

[8] R. M. Bowen, "Compressible porous media models by use of the theory of mixtures," *International Journal of Engineering Science*, vol. 20, no. 6, pp. 697–735, 1982.

[9] M. A. Biot, "General theory of three-dimensional consolidation," *Journal of Applied Physics*, vol. 12, no. 2, pp. 155–164, 1941.

[10] K. Terzaghi, *Erdbaumechanik auf bodenphysikalischer Grundlage*. Leipzig, Wien: F. Deuticke, 1925.

[11] P. Fillunger, *Erdbaumechanik?* Wien: Selbstverlag des Verfassers, 1936.

[12] R. de Boer, *Theory of Porous Media*. Berlin: Springer-Verlag, 2000.

[13] W. Noll, "A mathematical theory of the mechanical behavior of continuous media," in *Archive for Rational Mechanics and Analysis*, vol. 2, pp. 197–226, 1958.

[14] A. C. Eringen, *Microcontinuum Field Theories: I. Foundations and Solids*. Springer Science & Business Media, 2012.

[15] J. L. Mroginski, G. Etse, and S. M. Vrech, "A thermodynamical gradient theory for deformation and strain localization of porous media," *International Journal of Plasticity*, vol. 27, no. 4, pp. 620–634, 2011.

[16] M. E. Mobasher, L. Berger-Vergiat, and H. Waisman, "Non-local formulation for transport and damage in porous media," *Computer Methods in Applied Mechanics and Engineering*, vol. 324, pp. 654–688, 2017.

[17] H.-B. Mühlhaus and I. Vardoulakis, "The thickness of shear bands in granular materials," *Geotechnique*, vol. 37, no. 3, pp. 271–283, 1987.

[18] W. Ehlers and W. Volk, "On theoretical and numerical methods in the theory of porous media based on polar and non-polar elasto-plastic solid materials," *International Journal of Solids and Structures*, vol. 35, no. 34-35, pp. 4597–4617, 1998.

[19] H. Rattez, I. Stefanou, J. Sulem, M. Veveakis, and T. Poulet, "Numerical analysis of strain localization in rocks with thermo-hydro-mechanical couplings using cosserat continuum," *Rock Mechanics and Rock Engineering*, vol. 51, no. 10, pp. 3295–3311, 2018.

[20] R. E. Goodman, R. L. Taylor, and T. L. Brekke, "A model for the mechanics of jointed rock," *Journal of the Soil Mechanics and Foundations Division, Proceedings of ASCE*, vol. 94, no. 3, pp. 637–659, 1968.

[21] J. Ghaboussi, E. L. Wilson, and J. Isenberg, "Finite element for rock joints and interfaces," *Journal of the Soil Mechanics and Foundations Division*, vol. 99, no. 10, pp. 833–848, 1973.

[22] M. C. Lobao, R. Eve, D. Owen, and E. A. de Souza Neto, "Modelling of hydrofracture flow in porous media," *Engineering Computations*, 2010.

[23] P. Fu, S. M. Johnson, and C. R. Carrigan, "An explicitly coupled hydro-geomechanical model for simulating hydraulic fracturing in arbitrary discrete fracture networks," *International Journal for Numerical and Analytical Methods in Geomechanics*, vol. 37, no. 14, pp. 2278–2300, 2013.

[24] N. Moës, J. Dolbow, and T. Belytschko, "A finite element method for crack growth without remeshing," *International Journal for Numerical Methods in Engineering*, vol. 46, no. 1, pp. 131–150, 1999.

[25] M. Luege, J. Lucero, C. Torrijos, and A. Orlando, "Coupled mechanical and fluid flow analysis in fractured saturated porous media using the xfem," *Applied Mathematical Modelling*, vol. 40, no. 7-8, pp. 4480–4504, 2016.

[26] E. Mikaeili and B. Schrefler, "XFEM, strong discontinuities and second-order

work in shear band modeling of saturated porous media," *Acta Geotechnica*, vol. 13, no. 6, pp. 1249–1264, 2018.

[27] S. Pietruszczak and Z. Mróz, "Finite element analysis of deformation of strain-softening materials," *International Journal for Numerical Methods in Engineering*, vol. 17, no. 3, pp. 327–334, 1981.

[28] S. Pietruszczak, "On homogeneous and localized deformation in water-infiltrated soils," *International Journal of Damage Mechanics*, vol. 8, no. 3, pp. 233–253, 1999.

[29] S. Pietruszczak and Z. Mróz, "Finite element analysis of deformation of strain-softening materials," *International Journal for Numerical Methods in Engineering*, vol. 17, no. 3, pp. 327–334, 1981.

[30] E. Haghighat and S. Pietruszczak, "On modeling of discrete propagation of localized damage in cohesive-frictional materials," *International Journal for Numerical and Analytical Methods in Geomechanics*, vol. 39, no. 16, pp. 1774–1790, 2015.

[31] S. Moallemi, S. Pietruszczak, and Z. Mróz, "Deterministic size effect in concrete structures with account for chemo-mechanical loading," *Computers & Structures*, vol. 182, pp. 74–86, 2017.

Chapter 2

Embedded discontinuity approach for coupled hydromechanical analysis of fractured porous media

A. A. Jameei and S. Pietruszczak, "Embedded discontinuity approach for coupled hydromechanical analysis of fractured porous media," *International Journal for Numerical and Analytical Methods in Geomechanics*, vol. 44, no. 14, pp. 1880–1902, 2020.

Embedded discontinuity approach for coupled hydromechanical analysis of fractured porous media

A. A. Jameei and S. Pietruszczak

Department of Civil Engineering, McMaster University, Hamilton, Ontario, Canada

Summary: In this paper, a new continuum approach for the coupled hydromechanical analysis of fractured porous media is proposed. The methodology for describing the hydraulic characteristics invokes an enriched form of Darcy's law formulated in the presence of an embedded discontinuity. The constitutive relations governing the hydromechanical response are derived by averaging the fluid pressure gradient and the discontinuous displacement fields over a selected referential volume of the material, subject to some physical constraints. The framework incorporates an internal length scale which is explicitly embedded in the definition of gradient operators. The respective field equations are derived following the general form of balance equations in interacting continua. The conventional finite element method is then employed for the spatial discretization, and the generalized Newmark scheme is used for the temporal discretization. The proposed methodology is verified by some numerical examples dealing with a steady-state flow through fractured media as well as a time-dependent consolidation in the presence of a discontinuity.

Keywords: constitutive law with embedded discontinuity, continuum approach, coupled hydromechanical analysis, discontinuity, finite element

2.1 Introduction

The mechanical and hydraulic behavior of a multiphase porous medium can be studied within the realm of continuum physics by examining the interaction between different constituents. As an example, the saturated geomaterials are two-phase media comprising the solid and liquid phases, whereas in unsaturated conditions the third phase, i.e. the air, is also present. The analysis is often conducted at the mesoscale level and incorporates a representative elementary volume (REV) with statistically distributed and superimposed constituents. In this case, any volume space within the domain may be considered as composed of interacting continua, and the physical response can be efficiently modeled using established mathematical representations [1]. The foundations of the theory of superimposed interacting continua, which is also called the (immiscible) mixture theory, were established by Truesdell [2,3] in the context of diffusion problems. The framework was then extensively used in various areas of multiphase mechanics [4,5,6,7,8], for example, chemically reacting continua [9] and electromagnetics [10]. For porous media, it was Fillunger [11] who first derived a simplified form of balance equations incorporating the mixture theory in the context of one-dimensional consolidation. The general framework developed by Truesdell stipulates that each superimposed continuum satisfies the basic governing field equations, i.e. equations representing laws of conservation of mass, momentum and spin momentum, and thermodynamic principles of balance of energy and entropy production (i.e., Clausius-Duhem inequality) [3,12]. In later developments, the concept of volume fraction was introduced (cf Morland [13] and Bowen [14]) in order to extend the applicability of this framework to poromechanics. The description incorporated the effect of porosity, which is an important parameter in the fluid(s)-infiltrated porous solids, by replacing the constituents by continua of reduced densities [15,16,17]. Consistent

continuum approaches for the study of porous media based on the mixture theory can be found, for example, in de Boer [1,18], Ehlers [19], and Borja [20]. An alternative approach to describe the hydromechanics of porous media was introduced by Biot [21], who extended Terzaghi's theory of one-dimensional consolidation [22]. The original approach was limited to the linear elastic porous solid undergoing infinitesimal deformation and Poiseuille type of fluid flow [21,23]. The theory was later extended to problems associated with viscoelasticity, anisotropy, and finite deformations [24,25]. Although the continuum approach of Biot is conceptually different from the mixture theory of Truesdell, the results obtained using both frameworks are quantitatively fairly similar [26].

The permeability of porous media stems primarily from the presence of interconnected void space. The coupling between the flow and deformation can be accounted for using one of the continuum frameworks as mentioned above. However, the porous skeleton may contain discontinuities in the form of fractures, preexisting faults, and so forth, which will enhance the flow. An example of this is the localization of deformation into shear bands/macrocracks triggered by the local material instability [27,28]. In fact, the classical continuum mechanics can predict the onset of strain localization by invoking the bifurcation analysis [28,29]. However, this approach suffers from inability to describe the post-bifurcation behavior in the context of a boundary value problem. This is due to the fact that classical continuum mechanics does not incorporate any internal length scale because the constitutive equations are formulated based on Noll's principle of local action [12]. The strain localization is associated with the softening phenomenon. In this case, the lack of internal length scale leads to a change in the nature of the governing differential equations and, as a result, the numerical solution becomes pathologically sensitive to the discretization. Different regularization

techniques have been proposed to remedy this problem, that is, to restore the well-posedness of the governing equations. Those include the theories of micromorphic [30,31], micropolar [32,33,34] continua, and the second gradient approaches [35,36]. A more in-depth review dealing with the notion of localization can be found in some of the references cited above. The present study is focused mainly on the description of flow in the presence of existing fracture networks. Therefore, the remaining literature review is limited to this specific topic. It should be pointed out, however, that the approach is also suitable for dealing with a hydromechanical coupling in the context of the onset and propagation of new fractures.

The hydraulic conductivity along preexisting discontinuities is quite different from that in the intact region, which affects not only the flow pattern but also the strength and the deformability at the structural level. This is of importance in a broad range of practical engineering problems, which include those of slope stability, gas and oil extractions from shales, construction of geological waste repositories, and aquifers remediation. One of the first attempts to study the mechanics of fractured fluid-infiltrated porous media was that by Aifantis et al [37,38] who used the concept of a double porosity [39]. The cracked region was modeled as a homogenized equivalent continuum whose interaction with the intact domain was described using the mixture theory. This methodology was similar to that introduced earlier by Barenblatt [40] for the analysis of transient flow in fissured rocks. In another study, Oda [41] examined the permeability of rock mass containing a fracture network. He introduced a stereology-based tensorial measure of joints geometry accounting for the aperture, size, and orientation of fractures. The eigenvectors of this second-order tensor were assumed to coincide with the principal directions of permeability. Recently, Azizmohammadi and Matthäi [42] conducted a study focused on the effect of scale on the permeability of the naturally fractured rocks. The approach employed the upscaling

technique developed by Durlofsky [43] for estimating the equivalent permeability tensor. In general, the above-mentioned approaches are limited to the case when the cracks are densely distributed over a scale which is large enough compared to the dimensions of individual cracks and, at the same time, small enough to be considered as a representative volume. However, in many practical problems, the cracks might not be densely distributed within the domain and the existence of isolated discontinuities needs to be considered. The study of hydromechanical interaction in the presence of discrete discontinuities is a challenging task and, over the years, different techniques have been proposed in the literature. For example, the fractures have been modeled via an integral (weak) form of the governing equations, which incorporates the discontinuity surfaces as additional physical boundaries with distinct mechanical and hydraulic properties [44]. Alternatively, interface elements have been employed along the discontinuity surfaces with appropriate kinematic constraints (e.g., discontinuity of displacement field and continuity of the fluid mass-exchange between fracture and intact regions) [45,46,47]. In both these techniques, spatial discretization must conform to the geometry of discontinuities, and mesh regeneration is required for the propagation problems as the direction of propagation is not known a priori [48]. Dependency on the mesh size and alignment can be limited by employing XFEM methodology. In XFEM, the approximation functions are enriched using the partition-of-unity property of finite elements [49]. This approach has been extensively used in modeling of hydromechanical interaction in fractured media as well as the problems of hydraulic fracturing [50,51,52]. For instance, de Borst et al [50] studied the shear band evolution in a fluid-saturated domain by enriching the fluid pressure field in a similar way to the enrichment of the displacement field. They used the Heaviside step function to impose the discontinuity in the fluid pressure and displacement fields across the fracture. In a later work, Réthoré et al [51] assumed a discontinuity in

the gradient of fluid pressure and used a two-scale micro-macro description. The up-scaling involved introducing a jump in flux (i.e., out of the balance equations of the viscous micro fluid in the cavity) into the macro-scale weak form equations. More recently, Vahab et al [52] also presented an energy-based computational framework using XFEM in the context of hydraulic fracturing. It should be pointed out that the XFEM approach, although reliable, is computationally not very efficient as it employs additional degrees of freedom and requires special integration techniques.

An alternative approach, which does not introduce any additional degrees of freedom, is the formulation of a constitutive relation which incorporates a "characteristic dimension" associated with the presence of discontinuity [53,54]. This approach has been referred to as a constitutive law with embedded discontinuity (CLED) [53]. The CLED methodology has been used so far in the context of description of propagation of localized damage in a single-phase solid [53,54,55,56,57]. In a reference volume encompassing the fracture band, the discontinuous velocity gradient is averaged subject to the constraint of continuity of traction vector. The formulation accounts for strain-softening response in the fracture zone, and the macroscopic fourth order stiffness tensor is a function of properties of constituents as well as an internal length scale parameter, the latter defined as the ratio of the considered referential volume to the surface area of discontinuity. The CLED approach has been employed in the context of discrete modeling of the damage propagation in brittle and frictional materials [55]. In that case, rather than using the original smeared approach of Pietruszczak and Mróz [53]. a level-set method was employed for discrete tracing of the propagation path. The same methodology has also been used in the study of the size effect in concrete structures with account for chemo-mechanical interaction [56] and, more recently, in the analysis of damage process in rocks with preexisting fractures [57].

The main objective in this paper is to extend the CLED approach to describe the hydromechanical interaction in fluid-infiltrated porous media. In order to achieve this, a weak discontinuity in fluid pressure as well as a strong discontinuity in displacement field is imposed across the region. Subject to admissible constraints in the flow pattern and continuity of tractions in the fractured region, an equivalent hydraulic conductivity and a macroscopic stiffness operator are defined, both incorporating a "characteristic dimension". The proposed methodology is verified by some numerical examples dealing with a steady-state flow through fractured media as well as a time-dependent consolidation in the presence of a discontinuity.

2.2 Constitutive relations for hydromechanical response in the presence of discontinuities

The approach incorporating a constitutive law with embedded discontinuity (CLED) invokes a homogenization procedure whereby the post-localization response is defined in terms of properties of constituents (i.e., the intact material and the fractured zone) and their geometric arrangement. As mentioned earlier, the CLED approach has been used so far for describing the mechanics of a single-phase (i.e., solid) medium. In this work, the methodology is extended to address the hydromechanical coupling in two-phase (i.e., fully saturated) porous media. In particular, an enriched form of Darcy's law is proposed governing the fluid flow in the presence of discontinuities (fractures) within the domain. The approach incorporates the classical notions of mixture theory, whereby the solid and fluid phases are assumed to be immiscible, and the governing equations employ the concept of porosity/volume fraction.

In order to formulate the problem, consider a referential volume $\Delta\Omega$, which includes the intact parts $\Delta\Omega^+$ and $\Delta\Omega^-$, intercepted by a fractured region of thickness t_d and the surface area $\Delta\Gamma_d$. The geometry of the problem is schematically illustrated in Figure 2.1a, where $\boldsymbol{s}$, $\boldsymbol{t}$, and $\boldsymbol{n}$ are the standard local basis vectors. The origin of the coordinate system is located in the center of the discontinuity region, whereas the unit normal $\boldsymbol{n}$ is directed towards to positive side of the intact part $\Delta\Omega^+$.

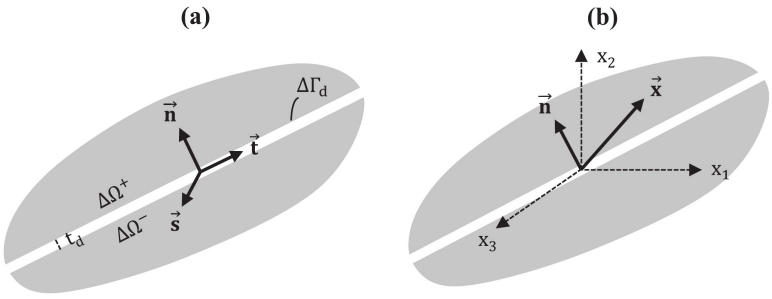

Figure 2.1: (a) Local Cartesian coordinate system attached to the discontinuity surface, (b) position vector and unit normal to the discontinuity surface

Consider now the case when there is a weak discontinuity in the fluid pressure. The latter involves an inhomogeneity in the pressure gradient such that its normal component is different in the intact and the fractured regions, whereas the tangential components remain the same. In this case, the gradient operator can be defined in terms of two continuous functions $\boldsymbol{\nabla}_{\boldsymbol{x}}\hat{p}$ and $\boldsymbol{\nabla}_{\boldsymbol{x}}\tilde{p}$, such that

$$\boldsymbol{\nabla}_{\boldsymbol{x}} p = \boldsymbol{\nabla}_{\boldsymbol{x}}\hat{p} + \Phi(\boldsymbol{x})(\boldsymbol{n}\cdot\boldsymbol{\nabla}_{\boldsymbol{x}}\tilde{p})\boldsymbol{n} \tag{2.1}$$

where $\boldsymbol{x}$ is an arbitrary position vector (Figure 2.1b) and $\Phi(\boldsymbol{x})$ is a piecewise scalar function defined as

$$\Phi(\boldsymbol{x}) = \begin{cases} 0 & \text{for} \quad \boldsymbol{x}\cdot\boldsymbol{n} > \dfrac{t_d}{2} \\ 1 & \text{for} \quad -\dfrac{t_d}{2} \le \boldsymbol{x}\cdot\boldsymbol{n} \le \dfrac{t_d}{2} \\ 0 & \text{for} \quad \boldsymbol{x}\cdot\boldsymbol{n} < -\dfrac{t_d}{2} \end{cases} \tag{2.2}$$

The significance of representation (2.1) is illustrated in Figure 2.1b. For points located in the intact subdomains (i.e., $\boldsymbol{x}\cdot\boldsymbol{n} > t_d/2$ or $\boldsymbol{x}\cdot\boldsymbol{n} < -t_d/2$), the gradient operator is $\boldsymbol{\nabla}_{\boldsymbol{x}}\hat{p}$, whereas in the discontinuity region (i.e., $-t_d/2 \le \boldsymbol{x}\cdot\boldsymbol{n} \le t_d/2$), it assumes the value $\boldsymbol{\nabla}_{\boldsymbol{x}}\hat{p} + (\boldsymbol{n}\cdot\boldsymbol{\nabla}_{\boldsymbol{x}}\tilde{p})\boldsymbol{n}$. Thus, Equation (2.1) can be expressed in an equivalent form

$$\boldsymbol{\nabla}_{\boldsymbol{x}} p^{(1)} = \boldsymbol{\nabla}_{\boldsymbol{x}}\hat{p} \quad \text{for} \quad \boldsymbol{x}\cdot\boldsymbol{n} > t_d/2 \quad \text{or} \quad \boldsymbol{x}\cdot\boldsymbol{n} < -t_d/2 \tag{2.3}$$

$$\boldsymbol{\nabla}_{\boldsymbol{x}} p^{(2)} = \boldsymbol{\nabla}_{\boldsymbol{x}} p^{(1)} + (\boldsymbol{n}\cdot\boldsymbol{\nabla}_{\boldsymbol{x}}\tilde{p})\boldsymbol{n} \quad \text{for} \quad -t_d/2 \le \boldsymbol{x}\cdot\boldsymbol{n} \le t_d/2 \tag{2.4}$$

where $\boldsymbol{\nabla}_{\boldsymbol{x}} p^{(1)}$ and $\boldsymbol{\nabla}_{\boldsymbol{x}} p^{(2)}$ are the pressure gradients in the intact material (1) and the fractured domain (2), respectively. Using the representation above, the average value of the gradient of p in the referential volume $\Delta\Omega$ is defined as

$$\begin{aligned} \boldsymbol{\nabla}_{\boldsymbol{x}} p = \frac{1}{\Delta\Omega}\int_{\Delta\Omega} \boldsymbol{\nabla}_{\boldsymbol{x}} p \, d\Omega = \frac{1}{\Delta\Omega}\int_{\Delta\Omega^+\cup\Delta\Omega^-} \boldsymbol{\nabla}_{\boldsymbol{x}} p^{(1)} \, d\Omega \\ + \frac{1}{\Delta\Omega}\int_{\Delta\Gamma_d t_d} \boldsymbol{\nabla}_{\boldsymbol{x}} p^{(2)} \, d\Omega \end{aligned} \tag{2.5}$$

Thus,

$$\boldsymbol{\nabla}_{\boldsymbol{x}} p = (1-\mu)\boldsymbol{\nabla}_{\boldsymbol{x}} p^{(1)} + \mu\boldsymbol{\nabla}_{\boldsymbol{x}} p^{(2)}; \quad \mu = \frac{\Delta\Gamma_d t_d}{\Delta\Omega} = \chi t_d \tag{2.6}$$

where $\boldsymbol{\nabla}_{\boldsymbol{x}} p^{(1)}$ and $\boldsymbol{\nabla}_{\boldsymbol{x}} p^{(2)}$ are the respective averages of $\boldsymbol{\nabla}_{\boldsymbol{x}} p^{(1)}$ and $\boldsymbol{\nabla}_{\boldsymbol{x}} p^{(2)}$, and χ^{-1} is an internal length scale parameter defined as the ratio of the referential volume over

the surface area of the fractured region (i.e., $\chi^{-1} = \Delta\Omega/\Delta\Gamma_d$). This scale parameter also appears in the formulation governing the localized deformation, as discussed later in this section. It should be noted that, using decomposition (2.4), the average pressure gradient $\boldsymbol{\nabla}_{\boldsymbol{x}} p^{(2)}$ in Equation (2.6) may be expressed as

$$\boldsymbol{\nabla}_{\boldsymbol{x}} p^{(2)} = \boldsymbol{\nabla}_{\boldsymbol{x}} p^{(1)} + (\boldsymbol{n} \cdot \boldsymbol{\nabla}_{\boldsymbol{x}} \tilde{p})\boldsymbol{n} \tag{2.7}$$

which upon contracting by the local base vectors (i.e., $\boldsymbol{t}$ and $\boldsymbol{s}$) leads to the set of constraints

$$\boldsymbol{t} \cdot \boldsymbol{\nabla}_{\boldsymbol{x}} p^{(1)} = \boldsymbol{t} \cdot \boldsymbol{\nabla}_{\boldsymbol{x}} p^{(2)} \quad \text{and} \quad \boldsymbol{s} \cdot \boldsymbol{\nabla}_{\boldsymbol{x}} p^{(1)} = \boldsymbol{s} \cdot \boldsymbol{\nabla}_{\boldsymbol{x}} p^{(2)} \tag{2.8}$$

Assume now that the average superficial velocity of fluid flow in both constituents, $\boldsymbol{w}^{(i)}$ (i = 1,2), is governed by Darcy's law, so that

$$\boldsymbol{w}^{(i)} = \frac{1}{\rho_f g}\boldsymbol{K}^{(i)}(-\boldsymbol{\nabla}_{\boldsymbol{x}} p^{(i)} + \rho_f \boldsymbol{g}) = \frac{1}{\rho_f g}\boldsymbol{K}^{(i)}\boldsymbol{h}^{(i)}; \quad i = 1, 2 \tag{2.9}$$

Here, ρ_f is the fluid's intrinsic density, g is the acceleration due to gravity, and $\boldsymbol{K}^{(1)}$ and $\boldsymbol{K}^{(2)}$ are the hydraulic conductivity tensors in the intact and fractured regions, respectively. By subtracting now the body force $\rho_f \boldsymbol{g}$ from both sides of Equation (2.6), it is evident that the volume average of the operator $\boldsymbol{h}$, which is proportional to the hydraulic gradient, can be expressed in a functional form similar to that of representation (2.6) supplemented by constraints (2.8), i.e.

$$\boldsymbol{h} = (1 - \mu)\boldsymbol{h}^{(1)} + \mu\boldsymbol{h}^{(2)} \tag{2.10}$$

subject to

$$\boldsymbol{t}\cdot\boldsymbol{h}^{(1)}=\boldsymbol{t}\cdot\boldsymbol{h}^{(2)} \quad \text{and} \quad \boldsymbol{s}\cdot\boldsymbol{h}^{(1)}=\boldsymbol{s}\cdot\boldsymbol{h}^{(2)} \tag{2.11}$$

The constraints as specified above imply that the normal component of the hydraulic gradient, the latter being the driving force triggering the fluid movement, is discontinuous across the interface whereas the tangential components remain continuous.

A similar approximation to that of Equation (2.10) may be obtained for the average superficial flow velocity $\boldsymbol{w}$. Thus,

$$\boldsymbol{w}=(1-\mu)\boldsymbol{w}^{(1)}+\mu\boldsymbol{w}^{(2)} \tag{2.12}$$

subject to

$$\boldsymbol{n}\cdot\boldsymbol{w}^{(1)}=\boldsymbol{n}\cdot\boldsymbol{w}^{(2)} \tag{2.13}$$

Equation (2.13) implies that there is a discontinuity in the tangential components of velocity while the continuity of flow in the direction normal to the discontinuity surface is preserved. It is noted that, in general, the constraints in Equations (2.11) and (2.13) are similar to those used for describing the flow through a layered porous medium.

Substituting Darcy's law (2.9) in the kinematic constraint (2.13) gives

$$\boldsymbol{n}\cdot\boldsymbol{K}^{(1)}\boldsymbol{h}^{(1)}=\boldsymbol{n}\cdot\boldsymbol{K}^{(2)}\boldsymbol{h}^{(2)} \tag{2.14}$$

Combining now Equations (2.11) and (2.14), the following relation is obtained

$$\boldsymbol{h}^{(2)}=\boldsymbol{\mathcal{C}}\boldsymbol{h}^{(1)} \tag{2.15}$$

where the operator $\boldsymbol{\mathcal{C}}$, which defines the coefficients of constraints, can be expressed in the matrix form as

$$[\boldsymbol{\mathcal{C}}] = \begin{bmatrix} \boldsymbol{t} \\ \boldsymbol{n} \cdot \boldsymbol{K}^{(2)} \\ \boldsymbol{s} \end{bmatrix}^{-1} \begin{bmatrix} \boldsymbol{t} \\ \boldsymbol{n} \cdot \boldsymbol{K}^{(1)} \\ \boldsymbol{s} \end{bmatrix} \tag{2.16}$$

Substituting Equation (2.15) in Equation (2.10) and performing some algebraic transformations, an expression defining the hydraulic gradient in the intact region $\boldsymbol{h}^{(1)}$ in terms of the operator $\boldsymbol{h}$ may be obtained, namely,

$$\boldsymbol{h}^{(1)} = [\boldsymbol{1} + \mu(\boldsymbol{\mathcal{C}} - \boldsymbol{1})]^{-1}\boldsymbol{h} \tag{2.17}$$

where $\boldsymbol{1}$ is the second-order identity tensor. Finally, combining Equations (2.9), (2.12), and (2.15) leads to an enriched form of Darcy's law which incorporates the internal length parameter, that is,

$$\boldsymbol{w} = \frac{1}{\rho_f g}\bar{\boldsymbol{K}}\boldsymbol{h} = \frac{1}{\rho_f g}\bar{\boldsymbol{K}}(-\boldsymbol{\nabla}_{\boldsymbol{x}} p + \rho_f \boldsymbol{g}) \tag{2.18}$$

where $\bar{\boldsymbol{K}}$ is an equivalent hydraulic conductivity tensor defined as

$$\bar{\boldsymbol{K}} = [(1-\mu)\boldsymbol{K}^{(1)} + \mu\boldsymbol{K}^{(2)}\boldsymbol{\mathcal{C}}][\boldsymbol{1} + \mu(\boldsymbol{\mathcal{C}} - \boldsymbol{1})]^{-1}; \quad \mu = \chi t_d, \quad \chi = \frac{\Delta\Gamma_d}{\Delta\Omega} \tag{2.19}$$

It should be noted that for a typical geometry of the referential volume, there is $\mu \ll 1$, so that the above expression can be simplified to

$$\bar{\boldsymbol{K}} = [\boldsymbol{K}^{(1)} + \mu\boldsymbol{K}^{(2)}\boldsymbol{\mathcal{C}}][\boldsymbol{1} + \mu(\boldsymbol{\mathcal{C}} - \boldsymbol{1})]^{-1} \tag{2.20}$$

It is evident from Equation (2.18) that the proposed methodology allows for describing the flow through a fractured domain without invoking any additional degrees of freedom. Thus, a standard FE analysis can be conducted employing the notion of equivalent hydraulic conductivity. The latter, according to Equations (2.19) and (2.20), depends not only on conductivities of intact and fractured regions but also on the size of the considered referential volume (viz., parameter μ). It can also be proven that the hydraulic conductivity $\bar{\boldsymbol{K}}$ is a symmetric tensor, which is of significant advantage in terms of numerical implementation. The formal proof of symmetry is provided in Appendix A (Section 2.6).

It should be mentioned that the fractured region may experience a turbulent flow within its aperture. The most commonly used approximation, however, is the assumption of a laminar flow with the fracture transmissivity assessed using Navier-Stokes, Stokes, or Reynold lubrication equations with different levels of mathematical simplifications [58]. The approximation employed in this work is based on a simplified local cubic law [58,59], in which the longitudinal conductivity coefficient of the fractured region is defined as

$$K_L^{(2)} = \frac{g}{12\vartheta} t_d^2 \tag{2.21}$$

where g and ϑ are the gravitational acceleration and fluid's kinematic viscosity, respectively.

The description of mechanical response associated with localized deformation can be formulated by defining the velocity of the solid as a sum of two continuous functions $\underline{\hat{\boldsymbol{v}}}$ and $\underline{\tilde{\boldsymbol{v}}}$ in the intact region, and a Heaviside step function $\mathcal{H}_{\Gamma_d}$ that accounts for the presence of a strong discontinuity, i.e.

$$\underline{\boldsymbol{\upsilon}} = \underline{\hat{\boldsymbol{\upsilon}}} + \mathcal{H}_{\Gamma_d}\underline{\tilde{\boldsymbol{\upsilon}}} \tag{2.22}$$

Here, the jump of the quantity $\boldsymbol{\upsilon}$ across the localized zone is given by

$$[\![\underline{\boldsymbol{\upsilon}}]\!] = [\![\mathcal{H}_{\Gamma_d}]\!]\underline{\tilde{\boldsymbol{\upsilon}}} \tag{2.23}$$

where $[\![\,.\,]\!] = [\,.\,]^+ - [\,.\,]^-$. Using Equation (2.22), the average value of the gradient of $\boldsymbol{\upsilon}$ over the referential volume can be defined as

$$\begin{aligned}\frac{1}{\Delta\Omega}\int_{\Delta\Omega}\boldsymbol{\nabla}_{\boldsymbol{x}}\underline{\boldsymbol{\upsilon}}\,d\Omega = \frac{1}{\Delta\Omega}\int_{\Delta\Omega}\boldsymbol{\nabla}_{\boldsymbol{x}}\underline{\hat{\boldsymbol{\upsilon}}}\,d\Omega + \frac{1}{\Delta\Omega}\int_{\Delta\Omega^+}\boldsymbol{\nabla}_{\boldsymbol{x}}\underline{\tilde{\boldsymbol{\upsilon}}}\,d\Omega \\ + \frac{1}{\Delta\Omega}\int_{\Delta\Gamma_d t_d}(\underline{\tilde{\boldsymbol{\upsilon}}}\otimes\boldsymbol{\nabla}_{\boldsymbol{x}}\mathcal{H}_{\Gamma_d})\,d\Omega\end{aligned} \tag{2.24}$$

In the expression above

$$\boldsymbol{\nabla}_{\boldsymbol{x}}\mathcal{H}_{\Gamma_d} = [\![\mathcal{H}_{\Gamma_d}]\!]\delta_{\Gamma_d}\boldsymbol{n} \tag{2.25}$$

where δ_{Γ_d} is the Dirac delta function and $\boldsymbol{n}$ is the outward normal to the discontinuity surface. Substituting Equation (2.25) into Equation (2.24) and using Equation (2.23) leads to

$$\frac{1}{\Delta\Omega}\int_{\Delta\Omega}\boldsymbol{\nabla}_{\boldsymbol{x}}\underline{\boldsymbol{\upsilon}}\,d\Omega = \frac{1}{\Delta\Omega}\int_{\Delta\Omega}\boldsymbol{\nabla}_{\boldsymbol{x}}\underline{\hat{\boldsymbol{\upsilon}}}\,d\Omega + \frac{1}{\Delta\Omega}\int_{\Delta\Omega^+}\boldsymbol{\nabla}_{\boldsymbol{x}}\underline{\tilde{\boldsymbol{\upsilon}}}\,d\Omega + \chi[\![\underline{\boldsymbol{\upsilon}}]\!]\otimes\boldsymbol{n} \tag{2.26}$$

The symmetric part of Equation (2.26), in the context of infinitesimal deformation, defines the volume averages of the respective strain rates. Thus [56],

$$\dot{\boldsymbol{\epsilon}} = \dot{\boldsymbol{\epsilon}}^{(1)} + (\chi[\![\underline{\boldsymbol{\upsilon}}]\!]\otimes\boldsymbol{n})^s \tag{2.27}$$

where $\dot{\boldsymbol{\epsilon}}^{(1)}$ is the average strain rate in the intact material while the second term gives the contribution associated with the discontinuous localized deformation.

The constraint of the problem is the requirement of continuity of traction $\boldsymbol{t}$ across the localized region. Thus,

$$\dot{\boldsymbol{t}}' = \boldsymbol{k}[\![\underline{\boldsymbol{v}}]\!] \cong \boldsymbol{n}\dot{\boldsymbol{\sigma}}' = \boldsymbol{n} \cdot \mathfrak{D} : \dot{\boldsymbol{\epsilon}} \tag{2.28}$$

where $\boldsymbol{k}$ is the stiffness operator relating the velocity discontinuity to the effective traction rate $\dot{\boldsymbol{t}}'$, $\boldsymbol{\sigma}'$ is the effective stress tensor and $\mathfrak{D}$ the constitutive fourth-order tensor which defines the properties in the intact region. Combining the above equations and rearranging leads to the localization law

$$[\![\underline{\boldsymbol{v}}]\!] = [(\boldsymbol{k} + \chi \boldsymbol{n} \cdot \mathfrak{D} \cdot \boldsymbol{n})^{-1} \otimes \boldsymbol{n}] : [\mathfrak{D} : \dot{\boldsymbol{\epsilon}}] \tag{2.29}$$

Thus, using Equations (2.27) and (2.29), the following constitutive equation is finally obtained:

$$\dot{\boldsymbol{\sigma}}' = \bar{\mathfrak{D}} : \mathfrak{D} : \dot{\boldsymbol{\epsilon}} \tag{2.30}$$

where

$$\bar{\mathfrak{D}} = \boldsymbol{\mathcal{I}} - \chi \mathfrak{D} : [\boldsymbol{n} \otimes (\boldsymbol{k} + \chi \boldsymbol{n} \cdot \mathfrak{D} \cdot \boldsymbol{n})^{-1} \otimes \boldsymbol{n}] \tag{2.31}$$

where $\boldsymbol{\mathcal{I}}$ is an isotropic fourth-order identity tensor.

It is noted that the stiffness operator $\bar{\mathfrak{D}}$ depends again on the properties of both constituents and the parameter χ. The latter is independent of the thickness of the fractured zone, which is formally eliminated from considerations. The initial

boundary-value problems involving a hydromechanical coupling can now be solved using the constitutive relations (2.18) and (2.30). For the sake of completeness, the governing field equations of the coupled analysis and their numerical solution are reviewed in the following sections.

2.3 Coupled hydromechanical formulation for computational analysis

2.3.1 Balance equations

According to Truesdell's principles [60] of mixture theory, the properties of constituents must lead to a consistent mathematical representation for the mixture. The latter should follow the same mechanical laws as a single-component continuum. The motion of constituents should be studied by isolating it from the mixture and incorporating the effect of interaction with other constituents. Each phase (e.g., solid and fluid phases in a biphasic porous media) is assumed to be present at every material point and to satisfy the balance equations of mass, linear momentum, and moment of linear momentum. In what follows, a brief review is provided of the governing field equations for a biphasic (i.e., fully saturated) porous medium.

The local form of the mass balance equations of solid and fluid phases, with the assumption of no mass exchange between the two phases, is given by the following expressions [18,19,20]

$$\begin{aligned} &\frac{d\rho^s}{dt} + \rho^s \mathrm{div}\boldsymbol{v} = 0 \\ &\frac{d\rho^f}{dt} + \rho^f \mathrm{div}\boldsymbol{v} + \mathrm{div}(\rho^f \boldsymbol{w}) = 0 \end{aligned} \tag{2.32}$$

Here, $\text{div}(\,.\,) \equiv \text{tr}(\frac{\partial(\,.\,)}{\partial \boldsymbol{x}})$, and ρ^s and ρ^f stand for the partial densities of the solid and fluid phases, respectively. Thus, the density of the mixture is defined as $\rho = \rho^s + \rho^f = (1-n)\rho_s + n\rho_f$, where n is the porosity, and ρ_s and ρ_f are the relevant intrinsic densities. Moreover, $\boldsymbol{v}^f$ and $\boldsymbol{v}$ are the fluid and solid velocities, respectively, so that $\boldsymbol{w} = n(\boldsymbol{v}^f - \boldsymbol{v})$ is the superficial velocity of fluid relative to the solid phase (i.e., Darcy's velocity). Expanding now the first term in Equation (2.32b), the mass balance for the fluid can be written as

$$n\frac{d\rho_f}{dt} + \rho_f \frac{dn}{dt} + n\rho_f \text{div}\boldsymbol{v} + \text{div}(\rho_f \boldsymbol{w}) = 0 \tag{2.33}$$

Similarly, using Equation (2.32a), the mass balance of the solid phase reads

$$\frac{dn}{dt} = \frac{(1-n)}{\rho_s}\frac{d\rho_s}{dt} + (1-n)\text{div}\boldsymbol{v} \tag{2.34}$$

Substituting Equation (2.34) into Equation (2.33) gives the following expression for the mass balance of the mixture

$$n\frac{d\rho_f}{dt} + \frac{\rho_f(1-n)}{\rho_s}\frac{d\rho_s}{dt} + \rho_f \text{div}\boldsymbol{v} + \text{div}(\rho_f \boldsymbol{w}) = 0 \tag{2.35}$$

The balance of linear momentum for each phase in the quasi-static condition (i.e., disregarding the inertia forces) is defined by the following set of equations

$$\begin{aligned} &\text{div}\boldsymbol{\sigma}^s + \rho^s \boldsymbol{g} + \boldsymbol{f}^s = \boldsymbol{0} \\ &\text{div}\boldsymbol{\sigma}^f + \rho^f \boldsymbol{g} + \boldsymbol{f}^f = \boldsymbol{0} \end{aligned} \tag{2.36}$$

where $\boldsymbol{\sigma}^s$ and $\boldsymbol{\sigma}^f$ represent the partial Cauchy stress tensors in the solid and fluid phases, respectively, and $\boldsymbol{f}^s$ and $\boldsymbol{f}^f$ are the forces of interaction satisfying $\boldsymbol{f}^s + \boldsymbol{f}^f = \boldsymbol{0}$.

In the equations above, it has been assumed that both phases are subject to the same body force per unit mass. In accordance with the mixture theory, the summation of Equations (2.36a) and (2.36b) result in the following set of equations of equilibrium for the mixture

$$\text{div}\boldsymbol{\sigma} + \rho\boldsymbol{g} = \mathbf{0} \tag{2.37}$$

where $\boldsymbol{\sigma}$ is the total stress in the mixture, that is, $\boldsymbol{\sigma} = \boldsymbol{\sigma}^s + \boldsymbol{\sigma}^f$. The energy conjugates are obtained by the local form of the balance of energy. The balance of energy generally states that the rate of change of internal and kinetic energies in the whole domain is equal to the rate of work done by external agencies such as surface and body forces, heat fluxes and supplies through surfaces and volumes, and so forth. Disregarding the thermal and nonmechanical effects, the rate of stored internal energy density (e) for the mixture can be stated in a local form as

$$\rho\dot{e} = \boldsymbol{\sigma}^s : \dot{\boldsymbol{\epsilon}} + \boldsymbol{\sigma}^f : \dot{\boldsymbol{\epsilon}}^f \tag{2.38}$$

where $\dot{\boldsymbol{\epsilon}}$ and $\dot{\boldsymbol{\epsilon}}^f$ are the strain rates in the constituents.

2.3.2 Incorporation of constitutive relations

In isothermal conditions, when the intrinsic densities are a function of pressure only, the statement of the mass balance of the mixture (Equation (2.34)) reduces to [20]

$$\frac{n}{S_f}\dot{p} + \left(1 - \frac{S}{S_s}\right)\text{div}\boldsymbol{v} + \frac{1}{\rho_f}\text{div}\left(\rho_f \boldsymbol{w}\right) = 0 \tag{2.39}$$

where S, S_s, and S_f are the bulk moduli of the porous matrix, the solid, and the fluid, respectively. For fluids of low viscosity, which cannot resist any shear deformation, the stress state is a spherical tensor $\boldsymbol{\sigma}^f = -np\boldsymbol{1}$, where $\boldsymbol{1}$ is the second-order identity operator and p is the fluid pressure. Under these conditions, it can be shown [20] that the rate of internal energy may be defined in an alternative form to that of expression (2.38), i.e.

$$\rho\dot{e} = \boldsymbol{\sigma}' : \dot{\boldsymbol{\epsilon}} + \left(\frac{1}{\rho_f}\mathrm{div}(\rho_f \boldsymbol{w}) - n\mathrm{div}\left(\frac{1}{n}\boldsymbol{w}\right) + \frac{n}{S_f}\dot{p}\right) p \equiv \langle \boldsymbol{\sigma}', \dot{\boldsymbol{\epsilon}} \rangle + \langle \boldsymbol{w}, p \rangle \tag{2.40}$$

Here, $\langle \boldsymbol{\sigma}', \dot{\boldsymbol{\epsilon}} \rangle$ and $\langle \boldsymbol{w}, p \rangle$ are two energy conjugates, $\boldsymbol{\sigma}'$ is the effective Cauchy stress tensor defined as

$$\boldsymbol{\sigma}' = \boldsymbol{\sigma} + Bp\boldsymbol{1} \tag{2.41}$$

and $B = 1 - S/S_s$ (Biot's coefficient). Apparently, in case of soils there is $S \ll S_s$, so that Equation (2.41) reduces to Terzaghi's effective stress decomposition.

Appropriate constitutive relations must now be added to define each energy-conjugate term in Equation (2.40). For a laminar flow, the energy-conjugate pair $\langle \boldsymbol{w}, p \rangle$ may be defined by the enriched form of Darcy's law (2.18) as postulated in the previous section. At the same time, for the energy-conjugate pair $\langle \boldsymbol{\sigma}', \dot{\boldsymbol{\epsilon}} \rangle$, the constitutive law takes the form (2.30). Restating both these relations

$$\boldsymbol{w} = \frac{1}{\rho_f g}\bar{\boldsymbol{K}}(\boldsymbol{\nabla}_{\boldsymbol{x}} p + \rho_f \boldsymbol{g}); \quad \dot{\boldsymbol{\sigma}}' = \bar{\mathfrak{D}} : \mathfrak{D} : \dot{\boldsymbol{\epsilon}} \tag{2.42}$$

Obviously, in the absence of discontinuities there is $\bar{\boldsymbol{K}} = \boldsymbol{K}$, where the latter is the hydraulic conductivity of the intact material. Also, in the absence of localized deformation there is $\bar{\mathfrak{D}} = \boldsymbol{\mathcal{I}}$, where $\boldsymbol{\mathcal{I}}$ is the fourth-order identity operator, so that

$\bar{\mathfrak{D}} : \mathfrak{D} = \mathfrak{D}$ with $\mathfrak{D}$ defining the properties of the homogeneous continuum.

Equations (2.37) and (2.39) in conjunction with the constitutive equations (2.41) and (2.42) form a system of partial differential equations that govern the coupled hydromechanical interaction in the presence of discontinuities. It is evident that the mathematical structure of these equations is analogous to that describing a homogeneous medium, which is advantageous from the computational point of view. In what follows, the finite element approximation is given which employs a weak (variational) form of these equations.

2.3.3 Weak form of the balance equations and their discretization

Assume that $\Omega \in \mathcal{R}^n$ is the configuration domain enclosed by the boundary $\partial\Omega$ and denote the time interval of the problem as $\Theta := (0, T]$ with $T > 0$. Let

$$\begin{aligned} \emptyset &= \partial_u\Omega \cap \partial_t\Omega = \partial_p\Omega \cap \partial_q\Omega \\ \partial\Omega &= \partial_u\Omega \,\bar{\cup}\, \partial_t\Omega = \partial_p\Omega \,\bar{\cup}\, \partial_q\Omega \end{aligned} \tag{2.43}$$

where $\partial_u\Omega$ and $\partial_p\Omega$ are the Dirichlet boundaries, and $\partial_t\Omega$ and $\partial_q\Omega$ are the Neumann boundaries. Then, the boundary conditions of the problem can be stated as

$$\begin{aligned} \boldsymbol{u} &= \boldsymbol{u}^\star \quad \text{on} \quad \partial_u\Omega \times \Theta \\ \boldsymbol{\sigma}\boldsymbol{n} &= \boldsymbol{t}^\star \quad \text{on} \quad \partial_t\Omega \times \Theta \\ p &= p^\star \quad \text{on} \quad \partial_p\Omega \times \Theta \\ \boldsymbol{w}\cdot\boldsymbol{n} &= q^\star \quad \text{on} \quad \partial_q\Omega \times \Theta \end{aligned} \tag{2.44}$$

where $\boldsymbol{n}$ is the unit outward normal to the boundary. The governing equations (2.37) and (2.39) in conjunction with the constitutive equations (2.41) and (2.42) represent a system of nonlinear partial differential equations which, in general, cannot be solved analytically. A common approach to obtain an approximate numerical solution is to replace them by a weak (e.g., Galerkin) form, which lowers the degree of nonlinearity, and then discretize them in order to obtain a system of algebraic equations. In order to do so, the test (arbitrary virtual) functions $\delta\boldsymbol{u}$, δp are introduced in an affined space such that $\delta\boldsymbol{u} \in \mathfrak{T}_u$ and $\delta p \in \mathfrak{T}_p$. The test functions must be kinematically admissible in terms of the Dirichlet boundary conditions. The space of test functions is defined as

$$\begin{aligned} \mathfrak{T}_u &= \{\, \delta\boldsymbol{u} \,|\, \delta\boldsymbol{u} \in [C^1(\Omega)]^3,\ \delta\boldsymbol{u} = \boldsymbol{0} \quad \text{on} \quad \partial_u\Omega \} \\ \mathfrak{T}_p &= \{\, \delta p \,|\, \delta p \in C^1(\Omega),\ \delta p = 0 \quad \text{on} \quad \partial_p\Omega \} \end{aligned} \tag{2.45}$$

where C^1 stands for the Sobolev space of degree 1. Solution/trial functions ($\boldsymbol{u} \in \mathfrak{S}_u$ and $p \in \mathfrak{S}_p$) are assumed to belong to the sets

$$\begin{aligned} \mathfrak{S}_u &= \{\, \boldsymbol{u} \,|\, \boldsymbol{u} \in [C^1(\Omega)]^3,\ \boldsymbol{u} = \boldsymbol{u}^\star \quad \text{on} \quad \partial_u\Omega \} \\ \mathfrak{S}_p &= \{\, p \,|\, p \in C^1(\Omega),\ p = p^\star \quad \text{on} \quad \partial_p\Omega \} \end{aligned} \tag{2.46}$$

Equations (2.37) and (2.39) combined with Equation (2.42a) are multiplied by the test functions $\delta\boldsymbol{u} \in \mathfrak{T}_u$ and $\delta p \in \mathfrak{T}_p$, respectively. The weak form is then obtained by integrating these equations by parts over the entire domain. By applying the Green's theorem, together with the Neumann boundary conditions (Equations (2.44b) and

(2.44d)), and substituting Equation (2.41), the following integral form is obtained:

$$\int_\Omega \delta\boldsymbol{\epsilon} : \boldsymbol{\sigma}' \, d\Omega - \int_\Omega \delta\boldsymbol{\epsilon} : Bp\boldsymbol{1} \, d\Omega = \int_{\partial_t\Omega} \delta\boldsymbol{u} \cdot \boldsymbol{t}^\star \, d\Gamma + \int_\Omega \delta\boldsymbol{u} \cdot \rho\boldsymbol{g} \, d\Omega \tag{2.47}$$

$$\int_\Omega \delta p \frac{n}{S_f} \dot{p} \, d\Omega + \int_\Omega \delta p B \dot{\boldsymbol{\epsilon}} : \boldsymbol{1} \, d\Omega + \int_\Omega \frac{1}{\rho_f g} \boldsymbol{\nabla}_{\boldsymbol{X}}(\delta p) \cdot \bar{\boldsymbol{K}} \boldsymbol{\nabla}_{\boldsymbol{X}} p \, d\Omega =$$

$$- \int_{\partial_q\Omega} \delta p q^\star d\Gamma + \int_\Omega \frac{1}{g} \boldsymbol{\nabla}_{\boldsymbol{X}}(\delta p) \cdot \bar{\boldsymbol{K}} \boldsymbol{g} \, d\Omega$$

In the finite element approach, the considered domain is discretized by nonoverlapping finite elements and the test and trial functions in each element are approximated as [26]

$$\begin{cases} \{\delta\boldsymbol{u}(\boldsymbol{X},t)\} \approx [\boldsymbol{N}_u(\boldsymbol{X})]\{\delta\bar{\boldsymbol{u}}(t)\} \\ \{\delta p(\boldsymbol{X},t)\} \approx [\boldsymbol{N}(\boldsymbol{X})]\{\delta\bar{p}(t)\} \end{cases} \qquad \begin{cases} \{\boldsymbol{u}(\boldsymbol{X},t)\} \approx [\boldsymbol{N}_u(\boldsymbol{X})]\{\bar{\boldsymbol{u}}(t)\} \\ \{p(\boldsymbol{X},t)\} \approx [\boldsymbol{N}(\boldsymbol{X})]\{\bar{p}(t)\} \end{cases} \tag{2.48}$$

where $\{\delta\bar{\boldsymbol{u}}\}$, $\{\delta\bar{p}\}$, $\{\bar{\boldsymbol{u}}\}$ and $\{\bar{p}\}$ are the nodal values of the variables defined in Equations (2.45) and (2.46), and $[\boldsymbol{N}_u(\boldsymbol{X})]$ and $[\boldsymbol{N}(\boldsymbol{X})]$ are the suitable interpolation (or shape) functions. Here, the time derivative of a function is evaluated based on its nodal values in view of the fact that the shape functions are time-independent. Substituting Equation (2.48) into Equation (2.47), the semidiscrete weak form equations (as a nontrivial solution) are obtained which, using the Voigt (matrix) notation, can be expressed as

$$\int_\Omega [\boldsymbol{L}\boldsymbol{N}_u]^T \{\boldsymbol{\sigma}'\} \, d\Omega - [\boldsymbol{Q}]\{\bar{p}\} - \{\boldsymbol{f}_1\} = \boldsymbol{0} \tag{2.49}$$

$$[\tilde{\boldsymbol{S}}]\{\dot{\bar{p}}\} + [\tilde{\boldsymbol{Q}}]\{\bar{\boldsymbol{v}}\} - [\boldsymbol{H}]\{\bar{p}\} - \{\boldsymbol{f}_2\} = \boldsymbol{0}$$

where

$$[\tilde{\boldsymbol{S}}] = \int_{\Omega} \frac{n}{S_f} \{\boldsymbol{N}\}^T \{\boldsymbol{N}\}\, d\Omega;$$
$$[\boldsymbol{Q}] = \int_{\Omega} B[\boldsymbol{L}\boldsymbol{N}_u]^T \{\boldsymbol{m}\}\{\boldsymbol{N}\}\, d\Omega;$$
$$\{\tilde{\boldsymbol{Q}}\} = \int_{\Omega} B\{\boldsymbol{N}\}^T \{\boldsymbol{m}\}^T [\boldsymbol{L}\boldsymbol{N}_u]\, d\Omega;$$
$$[\boldsymbol{H}] = \int_{\Omega} \frac{1}{\rho_f g} \{\boldsymbol{\nabla N}\}^T [\bar{\boldsymbol{K}}]\{\boldsymbol{\nabla N}\}\, d\Omega;$$
$$\{\boldsymbol{f}_1\} = \int_{\partial_t \Omega} [\boldsymbol{N}_u]^T \{\boldsymbol{t}^\star\}\, d\Gamma + \int_{\Omega} \rho [\boldsymbol{N}_u]^T \{\boldsymbol{g}\}\, d\Omega;$$
$$\{\boldsymbol{f}_2\} = -\int_{\partial q \Omega} q^\star \{\boldsymbol{N}\}^T d\Gamma + \frac{1}{g} \int_{\Omega} [\boldsymbol{\nabla N}]^T [\bar{\boldsymbol{K}}]\{\boldsymbol{g}\} d\Omega$$

In the above equations, $\{\bar{\boldsymbol{v}}\} = \{\dot{\bar{\boldsymbol{u}}}\}$, $\{\boldsymbol{m}\}^T = \{1,1,1,0,0,0\}$, $[\boldsymbol{L}]$ is a matrix of the gradient operator specifying the kinematic strain-displacement relations and $[\boldsymbol{\nabla N}]$ is a matrix which defines the relation between the pressure gradient and the nodal values of fluid pressure. The numerical integration is carried out using the Gaussian quadrature method. The set of equations (2.49) is commonly solved using the Newton-Raphson linearization procedure combined with the generalized Newmark scheme [61] for the time integration. A brief overview of this approach is provided in Appendix B (Section 2.7).

2.4 Numerical examples

In this section, two different numerical examples are provided. The first one involves simulation of a 2D steady-state flow through a domain that contains a single crack and/or a set of randomly oriented fractures. The case of impervious as well as permeable fractures is considered. The former is particularly relevant to a class of materials which undergo a fracture healing, cracks are sealed as a result of chemical

interaction. The second example deals with a classical consolidation problem, i.e. hydromechanical coupling, in the presence of a discontinuity. The results of simulations are compared with those obtained using other available computational strategies. It should be emphasized that there is no experimental data currently available which could be used for a comprehensive verification of the proposed approach. Thus, the simple examples given here serve primarily as an illustration of the main aspects of the general methodology.

2.4.1 A steady-state flow in the presence of discrete fractures

In order to simulate the flow around impervious fractures, the principal values of conductivity tensor in the fractured region, $\boldsymbol{K}^{(2)}$, Equation (2.19), were assumed to approach zero. Note that setting these values equal to zero leads to a singularity in the specification of the equivalent conductivity tensor, Equation (2.19). This singularity can be formally avoided by imposing a constraint of zero flux in the direction normal to the interface. As demonstrated in Appendix C (Section 2.8), in such a case, the equivalent conductivity becomes independent of the internal length scale and the formulation reduces to that given by Haghighat and Pietruszczak [62]. The numerical results presented in this section have been compared with those obtained using a standard finite element approach. In the latter case, the fractured region is modeled as a void with curved near-tip and zero flux boundaries (after Sheng et al [63]) and the finite element mesh is progressively refined towards the crack-tip in order to provide a more accurate response.

The geometry of the problem is shown in Figure 2.2. Two different configurations of impervious cracks, including a single and randomly distributed fracture(s) with a thickness of 3 mm embedded in 10 m $\times$ 10 m porous matrix, have been considered.

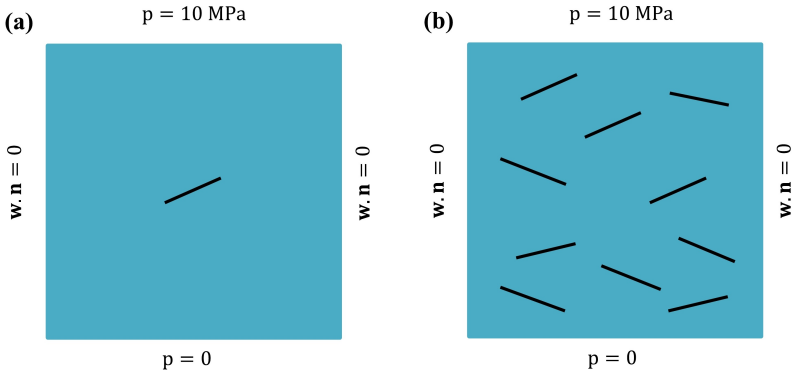

Figure 2.2: A sample 10 m × 10 m with (a) a single crack, (b) randomly distributed cracks

The domain has been subjected to a steady-state flow under a prescribed hydraulic gradient generated by imposing a constant fluid pressure of 10 MPa and zero along the top and bottom boundaries, respectively. The vertical left and right-hand side boundaries were assumed to be impervious (zero flux). Hydraulic conductivity of the intact material was assigned to be $9.8 \times 10^{-6} \frac{\text{m}}{\text{s}}$. For the model with a single discontinuity, a 2 m long fracture inclined at an angle of 25° with respect to horizontal axis was placed in the middle of domain (Figure 2.2a). The model with randomly distributed discontinuities was generated using 10 fractures, all 2 m long, oriented from −25 to 25 degrees with respect to the horizontal direction (Figure 2.2b).

The finite element discretization employed is shown in Figure 2.3. For the proposed approach, referred to as CLED (i.e., constitutive law with embedded discontinuity), both fine and coarse 2D meshes were used incorporating quadrilateral isoparametric elements with bilinear shape functions. The coarse mesh consisted of 637 and 1,394 elements for a single and multiple fracture(s), respectively, whereas the fine mesh incorporated 3,946 and 8,272 elements. For simulations based on standard finite element methodology (SFEM), a very fine mesh was used. The latter employed 18,898 elements for a single crack and 33,658 elements for the case of multiple fractures.

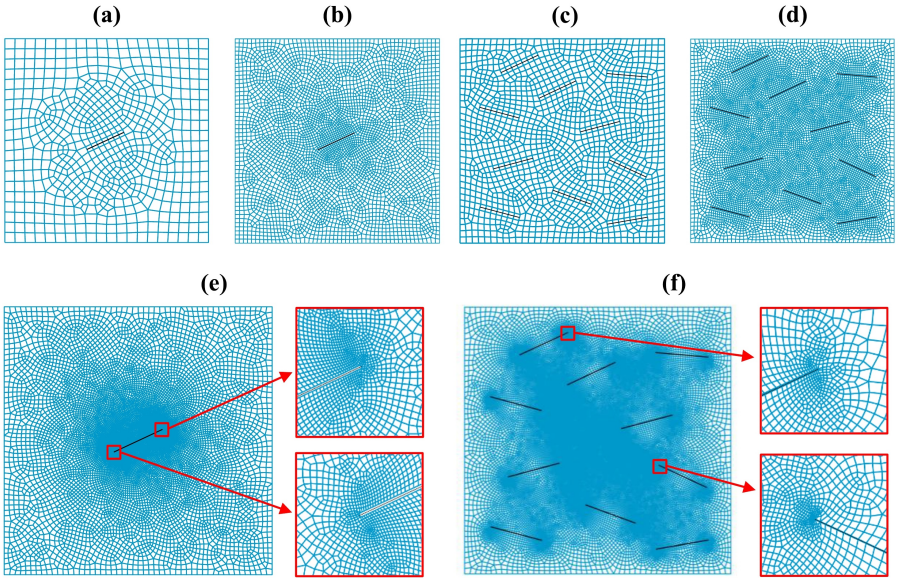

Figure 2.3: (a),(b) Coarse and fine mesh for a single crack; (c),(d) coarse and fine mesh for multiple cracks; (e),(f) SFEM mesh for a single and multiple crack(s)

The key results of the simulations are presented in Figures 2.4–2.6. Figures 2.4 and 2.5 show the pore-fluid pressure distribution obtained using CLED and SFEM approach. At the same time, Figure 2.6 gives the distribution of normalized fluid pressure along the vertical line passing through the center of the domain. In general, the results using CLED are fairly consistent with SFEM solution, even though the former employs a significantly smaller number of elements. This is illustrated in Figure 2.4d which presents the contour plots of the relative difference between the fluid pressures obtained from both solutions, that is, SFEM versus CLED with coarse mesh. As expected, the volume averaging gives less accurate predictions in the areas adjacent to fractures; however, on the macroscale, the discrepancy is negligible. A similar conclusion can be drawn by comparing the results for the coarse and fine mesh in Figures 2.4–2.6. The predicted distribution of fluid pressure, and thus the flow pattern, is very similar. Some differences appear again in the neighborhood of the cracks, whereby the solution for the fine mesh is, in general, more accurate in

relation to SFEM.

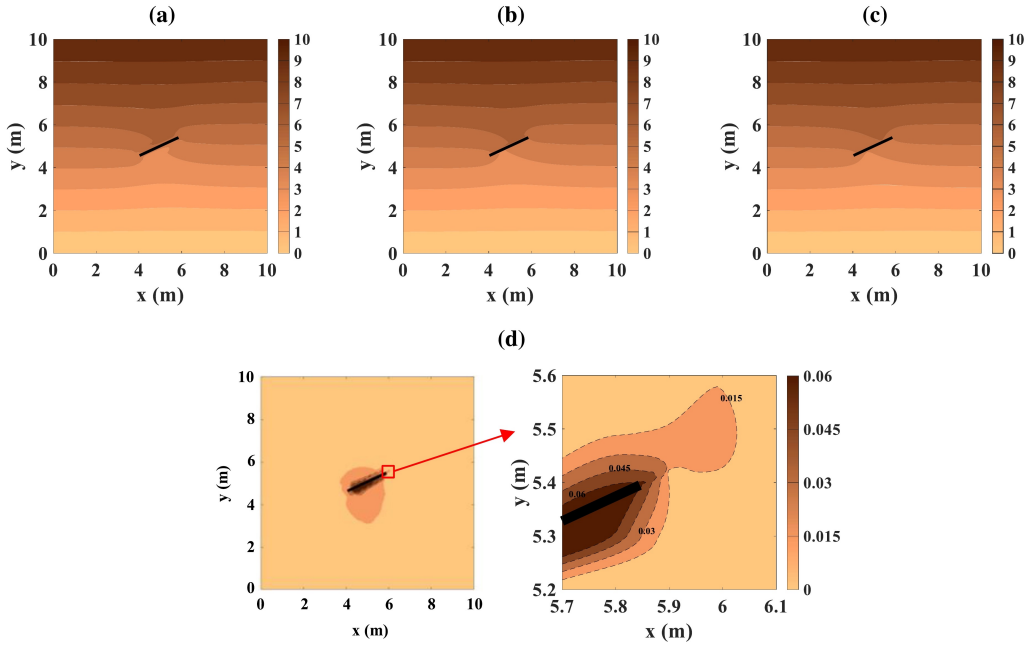

Figure 2.4: Pore-fluid pressure (MPa) distribution in the domain with a single impervious fracture: (a) CLED-FEM coarse mesh, (b) CLED-FEM fine mesh, (c) SFEM, (d) contours of relative difference (RD) between SFEM and CLED (coarse mesh) solutions, $RD(\boldsymbol{x}) = 2 \times |p_1(\boldsymbol{x}) - p_2(\boldsymbol{x})|/(p_1(\boldsymbol{x}) + p_2(\boldsymbol{x}))$; $1 \equiv$ CLED, $2 \equiv$ SFEM

Table 2.1 gives a comparison for the far-field characteristics. The latter include the total out-flow discharge from the sample as well as an average discharge in the vicinity of the fracture. The flux through the fractured region was evaluated in the center of a single crack (Figure 2.2a) across an area of 1 cm $\times$ 1cm. The analytical solution, which is referred to in this table, corresponds to flow through a homogeneous domain (i.e., no fractures). As expected, the presence of impervious fractures results in a reduction of the rate of discharge. The assessment of the volume of flow based on CLED approach is quite reasonable as compared to that corresponding to SFEM.

Finally, in order to complete the analysis, the case of flow through a domain

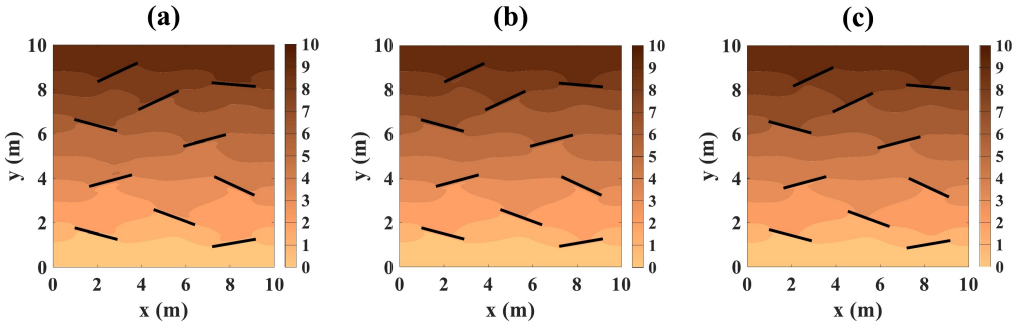

Figure 2.5: Pore-fluid pressure (MPa) distribution in the domain with multiple impervious fractures: (a) CLED-FEM coarse mesh, (b) CLED-FEM fine mesh, (c) SFEM

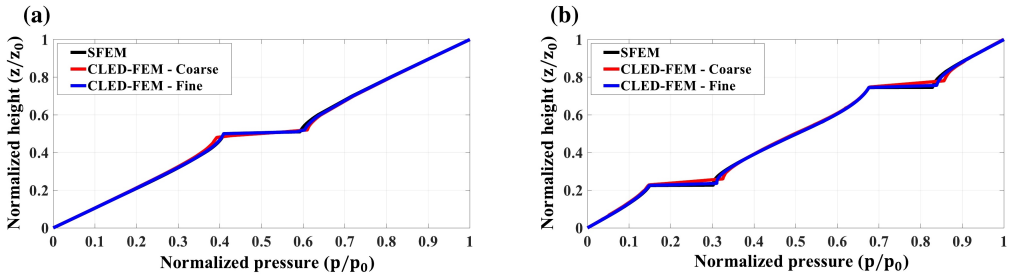

Figure 2.6: Normalized pressure distribution along a vertical line in the center of the (a) single-crack domain, (b) multiple-crack domain ($p_0 = 10\,\text{MPa}$, $z_0 = 10\,\text{m}$)

containing randomly distributed *permeable* fractures has been considered. The simulations were carried out assuming that the longitudinal conductivity in the fractured region obeys the cubic law [58] (i.e., Equation (2.21)). The kinematic viscosity of fluid (here, water at 20°C) and the fracture aperture were taken as $1.0 \times 10^{-6}\,\frac{\text{m}^2}{\text{s}}$ and 3 mm, respectively. The normal component of hydraulic conductivity was assumed to be the same as that in the intact domain (i.e., $9.8 \times 10^{-6}\,\frac{\text{m}}{\text{s}}$). The geometry of the problem and the boundary conditions were kept identical to those shown in Figure 2.2b. The analyses were carried out using the coarse and fine meshes with $1,394$ and $8,272$ quadrilateral isoparametric elements (Figure 2.3c,d).

Figure 2.7 shows the fluid pressure distribution within the domain for both the

Table 2.1: Comparison of results of the far-field characteristics of flow, i.e. the out-flow discharge from the domain and the average discharge in the fractured region (cm^3/s)

	Out-flow discharge (multiple-fractured problem)	Out-flow discharge (single-fractured problem)	Through-fracture discharge (single-fractured problem)
CLED-FEM (coarse)	71.73	96.89	0.42
CLED-FEM (fine)	74.54	97.23	0.41
SFEM (fine)	76.29	97.45	0.42
Analytical solution[a]	100	100	1

[a]Homogeneous domain (no fractures)

coarse and fine meshes. The predicted outflow discharge is 104.16 and 103.12 cm^3/s for the coarse and fine meshes, respectively. Comparing this to results in Table 2.1, it is evident that volume of flow is now significantly higher than that in case of impervious cracks. The results display only a marginal sensitivity to mesh size, which is intrinsic to finite element methodology itself.

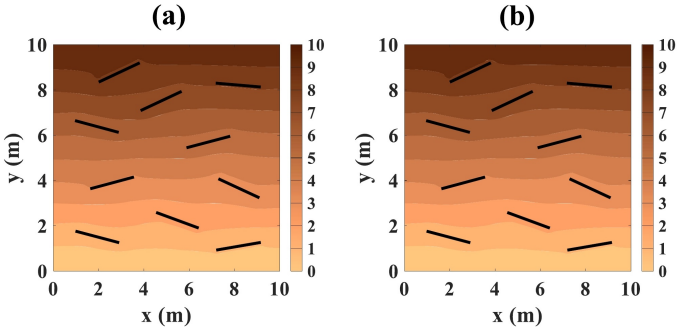

Figure 2.7: Pore-fluid pressure (MPa) distribution in the domain with permeable fractures: CLED-FEM with (a) coarse mesh, (b) fine mesh ($p_0 = 10\,\text{MPa}$, $z_0 = 10\,\text{m}$)

2.4.2 A coupled consolidation analysis involving a preexisting fracture

The second example deals with a consolidation analysis of a porous sample intercepted by a vertical crack, as shown in Figure 2.8. The geometry of the problem and the material properties are taken from the work of Segura and Carol [46], who carried out coupled HM simulations with interface elements (IE) representing the fracture. The analysis is restricted to an elastic range; it incorporates Terzaghi's effective stress principle, and the fracture is considered as a zone with a very high longitudinal conductivity obeying the local cubic law [58] (viz., Equation (2.21)). The intact region is assumed to be isotropic with respect to both mechanical and hydraulic properties, and the fluid is assumed to be incompressible. The values of material parameters are provided in Figure 2.8, where k_x and k_z are the conductivity coefficients along x and z axes, γ_f and ϑ are fluid's unit weight and kinematic viscosity, respectively, and k_t, k_n are the tangential and normal stiffness moduli of the fractured region. It should be noted that in view of the presence of discontinuity, a closed-form solution to this problem cannot be obtained, as the flow and deformation fields are no longer one-dimensional.

The numerical analysis employed quadrilateral isoparametric elements with bilinear and biquadratic shape functions for approximating the pore-fluid pressure and displacement fields, respectively. The domain was discretized using four structured finite element meshes with progressively reduced element size. The coarse meshes, labeled as E1 and E2, incorporated 121 and 441 elements, whereas the finer meshes (referred to as E3 and E4) contained 961 and $2,601$ elements, respectively. The geometry of the FE mesh, together with the definition of associated internal length scale, is shown in Figure 2.9. The number of elements in this figure corresponds to mesh

E2.

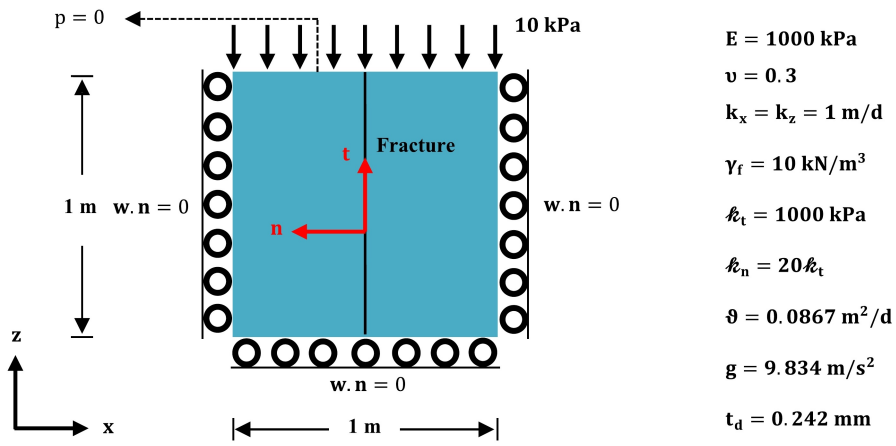

Figure 2.8: Geometry, boundary conditions, and material properties for the consolidation analysis of a porous sample with a vertical fracture

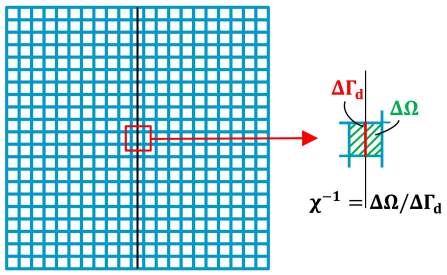

Figure 2.9: Finite element discretization; mesh E2 with the discontinuity embedded in elements along the center line

The analysis was conducted in two stages. The first step involved an undrained response leading to a build-up of the excess of pore water pressure. This was followed by a transient flow coupled with an increasing settlement under the sustained vertical load. Figure 2.10 shows the distribution of pore pressure at different time intervals. It is evident that due to the presence of fracture the rate of flow is not uniform within the domain. At the same time, the pore pressure profiles are very similar for both coarse and fine meshes.

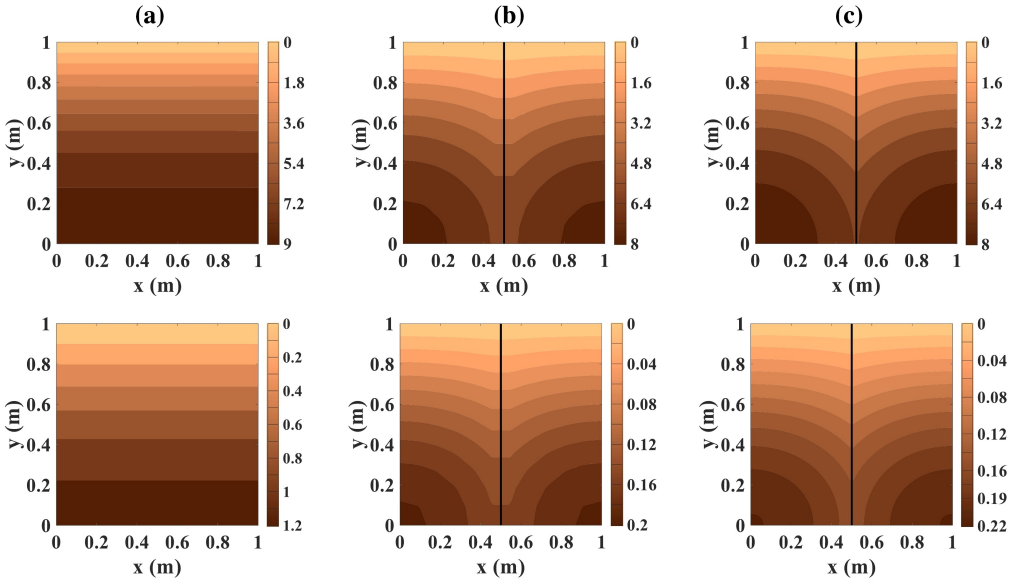

Figure 2.10: Distribution of pore-fluid pressure (kPa) at different time steps for (a) intact domain (Terzaghi's solution), (b) fractured domain with coarse mesh (E1), (c) the fractured domain with fine mesh (E4)

Figure 2.11 shows the evolution of pore pressure in the fractured region, that is, along t-axis in Figure 2.8. Here, the dots represent the results of FEM analysis of Segura and Carol [46], whereas the black solid line is the Terzaghi's analytical solution for a homogeneous domain (no fracture). It is noted that the results obtained using CLED approach are not affected by the mesh size and are almost identical to those generated using the interface elements [46]. The same conclusion applies to the time history of surface settlement at the center of the domain, as presented in Figure 2.12. The latter is also nearly the same for both methodologies employed.

Finally, Figure 2.13a depicts the time history of the total discharge from the upper boundary for all meshes employed in the CLED analysis (i.e., E1-E4). At the same time, Figure 2.13b shows the convergence of the solution as a function of number of elements used. It can be seen that the results based on CLED approach display very little sensitivity to the FEM discretization. This stems from the fact that both the

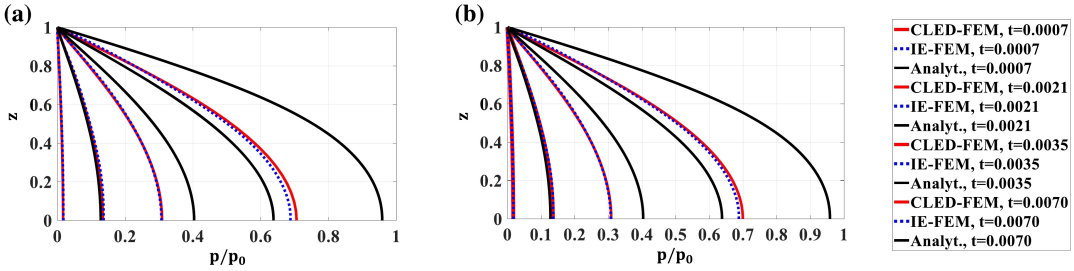

Figure 2.11: Evolution of pore-fluid pressure in the fractured region (a) the coarse mesh (E1), (b) the fine mesh (E4); both compared with IE-FEM (Segura and Carol [46])

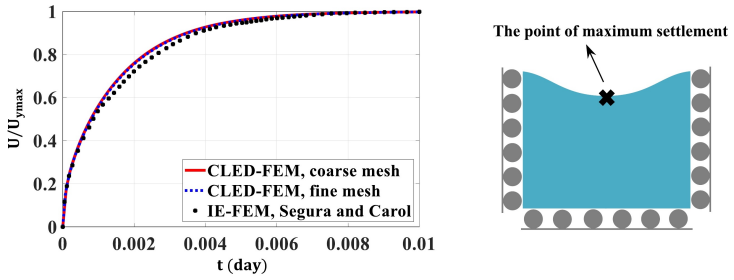

Figure 2.12: Variation of maximum settlement with time; CLED (coarse mesh E1 and fine mesh E4) and IE-FEM (Segura and Carol [46])

hydraulic and mechanical properties in the referential volume depend explicitly on the mesh size. There is no direct comparison here with the results of IE-FEM as the latter were not reported in the original reference. It should be noted, however, that Segura and Carol [46] used interface elements embedded in a coarse mesh that was similar to E1. Thus, although their solution in the interface zone may be sufficiently accurate, outside this zone the results may display mesh sensitivity which will impact the far field quantities, such as volume of discharge and/or the settlement profile.

2.5 Final remarks

In this work, a mathematical formulation for describing the flow in a domain containing discontinuities has been proposed. The methodology involved an embedded

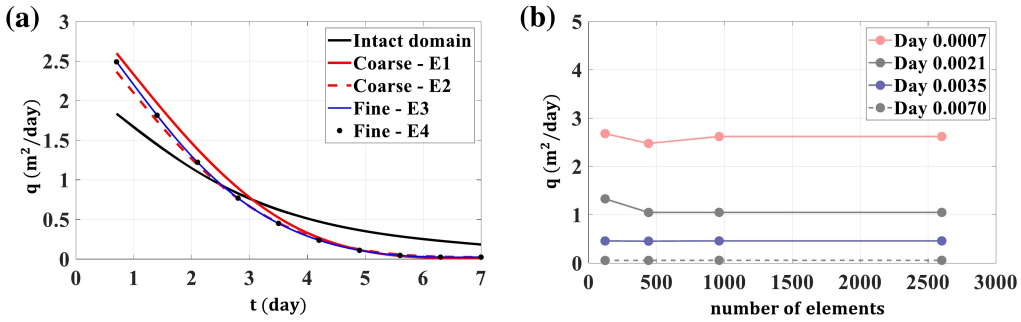

Figure 2.13: (a) Time history of the outflow discharge from the upper boundary, (b) variation of the outflow discharge with the total number of elements

discontinuity approach whereby the averaged flow characteristics have been established in a referential volume adjacent to a preexisting fracture. A weak discontinuity in fluid pressure has been imposed across the region, subject to constraint of continuity of tangential components of the pressure gradient. The proposed approach leads to an enriched form of Darcy's law that incorporates the notion of equivalent conductivity. The latter is defined as a symmetric second-order tensor whose components are a function of hydraulic properties of constituents (viz., intact material and fractured region) as well as the internal length. The suggested approach is computationally very efficient as it does not require the use of any additional degrees of freedom and can easily be implemented in existing commercial finite element packages.

The proposed framework has been combined with a constitutive law with an embedded discontinuity dealing with the description of mechanical response. As a result, a unified approach has been developed for modeling of the hydro-mechanical interaction in the presence of fractures. In the paper, the basic equations of the coupled formulation have been outlined and the approach was illustrated by some numerical examples. In particular, a steady-state flow through a domain containing preexisting fractures as well as a coupled consolidation problem in the presence of a localized

damage have been analyzed. It was demonstrated that the solution is fairly accurate as compared to FE analysis that employs a very fine mesh for modeling the near-crack-tip response (approx. $34,000$ elements) and/or uses interface elements for hydromechanical coupling in the presence of a single fracture. It should be pointed out that although the present study is focused on the preexisting fractures, the methodology is general and can also be incorporated to deal with the onset and propagation of new fractures. The latter may involve the use of a level-set method for a discrete tracing of the crack path [55].

Acknowledgements: The research presented in this paper was supported by the Natural Sciences and Engineering Research Council of Canada (Discovery Grant) and the Canadian Nuclear Safety Commission (CNSC).

2.6 Appendix A: Proof of symmetry of the homogenized conductivity tensor

In order to prove the symmetry of the equivalent hydraulic conductivity tensor, as defined by Equation (2.19), it is convenient to refer the problem to the coordinate system attached to the discontinuity surface (see Figure 2.1a). In this case, the conductivity tensor in the fractured region ($\boldsymbol{K}^{(2)}$) has a diagonal form with the components $K_t^{(2)}$, $K_n^{(2)}$, and $K_s^{(2)}$. Recalling now Equation (2.16), the operator $\boldsymbol{\mathcal{C}}$, which defines the constraints of the problem, viz. Equations (2.11) and (2.14), can be expressed in the form

$$
\begin{aligned}
[\boldsymbol{\mathcal{C}}] &= \begin{bmatrix} 1 & 0 & 0 \\ 0 & K_n^{(2)} & 0 \\ 0 & 0 & 1 \end{bmatrix}^{-1} \begin{bmatrix} 1 & 0 & 0 \\ K_{tn}^{(1)} & K_{nn}^{(1)} & K_{ns}^{(1)} \\ 0 & 0 & 1 \end{bmatrix} \\
&= \begin{bmatrix} 1 & 0 & 0 \\ 0 & \left(K_n^{(2)}\right)^{-1} & 0 \\ 0 & 0 & 1 \end{bmatrix} \begin{bmatrix} 1 & 0 & 0 \\ K_{tn}^{(1)} & K_{nn}^{(1)} & K_{ns}^{(1)} \\ 0 & 0 & 1 \end{bmatrix} = \begin{bmatrix} 1 & 0 & 0 \\ \dfrac{K_{tn}^{(1)}}{K_n^{(2)}} & \dfrac{K_{nn}^{(1)}}{K_n^{(2)}} & \dfrac{K_{ns}^{(1)}}{K_n^{(2)}} \\ 0 & 0 & 1 \end{bmatrix}
\end{aligned}
\tag{2.50}
$$

The term $[\boldsymbol{1} + \mu(\boldsymbol{\mathcal{C}} - \boldsymbol{1})]$ in Equation (2.19) reads

$$
[\boldsymbol{1} + \mu(\boldsymbol{\mathcal{C}} - \boldsymbol{1})] = \begin{bmatrix} 1 & 0 & 0 \\ \mu \dfrac{K_{tn}^{(1)}}{K_n^{(2)}} & 1 + \mu \left(\dfrac{K_{nn}^{(1)}}{K_n^{(2)}} - 1 \right) & \mu \dfrac{K_{ns}^{(1)}}{K_n^{(2)}} \\ 0 & 0 & 1 \end{bmatrix}
\tag{2.51}
$$

whereas the inverse of expression (2.51) becomes

$$[\boldsymbol{1} + \mu(\boldsymbol{\mathcal{C}} - \boldsymbol{1})]^{-1} = \tag{2.52}$$

$$\begin{bmatrix} 1 & 0 & 0 \\ \dfrac{-\mu K_{tn}^{(1)}}{(1-\mu)K_n^{(2)} + \mu K_{nn}^{(1)}} & \dfrac{K_n^{(2)}}{(1-\mu)K_n^{(2)} + \mu K_{nn}^{(1)}} & \dfrac{-\mu K_{ns}^{(1)}}{(1-\mu)K_n^{(2)} + \mu K_{nn}^{(1)}} \\ 0 & 0 & 1 \end{bmatrix}$$

At the same time, the term $[(1-\mu)\boldsymbol{K}^{(1)} + \mu\boldsymbol{K}^{(2)}\boldsymbol{\mathcal{C}}]$ in Equation (2.19) can be written as

$$[(1-\mu)\boldsymbol{K}^{(1)} + \mu\boldsymbol{K}^{(2)}\boldsymbol{\mathcal{C}}] = \tag{2.53}$$

$$\begin{bmatrix} (1-\mu)K_{tt}^{(1)} + \mu K_t^{(2)} & (1-\mu)K_{tn}^{(1)} & (1-\mu)K_{ts}^{(1)} \\ K_{tn}^{(1)} & K_{nn}^{(1)} & K_{ns}^{(1)} \\ (1-\mu)K_{ts}^{(1)} & (1-\mu)K_{ns}^{(1)} & (1-\mu)K_{ss}^{(1)} + \mu K_s^{(2)} \end{bmatrix}$$

Now, multiplying the operators (2.53) by (2.52), the following expression is obtained:

$$\bar{\boldsymbol{K}} = \begin{bmatrix} \bar{K}_{tt} & \bar{K}_{tn} & \bar{K}_{ts} \\ \bar{K}_{nt} & \bar{K}_{nn} & \bar{K}_{ns} \\ \bar{K}_{st} & \bar{K}_{sn} & \bar{K}_{ss} \end{bmatrix} \tag{2.54}$$

where

$$\bar{K}_{nn} = \frac{K_{nn}^{(1)} K_n^{(2)}}{(1-\mu)K_n^{(2)} + \mu K_{nn}^{(1)}};$$

$$\bar{K}_{tn} = \bar{K}_{nt} = \frac{(1-\mu)K_{tn}^{(1)} K_n^{(2)}}{(1-\mu)K_n^{(2)} + \mu K_{nn}^{(1)}};$$

$$\bar{K}_{ns} = \bar{K}_{sn} = \frac{(1-\mu)K_{ns}^{(1)} K_n^{(2)}}{(1-\mu)K_n^{(2)} + \mu K_{nn}^{(1)}};$$

$$\bar{K}_{ts} = \bar{K}_{st} = (1-\mu)K_{ts}^{(1)} - \frac{\mu(1-\mu)K_{tn}^{(1)}K_{ns}^{(1)}}{(1-\mu)K_{n}^{(2)} + \mu K_{nn}^{(1)}};$$

$$\bar{K}_{tt} = (1-\mu)K_{tt}^{(1)} + \mu K_{t}^{(2)} - \frac{\mu(1-\mu)\left(K_{tn}^{(1)}\right)^2}{(1-\mu)K_{n}^{(2)} + \mu K_{nn}^{(1)}};$$

$$\bar{K}_{ss} = (1-\mu)K_{ss}^{(1)} + \mu K_{s}^{(2)} - \frac{\mu(1-\mu)\left(K_{ns}^{(1)}\right)^2}{(1-\mu)K_{n}^{(2)} + \mu K_{nn}^{(1)}}$$

Thus, it is evident that the equivalent conductivity tensor $\bar{\boldsymbol{K}}$, as defined above, is a symmetric operator.

2.7 Appendix B: Temporal discretization and Newton-Raphson linearization procedures

Temporal discretization of the semidiscrete weak form of governing equation follows the generalized Newmark scheme [61]. The time interval ($\Theta := (0, T]$ with $T > 0$) is divided into a number of incremental steps so that $t_{n+1} = t_n + \Delta t$, and the nodal velocities as well as the rates of fluid pressure are evaluated as

$$\{\bar{\boldsymbol{v}}\}_{n+1} = \frac{1}{\beta_1 \Delta t}(\{\bar{\boldsymbol{u}}\}_{n+1} - \{\bar{\boldsymbol{u}}\}_n) + \left(\frac{\beta_1 - 1}{\beta_1}\right)\{\bar{\boldsymbol{v}}\}_n \tag{2.55}$$

$$\{\dot{\bar{p}}\}_{n+1} = \frac{1}{\beta_2 \Delta t}(\{\bar{p}\}_{n+1} - \{\bar{p}\}_n) + \left(\frac{\beta_2 - 1}{\beta_2}\right)\{\dot{\bar{p}}\}_n$$

For the solution to be unconditionally stable, there must be $\beta_1 \,\&\, \beta_2 \geq 1/2$ [26]. Knowing the solution at time step n, the set of Equation (2.49) needs to be solved at time step $n+1$. Substituting Equation (2.55) into Equation (2.49) and performing some algebraic transformations lead to

$$\{\boldsymbol{\Psi}_1\}_{n+1} = \left(\int_\Omega [\boldsymbol{L}\boldsymbol{N}_u]^T \{\boldsymbol{\sigma}'\}\, d\Omega\right)_{n+1} - [\boldsymbol{Q}]\{\bar{p}\}_{n+1} - \{\boldsymbol{f}_1\}_{n+1} = \boldsymbol{0} \tag{2.56}$$

$$\{\boldsymbol{\Psi}_2\}_{n+1} = \frac{1}{\beta_1 \Delta t}[\tilde{\boldsymbol{Q}}]\{\bar{\boldsymbol{u}}\}_{n+1} + \left(\frac{1}{\beta_2 \Delta t}[\tilde{\boldsymbol{S}}] + [\boldsymbol{H}]\right)\{\bar{p}\}_{n+1} - \{\boldsymbol{f}_2\}_{n+1} - \{\boldsymbol{F}_2\}_{n+1} = \boldsymbol{0}$$

where

$$\{\boldsymbol{F}_2\}_{n+1} = [\tilde{\boldsymbol{Q}}]\left(\frac{1}{\beta_1 \Delta t}\{\bar{\boldsymbol{u}}\}_n + \left(\frac{1-\beta_1}{\beta_1}\right)\{\bar{\boldsymbol{v}}\}_n\right) + [\tilde{\boldsymbol{S}}]\left(\frac{1}{\beta_2 \Delta t}\{\bar{p}\}_n + \left(\frac{1-\beta_2}{\beta_2}\right)\{\dot{\bar{p}}\}_n\right)$$

The stress-strain relation for the solid matrix, as defined by Equation (2.42b), is in general nonlinear which results in nonlinearity of the algebraic expressions (2.56a) and (2.56b). In this case, the Newton-Raphson iterative algorithm is utilized to linearize the system by expanding Equations (2.56a) and (2.56b) using Taylor series expansion with the first-order truncation, which gives

$$[\boldsymbol{J}]^i \begin{Bmatrix} \{d\bar{\boldsymbol{u}}\}_n \\ \{d\bar{p}\}_n \end{Bmatrix}^i = - \begin{Bmatrix} \{\boldsymbol{\Psi}_1\}_{n+1} \\ \{\boldsymbol{\Psi}_2\}_{n+1} \end{Bmatrix}^i \tag{2.57}$$

where the Jacobian matrix $[\boldsymbol{J}]$ is

$$[\boldsymbol{J}] = \begin{bmatrix} \dfrac{\partial \boldsymbol{\Psi}_1^{n+1}}{\partial \bar{\boldsymbol{u}}_{n+1}} & \dfrac{\partial \boldsymbol{\Psi}_1^{n+1}}{\partial \bar{p}_{n+1}} \\ \dfrac{\partial \boldsymbol{\Psi}_2^{n+1}}{\partial \bar{\boldsymbol{u}}_{n+1}} & \dfrac{\partial \boldsymbol{\Psi}_2^{n+1}}{\partial \bar{p}_{n+1}} \end{bmatrix} = \begin{bmatrix} [\boldsymbol{S}] & -[\boldsymbol{Q}] \\ \dfrac{1}{\beta_1 \Delta t}[\tilde{\boldsymbol{Q}}] & \dfrac{1}{\beta_2 \Delta t}[\tilde{\boldsymbol{S}}] + [\boldsymbol{H}] \end{bmatrix}$$

and $[\boldsymbol{S}]$ is the equivalent stiffness matrix given by

$$[\boldsymbol{S}] = \int_\Omega [\boldsymbol{L}\boldsymbol{N}_u]^T [\boldsymbol{D}][\boldsymbol{L}\boldsymbol{N}_u]\, d\Omega$$

In the expression above, $[\boldsymbol{D}]$ is the Voigt notation of the fourth-order constitutive tensor $\bar{\mathfrak{D}} : \mathfrak{D}$ as defined in Equation (2.31). Apparently, in the absence of fracture (i.e., in case of homogeneous deformation), there is $\bar{\mathfrak{D}} = \boldsymbol{\mathcal{I}}$ where $\boldsymbol{\mathcal{I}}$ is a fourth-order identity tensor.

2.8 Appendix C: Equivalent conductivity tensor in the domain containing impervious fractures

In what follows, the functional form of the equivalent hydraulic conductivity tensor is derived for the case involving impermeable (sealed) fractures. If there is no flow within the cracked region, the superficial fluid velocity in the referential volume follows Darcy's law of intact region, i.e.

$$\boldsymbol{w} = \frac{1}{\rho_f g}\boldsymbol{K}^{(1)}(-\boldsymbol{\nabla}_{\boldsymbol{x}} p^{(1)} + \rho_f \boldsymbol{g}) = \frac{1}{\rho_f g}\boldsymbol{K}^{(1)}\boldsymbol{h}^{(1)} \tag{2.58}$$

Since the velocity vanishes across the impervious discontinuity, we have

$$\boldsymbol{n} \cdot \boldsymbol{K}^{(1)}\boldsymbol{h}^{(1)} = \boldsymbol{0} \tag{2.59}$$

Substituting Equation (2.10) in Equation (2.59) gives the following expression

$$\mu \boldsymbol{n} \cdot \boldsymbol{K}^{(1)}\boldsymbol{h}^{(2)} = \boldsymbol{n} \cdot \boldsymbol{K}^{(1)}\boldsymbol{h} \tag{2.60}$$

The constraints mentioned in Equation (2.11) imply that the tangential components of the gradient operator $\boldsymbol{h}$ are continuous and are the same as those in the homogenized referential volume. The latter, in conjunction with Equation (2.60), gives the following

set of constraints

$$\boldsymbol{t} \cdot \boldsymbol{h}^{(2)} = \boldsymbol{t} \cdot \boldsymbol{h} \tag{2.61}$$

$$\mu \boldsymbol{n} \cdot \boldsymbol{K}^{(1)} \boldsymbol{h}^{(2)} = \boldsymbol{n} \cdot \boldsymbol{K}^{(1)} \boldsymbol{h}$$

$$\boldsymbol{s} \cdot \boldsymbol{h}^{(2)} = \boldsymbol{s} \cdot \boldsymbol{h}$$

It is convenient now to express Equation (2.61) in a matrix form

$$\boldsymbol{h}^{(2)} = \boldsymbol{\mathcal{A}} \boldsymbol{h} \tag{2.62}$$

where the operator $\boldsymbol{\mathcal{A}}$, which specifies the coefficients of constraints, is defined as

$$[\boldsymbol{\mathcal{A}}] = \begin{bmatrix} \boldsymbol{t} \\ \mu \boldsymbol{n} \cdot \boldsymbol{K}^{(1)} \\ \boldsymbol{s} \end{bmatrix}^{-1} \begin{bmatrix} \boldsymbol{t} \\ \boldsymbol{n} \cdot \boldsymbol{K}^{(1)} \\ \boldsymbol{s} \end{bmatrix} \tag{2.63}$$

Referring the problem to the coordinates system attached to the discontinuity surface, as shown in Figure 2.1a, the components of the operator $\boldsymbol{\mathcal{A}}$ become

$$\begin{aligned} [\boldsymbol{\mathcal{A}}] &= \begin{bmatrix} 1 & 0 & 0 \\ \mu K_{nt}^{(1)} & \mu K_{nn}^{(1)} & \mu K_{ns}^{(1)} \\ 0 & 0 & 1 \end{bmatrix}^{-1} \begin{bmatrix} 1 & 0 & 0 \\ K_{nt}^{(1)} & K_{nn}^{(1)} & K_{ns}^{(1)} \\ 0 & 0 & 1 \end{bmatrix} \\ &= \frac{1}{\mu} \begin{bmatrix} \mu & 0 & 0 \\ \dfrac{K_{nt}^{(1)}}{K_{nn}^{(1)}}(1-\mu) & 1 & \dfrac{K_{ns}^{(1)}}{K_{nn}^{(1)}}(1-\mu) \\ 0 & 0 & \mu \end{bmatrix} \end{aligned} \tag{2.64}$$

Recalling Equation (2.10) and using Equation (2.62), the operator $\boldsymbol{h}^{(1)}$ can then be expressed as

$$\boldsymbol{h}^{(1)} = \frac{1}{1-\mu}(\boldsymbol{1} - \mu\boldsymbol{\mathcal{A}})\boldsymbol{h} \tag{2.65}$$

Substituting Equation (2.64) into Equation (2.65) gives

$$\boldsymbol{h}^{(1)} = \boldsymbol{\mathcal{B}}\boldsymbol{h} \tag{2.66}$$

where

$$[\boldsymbol{\mathcal{B}}] = \begin{bmatrix} 1 & 0 & 0 \\ -\dfrac{K_{nt}^{(1)}}{K_{nn}^{(1)}} & 0 & -\dfrac{K_{ns}^{(1)}}{K_{nn}^{(1)}} \\ 0 & 0 & 1 \end{bmatrix} \tag{2.67}$$

Now, substitution of Equation (2.66) into Equation (2.58) leads to the Darcy's velocity in the homogenized referential volume being defined as

$$\boldsymbol{w} = \frac{1}{\rho_f g}\bar{\boldsymbol{K}}\boldsymbol{h} = \frac{1}{\rho_f g}\bar{\boldsymbol{K}}(-\boldsymbol{\nabla}_{\boldsymbol{x}} p + \rho_f \boldsymbol{g}) \tag{2.68}$$

where $\bar{\boldsymbol{K}}$ is the equivalent conductivity tensor given by

$$\bar{\boldsymbol{K}} = \boldsymbol{K}^{(1)}\boldsymbol{\mathcal{B}} \tag{2.69}$$

The component form of this operator, using Equation (2.67), becomes

$$
\begin{aligned}
[\bar{\boldsymbol{K}}] &= \begin{bmatrix} K_{tt}^{(1)} & K_{nt}^{(1)} & K_{ts}^{(1)} \\ K_{nt}^{(1)} & K_{nn}^{(1)} & K_{ns}^{(1)} \\ K_{ts}^{(1)} & K_{ns}^{(1)} & K_{ss}^{(1)} \end{bmatrix} \begin{bmatrix} 1 & 0 & 0 \\ -\dfrac{K_{nt}^{(1)}}{K_{nn}^{(1)}} & 0 & -\dfrac{K_{ns}^{(1)}}{K_{nn}^{(1)}} \\ 0 & 0 & 1 \end{bmatrix} \\
&= \begin{bmatrix} K_{tt}^{(1)} - \dfrac{(K_{nt}^{(1)})^2}{K_{nn}^{(1)}} & 0 & K_{ts}^{(1)} - \dfrac{K_{nt}^{(1)} K_{ns}^{(1)}}{K_{nn}^{(1)}} \\ 0 & 0 & 0 \\ K_{ts}^{(1)} - \dfrac{K_{nt}^{(1)} K_{ns}^{(1)}}{K_{nn}^{(1)}} & 0 & K_{ss}^{(1)} - \dfrac{(K_{ns}^{(1)})^2}{K_{nn}^{(1)}} \end{bmatrix}
\end{aligned}
\tag{2.70}
$$

It is evident from Equation (2.70) that the equivalent hydraulic conductivity matrix is now independent of the volume fraction μ.

References

[1] R. de Boer, "Highlights in the historical development of the porous media theory: toward a consistent macroscopic theory," *ASME, Applied Mechanics Reviews*, vol. 49, no. 4, pp. 201–262, 1996.

[2] C. Truesdell and R. Toupin, "Sulle basi della termomeccanica," *Rend Linc.*, vol. 22, pp. 158–166, 1957.

[3] C. Truesdell and R. Toupin, "The classical field theories," in *Principles of Classical Mechanics and Field Theory/Prinzipien der Klassischen Mechanik und Feldtheorie*, pp. 226–858, Springer, 1960.

[4] C. Truesdell, "Mechanical basis of diffusion," *The Journal of Chemical Physics*, vol. 37, no. 10, pp. 2336–2344, 1962.

[5] J. Adkins, "Diffusion of fluids through aeolotropic highly elastic solids," *Archive for Rational Mechanics and Analysis*, vol. 15, no. 3, pp. 222–234, 1964.

[6] A. Green and J. Adkins, "A contribution to the theory of non-linear diffusion," *Archive for Rational Mechanics and Analysis*, vol. 15, no. 3, pp. 235–246, 1964.

[7] A. E. Green and P. M. Naghdi, "A theory of mixtures," *Archive for Rational Mechanics and Analysis*, vol. 24, no. 4, pp. 243–263, 1967.

[8] A. E. Green and P. M. Naghdi, "On basic equations for mixtures," *The Quarterly Journal of Mechanics and Applied Mathematics*, vol. 22, no. 4, pp. 427–438, 1969.

[9] A. C. Eringen and J. D. Ingram, "A continuum theory of chemically reacting media—I," *International Journal of Engineering Science*, vol. 3, no. 2, pp. 197–212, 1965.

[10] P. D. Kelly, "A reacting continuum," *International Journal of Engineering Science*, vol. 2, no. 2, pp. 129–153, 1964.

[11] P. Fillunger, *Erdbaumechanik?* Wien: Selbstverlag des Verfassers, 1936.

[12] W. Noll, "A mathematical theory of the mechanical behavior of continuous media," in *Archive for Rational Mechanics and Analysis*, vol. 2, pp. 197–226, 1958.

[13] L. Morland, "A simple constitutive theory for a fluid-saturated porous solid," *Journal of Geophysical Research*, vol. 77, no. 5, pp. 890–900, 1972.

[14] R. M. Bowen, "Theory of mixtures," in *Eringen AC, ed. Continuum Physics. Volume III—Mixtures and EM Field Theories. London: Academic Press*, pp. 1–127, 1976.

[15] R. M. Bowen, "Incompressible porous media models by use of the theory of mixtures," *International Journal of Engineering Science*, vol. 18, no. 9, pp. 1129–1148, 1980.

[16] R. M. Bowen, "Compressible porous media models by use of the theory of mixtures," *International Journal of Engineering Science*, vol. 20, no. 6, pp. 697–735, 1982.

[17] J. H. Prévost, "Mechanics of continuous porous media," *International Journal of Engineering Science*, vol. 18, no. 6, pp. 787–800, 1980.

[18] R. de Boer, *Theory of Porous Media*. Berlin: Springer-Verlag, 2000.

[19] W. Ehlers, "Foundations of multiphasic and porous materials," in *Ehlers W, Bluhm J, eds. Porous Media: Theory, Experimental and Numerical Applications. Berlin: Springer-Verlag*, pp. 3–86, Springer, 2002.

[20] R. I. Borja, "On the mechanical energy and effective stress in saturated and unsaturated porous continua," *International Journal of Solids and Structures*, vol. 43, no. 6, pp. 1764–1786, 2006.

[21] M. A. Biot, "General theory of three-dimensional consolidation," *Journal of Applied Physics*, vol. 12, no. 2, pp. 155–164, 1941.

[22] K. Terzaghi, *Erdbaumechanik auf bodenphysikalischer Grundlage*. Leipzig, Wien: F. Deuticke, 1925.

[23] M. A. Biot, "Theory of propagation of elastic waves in a fluid-saturated porous solid. I. Low-frequency range," *The Journal of the Acoustical Society of America*, vol. 28, no. 2, pp. 168–191, 1956.

[24] M. A. Biot, "Mechanics of deformation and acoustic propagation in porous media," *Journal of Applied Physics*, vol. 33, no. 4, pp. 1482–1498, 1962.

[25] M. A. Biot, "Theory of finite deformations of porous solids," *Indiana University Mathematics Journal*, vol. 21, no. 7, pp. 597–620, 1972.

[26] O. C. Zienkiewicz, A. H. C. Chan, M. Pastor, B. A. Schrefler, and T. Shiomi, *Computational geomechanics with special references to earthquake engineering*. New York: Wiley, 1999.

[27] T. Y. Thomas, *Plastic Flow and Fracture in Solids*. New York: Academic Press, 1961.

[28] J. W. Rudnicki and J. R. Rice, "Conditions for the localization of deformation in pressure-sensitive dilatant materials," *Journal of the Mechanics and Physics of Solids*, vol. 23, no. 6, pp. 371–394, 1975.

[29] J. R. Rice, "On the stability of dilatant hardening for saturated rock masses," *Journal of Geophysical Research*, vol. 80, no. 11, pp. 1531–1536, 1975.

[30] A. C. Eringen, *Microcontinuum Field Theories: I. Foundations and Solids*. Berlin: Springer, 1998.

[31] F. Aldakheel, "Micromorphic approach for gradient-extended thermo-elastic–plastic solids in the logarithmic strain space," *Continuum Mechanics and Thermodynamics*, vol. 29, no. 6, pp. 1207–1217, 2017.

[32] H.-B. Mühlhaus and I. Vardoulakis, "The thickness of shear bands in granular materials," *Géotechnique*, vol. 37, no. 3, pp. 271–283, 1987.

[33] W. Ehlers and W. Volk, "On theoretical and numerical methods in the theory of porous media based on polar and non-polar elasto-plastic solid materials," *International Journal of Solids and Structures*, vol. 35, no. 34-35, pp. 4597–4617, 1998.

[34] H. Rattez, I. Stefanou, J. Sulem, M. Veveakis, and T. Poulet, "Numerical analysis of strain localization in rocks with thermo-hydro-mechanical couplings using

cosserat continuum," *Rock Mechanics and Rock Engineering*, vol. 51, no. 10, pp. 3295–3311, 2018.

[35] P. Germain, "La méthode des puissances virtuelles en mécanique des milieux continus, premiere partie: théorie du second gradient," *J. Mécanique*, vol. 12, no. 2, pp. 235–274, 1973.

[36] F. Collin, R. Chambon, and R. Charlier, "A finite element method for poro mechanical modelling of geotechnical problems using local second gradient models," *International Journal for Numerical Methods in Engineering*, vol. 65, no. 11, pp. 1749–1772, 2006.

[37] E. C. Aifantis, "On the problem of diffusion in solids," *Acta Mechanica*, vol. 37, no. 3, pp. 265–296, 1980.

[38] R. K. Wilson and E. C. Aifantis, "On the theory of consolidation with double porosity," *International Journal of Engineering Science*, vol. 20, no. 9, pp. 1009–1035, 1982.

[39] E. C. Aifantis, "On Barenblatt's problem," *Letters in Applied and Engineering Sciences*, vol. 18, no. 6, pp. 857–867, 1980.

[40] G. I. Barenblatt, I. P. Zheltov, and I. Kochina, "Basic concepts in the theory of seepage of homogeneous liquids in fissured rocks [strata]," *Journal of Applied Mathematics and Mechanics*, vol. 24, no. 5, pp. 1286–1303, 1960.

[41] M. Oda, "Permeability tensor for discontinuous rock masses," *Géotechnique*, vol. 35, no. 4, pp. 483–495, 1985.

[42] S. Azizmohammadi and S. K. Matthäi, "Is the permeability of naturally fractured

rocks scale dependent?," *Water Resources Research*, vol. 53, no. 9, pp. 8041–8063, 2017.

[43] L. J. Durlofsky, "Numerical calculation of equivalent grid block permeability tensors for heterogeneous porous media," *Water resources research*, vol. 27, no. 5, pp. 699–708, 1991.

[44] L. Simoni and S. Secchi, "Cohesive fracture mechanics for a multi-phase porous medium," *Engineering Computations*, vol. 20, no. 5/6, pp. 657–698, 2003.

[45] J. M. Segura and I. Carol, "Coupled HM analysis using zero-thickness interface elements with double nodes. Part I: Theoretical model," *International Journal for Numerical and Analytical Methods in Geomechanics*, vol. 32, no. 18, pp. 2083–2101, 2008.

[46] J. Segura and I. Carol, "Coupled HM analysis using zero-thickness interface elements with double nodes—Part II: Verification and application," *International Journal for Numerical and Analytical Methods in Geomechanics*, vol. 32, no. 18, pp. 2103–2123, 2008.

[47] M. C. Lobão, R. Eve, D. R. J. Owen, and E. A. de Souza Neto, "Modelling of hydro-fracture flow in porous media," *Engineering Computations*, vol. 27, no. 1, pp. 129–154, 2010.

[48] P. Fu, S. M. Johnson, and C. R. Carrigan, "An explicitly coupled hydro-geomechanical model for simulating hydraulic fracturing in arbitrary discrete fracture networks," *International Journal for Numerical and Analytical Methods in Geomechanics*, vol. 37, no. 14, pp. 2278–2300, 2013.

[49] N. Moës, J. Dolbow, and T. Belytschko, "A finite element method for crack

growth without remeshing," *International Journal for Numerical Methods in Engineering*, vol. 46, no. 1, pp. 131–150, 1999.

[50] R. de Borst, J. Réthoré, and M.-A. Abellan, "A numerical approach for arbitrary cracks in a fluid-saturated medium," *Archive of Applied Mechanics*, vol. 75, no. 10, pp. 595–606, 2006.

[51] J. Réthoré, R. d. Borst, and M.-A. Abellan, "A two-scale approach for fluid flow in fractured porous media," *International Journal for Numerical Methods in Engineering*, vol. 71, no. 7, pp. 780–800, 2007.

[52] M. Vahab, S. Akhondzadeh, A. R. Khoei, and N. Khalili, "An X-FEM investigation of hydro-fracture evolution in naturally layered domains," *Engineering Fracture Mechanics*, vol. 191, pp. 187–204, 2018.

[53] S. Pietruszczak and Z. Mróz, "Finite element analysis of deformation of strain-softening materials," *International Journal for Numerical Methods in Engineering*, vol. 17, no. 3, pp. 327–334, 1981.

[54] S. Pietruszczak, "On homogeneous and localized deformation in water-infiltrated soils," *International Journal of Damage Mechanics*, vol. 8, no. 3, pp. 233–253, 1999.

[55] E. Haghighat and S. Pietruszczak, "On modeling of discrete propagation of localized damage in cohesive-frictional materials," *International Journal for Numerical and Analytical Methods in Geomechanics*, vol. 39, no. 16, pp. 1774–1790, 2015.

[56] S. Moallemi, S. Pietruszczak, and Z. Mróz, "Deterministic size effect in concrete

structures with account for chemo-mechanical loading," *Computers & Structures*, vol. 182, pp. 74–86, 2017.

[57] H. Mohammadi and S. Pietruszczak, "Description of damage process in fractured rocks," *International Journal of Rock Mechanics and Mining Sciences*, vol. 113, pp. 295–302, 2019.

[58] R. W. Zimmerman and I.-W. Yeo, "Fluid flow in rock fractures: From the navier-stokes equations to the cubic law," *Dynamics of Fluids in Fractured Rock, Geophysical Monograph-American Geophysical Union*, vol. 122, pp. 213–224, 2000.

[59] O. Coussy, *Poromechanics*. Chichester, England: John Wiley & Sons, 2004.

[60] C. Truesdell, *Rational Thermodynamics*. 2nd ed. New York: Springer-Verlag, 1984.

[61] M. C. Katona and O. Zienkiewicz, "A unified set of single step algorithms part 3: the Beta-m method, a generalization of the newmark scheme," *International Journal for Numerical Methods in Engineering*, vol. 21, no. 7, pp. 1345–1359, 1985.

[62] E. Haghighat and S. Pietruszczak, "On the mechanical and hydraulic response of sedimentary rocks in the presence of discontinuities," *Geomechanics for Energy and the Environment*, vol. 4, pp. 61–72, 2015.

[63] M. Sheng, G. Li, S. Shah, A. R. Lamb, and S. P. A. Bordas, "Enriched finite elements for branching cracks in deformable porous media," *Engineering Analysis with Boundary Elements*, vol. 50, pp. 435–446, 2015.

Chapter 3

On hydromechanical interaction during propagation of localized damage in rocks

A. A. Jameei and S. Pietruszczak, "On hydromechanical interaction during propagation of localized damage in rocks," *Minerals, Special Issue: The Hydro-mechanics of Crystalline Rocks*, vol. 11, no. 2, pp. 162, 2021.

On hydromechanical interaction during propagation of localized damage in rocks

A. A. Jameei and S. Pietruszczak

Department of Civil Engineering, McMaster University, Hamilton, Ontario, Canada

Abstract: This paper provides a mathematical description of hydromechanical coupling associated with propagation of localized damage. The framework incorporates an embedded discontinuity approach and addresses the assessment of both hydraulic and mechanical properties in the region intercepted by a fracture. Within this approach, an internal length scale parameter is explicitly employed in the definition of equivalent permeability as well as the tangential stiffness operators. The effect of the progressive evolution of damage on the hydro-mechanical coupling is examined and an evolution law is derived governing the variation of equivalent permeability with the continuing deformation. The framework is verified by a numerical study involving 3D simulation of an axial splitting test carried out on a saturated sample under displacement and fluid pressure-controlled conditions. The finite element analysis incorporates the Polynomial-Pressure-Projection (PPP) stabilization technique and a fully implicit time integration scheme.

Keyword: hydromechanics, fracture propagation, localization, embedded discontinuity, quasi-brittle rocks

3.1 Introduction

The most widely advocated method for disposal of low and intermediate-level nuclear waste is deep geological disposal. A geological repository is supposed to be constructed at a significant depth below the surface and the potential site should fulfill several criteria, which include low permeability, adequate strength, and the long-term stability of the host rock. The repository uses multiple natural and engineered barriers that include the container, sealing materials, and the host rock. The repository design concepts differ between different countries. The main host rocks considered are igneous crystalline rocks, argillaceous clay rocks, and salts. The choice of host rock is mainly governed by the availability of suitable geological formations of adequate thickness and geological setting.

Deep geological storage is being considered in most countries with nuclear power production. In Switzerland, an active site-selection process is currently underway. The site selections for France and Sweden have already been made and, in Sweden, a nuclear regulatory body is currently reviewing a license application for construction. The first project to enter the construction phase is Finland's Onkalo spent nuclear fuel repository, which obtained regulatory approval in 2015.

In order to build confidence in deep geological disposal technologies, several Underground Research Laboratories (URL) have been constructed. Those include generic URLs built for research and testing purposes (e.g., Mount Terri URL in Switzerland, Tournemire facility in France, Aspo Hard Rock Lab in Sweden) as well as site-specific URLs (e.g., Meuse/Haute Marne URL in France, Onkalo URL in Finland, Gorleben URL in Germany). The subsurface testing allows not only for an in-depth investigation of the selected geological environment but also provides an opportunity for verification of different methodologies for simulating the mechanical response of the

host rock.

Canadian efforts are currently directed at two potential sites, i.e., Bruce County and Ignace area in Ontario. The Bruce site has a sedimentary rock formation (Cobourg limestone of the Michigan Basin), while the Ignace site includes a crystalline rock of the Canadian Shield. In mechanical terms, these two types of rocks have high strength, low permeability, and high sorption capacity, so that they would constitute an efficient barrier to radionuclide migration.

Most sedimentary rocks are inherently anisotropic and often heterogeneous (e.g., [1,2]). Anisotropy is due to stratification resulting from the sedimentation process; heterogeneity, on the other hand, originates from the interspersed fabric (cf. [3,4]). For crystalline rocks, layering takes a less prominent role. Thus, the intact rock may be perceived as isotropic in terms of both mechanical and hydraulic properties (e.g., [2,5,6]). The deformation process is characterized by the onset of microcracks, which progressively increase in density, ultimately coalescing and leading to strain localization at the macroscale. As a result, in crystalline rocks fractures are ubiquitous and the fracture systems exhibit a range of anti-clustered to clustered patterns. The nature and evolution of fracture systems directly influence the strength, geophysical, and fluid transport characteristics. Therefore, the main challenge in terms of modeling the behavior of crystalline rocks is the assessment of hydromechanical properties in the presence of pre-existing and newly forming discontinuities.

The onset of localization is typically considered as a bifurcation problem [7]. Alternatively, in tension regime, some simple path-independent strength criteria are invoked [8]. The localized zones exhibit strain-softening which, for classical continuum representations, leads to ill-posedness of the initial boundary-value problem [9]. The latter results in a pathological mesh-dependency of the numerical solution. In

order to remedy the problem, the classical framework needs to be enriched by incorporating an internal length scale parameter. Common approaches include non-local theories [10,11] as well as Extended Finite Element Method (XFEM) (cf. [12,13]). Both these approaches have limitations that stem either from ambiguity in defining the notion of internal length or, like in the case of XFEM, computational inefficiency resulting from the incorporation of additional degrees of freedom that account for the presence of discontinuities.

The work presented here is focused on the description of hydromechanical coupling associated with the onset and propagation of localized damage. The mathematical framework incorporates an embedded discontinuity approach, which employs volume averaging in order to define representative homogenized properties. The formulation addresses both the assessment of equivalent permeability in the region intercepted by a fracture and the associated interaction with the mechanical response in the presence of discontinuities. In particular, the effect of the progressive evolution of damage on the hydro-mechanical coupling is examined. The framework is verified by a numerical example that involves 3D simulation of an axial splitting test carried out on a saturated sample under external control of fluid pressure.

3.2 Governing equations of hydromechanical coupling under homogeneous and localized deformation

Consider an initial-boundary-value problem involving a saturated porous medium undergoing deformation coupled with a transient flow. Denote the spatial domain and its external boundary as $\mathfrak{B} \in \mathbb{R}^m$ and $\partial\mathfrak{B}$, respectively, where m stands for

the spatial dimension of the problem. Furthermore, let $\mathcal{T}$ be the time interval, such that $\mathcal{T}(0,T]$, and let $\partial\mathfrak{B}$ comprise of nonoverlapping Dirichlet ($\partial_u\mathfrak{B}$ and $\partial_p\mathfrak{B}$) and Neumann boundaries ($\partial_t\mathfrak{B}$ and $\partial_q\mathfrak{B}$). Restricting the considerations to static regime and assuming infinitesimal deformations, the field equations can be stated as (cf. [14])

$$\nabla\cdot(\boldsymbol{\sigma}'-\beta p\boldsymbol{I})+\rho\boldsymbol{g}=\boldsymbol{0}\quad\text{in}\quad\mathfrak{B}\times\mathcal{T} \tag{3.1}$$

$$\alpha\dot{p}+\beta\nabla\cdot\dot{\boldsymbol{u}}+\nabla\cdot[\frac{1}{\mu_f}\boldsymbol{k}\cdot(-\nabla p+\rho_f\boldsymbol{g})]=0\quad\text{in}\quad\mathfrak{B}\times\mathcal{T} \tag{3.2}$$

subject to

$$\boldsymbol{u}=\bar{\boldsymbol{u}}\quad\text{on}\quad\partial_u\mathfrak{B}\times\mathcal{T} \tag{3.3}$$

$$(\boldsymbol{\sigma}'-\beta p\boldsymbol{I})\cdot\boldsymbol{n}=\bar{\boldsymbol{t}}\quad\text{on}\quad\partial_t\mathfrak{B}\times\mathcal{T}$$

$$p=\bar{p}\quad\text{on}\quad\partial_p\mathfrak{B}\times\mathcal{T}$$

$$(1/\mu_f)\boldsymbol{k}\cdot(-\nabla p+\rho_f\boldsymbol{g})\cdot\boldsymbol{n}=\bar{q}\quad\text{on}\quad\partial_q\mathfrak{B}\times\mathcal{T}$$

In equations above, $\boldsymbol{n}$ is the unit outward normal to $\partial\mathfrak{B}$, β is the Biot coefficient, α is defined as $\alpha=n/S_f$, where n and S_f are the porosity and the bulk modulus of fluid, respectively, ρ represents the density of mixture, while $\boldsymbol{g}$ is gravitational acceleration. Moreover, ∇ and $\nabla\cdot$ denote the spatial gradient and divergence operators, $\boldsymbol{k}$ is the permeability tensor, μ_f is the dynamic viscosity of the fluid, p is the pore–fluid pressure, while $\boldsymbol{\sigma}'$ and $\boldsymbol{u}$ are the effective Cauchy stress tensor and the solid's displacement vector, respectively.

It is noted that the balance equations explicitly incorporate Darcy's law for the superficial velocity as well as the effective stress principle. The validity of Equation (3.2) is restricted to the case when the process is isothermal and there is no mass exchange between the solid and fluid phases. For small deformations, the mechanical

power conjugate pair includes the effective stress ($\boldsymbol{\sigma}' = \boldsymbol{\sigma} + \beta p \boldsymbol{I}$) and the infinitesimal strain rate ($\dot{\boldsymbol{\epsilon}} = \operatorname{sym} \nabla \dot{\boldsymbol{u}}$) tensors. Furthermore, the hydraulic power conjugate pair is the pore–fluid pressure (p) and the Darcy's velocity ($\boldsymbol{k} \cdot [-\nabla p + \rho \boldsymbol{g}]/\mu_f$).

The homogenous deformation process may be described using a classical continuum representation. A common approach involves a standard rate-independent elastoplastic idealization, i.e.,

$$\dot{\boldsymbol{\sigma}}' = \mathfrak{D} : \dot{\boldsymbol{\epsilon}}; \quad \mathfrak{D} = \mathfrak{D}^e - \frac{\mathfrak{D}^e : \nabla_{\sigma'} \psi \otimes \nabla_{\sigma'} f : \mathfrak{D}^e}{\nabla_{\sigma'} f : \mathfrak{D}^e : \nabla_{\sigma'} \psi + \mathscr{H}} \tag{3.4}$$

where f and ψ are the yield and potential functions, respectively, $\mathfrak{D}^e$ and $\mathfrak{D}$ are the fourth- order elastic and elastoplastic tangent moduli, $\mathscr{H}$ represents the plastic hardening modulus, $\nabla_{\sigma'}$ is the stress–space gradient operator, and $\otimes$ and "$:$" denote the dyadic product and double contraction between two tensors, respectively. Apparently, for an elastic material, there is $\mathfrak{D} = \mathfrak{D}^e$.

In geomaterials, in particular in sedimentary/crystalline rocks, the failure mode involves localized deformation. The latter is heterogeneous at the macroscale as it entails the development of high strain gradient zones, within which the mechanical response typically exhibits strain-softening. In this case, the standard continuum representation (3.4), which does not incorporate any internal length measure, leads to a systemic dependence of the numerical solution on the discretization. As mentioned earlier, in the last few decades different regularization techniques have been proposed to alleviate this problem, i.e., to restore the well-posedness of the governing equations. In this work, the framework incorporating a constitutive law with embedded discontinuity (CLED) is employed. The approach, which was originally developed in the early 1980s (cf. [15]) and refined in the subsequent works [16,17], incorporates a 'characteristic dimension' associated with the presence of discontinuity. Most of the

past developments dealt with the mechanical response of a single-phase solid and focused on modeling of discrete propagation of the damage in both brittle and frictional materials. Recently, the framework has been extended to include the description of hydro-mechanical interaction [18]. The approach involves imposing a weak discontinuity in fluid pressure as well as a strong discontinuity in the displacement field within the considered referential volume. By enforcing admissible constraints in the flow regime and continuity of tractions in the fractured region, an equivalent permeability and a macroscopic stiffness operator are defined, both incorporating an internal length parameter. Within the CLED approach, the homogenized constitutive relations governing the hydromechanical response within the referential volume adjacent to the localized region, take the form (cf. [18])

$$\dot{\boldsymbol{\sigma}}' = \bar{\mathfrak{D}} : \mathfrak{D} : \dot{\boldsymbol{\epsilon}}; \quad \bar{\boldsymbol{v}} = \frac{1}{\mu_f} \bar{\boldsymbol{k}} \cdot (-\nabla p + \rho_f \boldsymbol{g}) \tag{3.5}$$

where $\bar{\boldsymbol{v}}$ is the superficial (Darcy's) velocity of the fluid and $\bar{\boldsymbol{k}}$ and $\bar{\mathfrak{D}} : \mathfrak{D}$ denote the equivalent permeability and stress–strain tangent modulus tensors. The operators $\bar{\mathfrak{D}}$ and $\bar{\boldsymbol{k}}$ are defined as

$$\bar{\mathfrak{D}} = \boldsymbol{\mathcal{I}} - \chi \mathfrak{D} : [\boldsymbol{n}^d \otimes (\boldsymbol{k} + \chi \boldsymbol{n}^d \cdot \mathfrak{D} \cdot \boldsymbol{n}^{\boldsymbol{d}})^{-1} \otimes \boldsymbol{n}^d] \tag{3.6}$$

$$\bar{\boldsymbol{k}} = [(1 - \chi t_d)\boldsymbol{k}^{(1)} + \chi t_d \boldsymbol{k}^{(2)} \cdot \boldsymbol{\mathcal{C}}][\boldsymbol{I} + \chi t_d (\boldsymbol{\mathcal{C}} - \boldsymbol{I})]^{-1} \tag{3.7}$$

Here, χ^{-1} is the characteristic length defined as the ratio of the referential volume to the surface area of the discontinuity. Moreover, $\boldsymbol{n}^d$ is the unit normal to the discontinuity surface, $\boldsymbol{k}$ denotes the tangent modulus relating the rate of effective traction to velocity jump across the fractured region, $\boldsymbol{\mathcal{I}}$ is the fourth-order identity tensor, t_d is the thickness of the localization zone, $\boldsymbol{k}^{(1)}$ and $\boldsymbol{k}^{(2)}$ denote the permeability

tensors in the intact and localized domain, respectively, and $\boldsymbol{\mathcal{C}}$ is an operator that defines the coefficients of the hydraulic constrains, viz.

$$[\boldsymbol{\mathcal{C}}] = \begin{bmatrix} \boldsymbol{t}^d \\ \boldsymbol{n}^d \cdot \boldsymbol{k}^{(2)} \\ \boldsymbol{s}^d \end{bmatrix}^{-1} \begin{bmatrix} \boldsymbol{t}^d \\ \boldsymbol{n}^d \cdot \boldsymbol{k}^{(1)} \\ \boldsymbol{s}^d \end{bmatrix} \tag{3.8}$$

where $\boldsymbol{t}^d$ and $\boldsymbol{s}^d$ are the unit vectors along the discontinuity surface.

3.2.1 Localization-induced permeability evolution

According to Equation (3.6), the changes in thickness of the localized region do not directly affect the homogenized stress–strain tangent modulus since the expression is independent of it. At the same time, however, the evolution of thickness directly affects the homogenized permeability tensor Equation (3.7). Thus, there is an explicit coupling between the hydraulic and mechanical terms.

The change in equivalent permeability during the ongoing deformation is defined as

$$\dot{\bar{\boldsymbol{k}}} = \frac{\partial \bar{\boldsymbol{k}}}{\partial t_d} \dot{t}_d \tag{3.9}$$

where $\dot{t}_d$ denotes the rate of the change of thickness, which represents the normal component of the velocity jump, i.e.,

$$\dot{t}_d = \boldsymbol{n}^d \cdot [\![\dot{\boldsymbol{u}}]\!] \tag{3.10}$$

Given the requirement of continuity of traction across the interface (cf. [16]), there is

$$[\![\dot{\boldsymbol{u}}]\!] = [(\boldsymbol{k} + \chi \boldsymbol{n}^d \cdot \mathfrak{D} \cdot \boldsymbol{n}^d)^{-1} \otimes \boldsymbol{n}^d] : [\mathfrak{D} : \dot{\boldsymbol{\epsilon}}] \tag{3.11}$$

Substituting now Equation (3.11) into Equation (3.10) gives

$$\dot{t}_d = \boldsymbol{n}^d \cdot [(\boldsymbol{k} + \chi \boldsymbol{n}^d \cdot \mathfrak{D} \cdot \boldsymbol{n}^d)^{-1} \otimes \boldsymbol{n}^d] : [\mathfrak{D} : \dot{\boldsymbol{\epsilon}}] \tag{3.12}$$

Thus, by introducing Equation (3.12) in Equation (3.9), the following expression is obtained

$$\dot{\bar{\boldsymbol{k}}} = \boldsymbol{\zeta} : \dot{\boldsymbol{\epsilon}} \tag{3.13}$$

where $\boldsymbol{\zeta}$ is a fourth-order tensor relating the rates of permeability and strain, which is defined as

$$\boldsymbol{\zeta} = \frac{\partial \bar{\boldsymbol{k}}}{\partial t_d} \otimes \left[\left(\boldsymbol{n}^d \cdot (\boldsymbol{k} + \chi \boldsymbol{n}^d \cdot \mathfrak{D} \cdot \boldsymbol{n}^d)^{-1} \right) \otimes \boldsymbol{n}^d \right] : \mathfrak{D} \tag{3.14}$$

The evolution law Equation (3.13) governs the variation of equivalent permeability tensor during the deformation process associated with strain localization. It is evident that there is a direct coupling here, i.e., the change in the deformation field affects the permeability which, in turn, influences the velocity of flow and the generation of pore-fluid pressure.

In order to evaluate the term $\partial \bar{\boldsymbol{k}} / \partial t_d$, note that the permeability in the intact region ($\boldsymbol{k}^{(1)}$) is independent of thickness t_d. Moreover, the normal component of permeability in the fractured zone, i.e., $\boldsymbol{n}^d \cdot \boldsymbol{k}^{(2)}$, is also independent of thickness. Thus, with reference to Equation (3.8), there is

$$\frac{\partial \boldsymbol{\mathcal{C}}}{\partial t_d} = \mathbf{0} \tag{3.15}$$

Therefore, differentiating Equation (3.7), one obtains

$$\begin{aligned}\frac{\partial \bar{\boldsymbol{k}}}{\partial t_d} &= [-\chi \boldsymbol{k}^{(1)} + \chi \boldsymbol{k}^{(2)} \cdot \boldsymbol{\mathcal{C}} + \chi t_d (\partial \boldsymbol{k}^{(2)}/\partial t_d) \cdot \boldsymbol{\mathcal{C}}][\boldsymbol{I} + \chi t_d (\boldsymbol{\mathcal{C}} - \boldsymbol{I})]^{-1} \\ &- \chi[(1-\chi t_d)\boldsymbol{k}^{(1)} + \chi t_d \boldsymbol{k}^{(2)} \cdot \boldsymbol{\mathcal{C}}][\boldsymbol{I} + \chi t_d (\boldsymbol{\mathcal{C}} - \boldsymbol{I})]^{-1}[\boldsymbol{\mathcal{C}} - \boldsymbol{I}][\boldsymbol{I} + \chi t_d (\boldsymbol{\mathcal{C}} - \boldsymbol{I})]^{-1}\end{aligned} \tag{3.16}$$

In numerical implementation, it is convenient to refer the operator $\partial \bar{\boldsymbol{k}}/\partial t_d$ to the local coordinate system $\boldsymbol{x}^\star$ attached to the discontinuity surface. In this case, the matrix representation becomes

$$\left[\frac{\partial \bar{\boldsymbol{k}}^\star}{\partial t_d}\right] = \begin{bmatrix} \dfrac{\partial \bar{k}_{tt}}{\partial t_d} & \dfrac{\partial \bar{k}_{tn}}{\partial t_d} & \dfrac{\partial \bar{k}_{ts}}{\partial t_d} \\ \dfrac{\partial \bar{k}_{nt}}{\partial t_d} & \dfrac{\partial \bar{k}_{nn}}{\partial t_d} & \dfrac{\partial \bar{k}_{ns}}{\partial t_d} \\ \dfrac{\partial \bar{k}_{st}}{\partial t_d} & \dfrac{\partial \bar{k}_{sn}}{\partial t_d} & \dfrac{\partial \bar{k}_{ss}}{\partial t_d} \end{bmatrix} \tag{3.17}$$

It can be shown that the above operator is symmetric in view of the symmetry of $\bar{\boldsymbol{k}}$. The individual components of this matrix may be expressed, after some algebraic transformations, in the form

$$\begin{aligned}\frac{\partial \bar{k}_{tt}}{\partial t_d} &= \chi\left(k_t^{(2)} - k_{tt}^{(1)} + t_d \frac{\partial k_t^{(2)}}{\partial t_d}\right) + \frac{\chi\left(k_{tn}^{(1)}\right)^2\left((\chi t_d)^2 k_{nn}^{(1)} - (1-\chi t_d)^2 k_n^{(2)}\right)}{\left((1-\chi t_d)k_n^{(2)} + \chi t_d k_{nn}^{(1)}\right)^2}; \\ \frac{\partial \bar{k}_{nn}}{\partial t_d} &= -\frac{\chi k_n^{(2)} k_{nn}^{(1)}\left(k_{nn}^{(1)} - k_n^{(2)}\right)}{\left((1-\chi t_d)k_n^{(2)} + \chi t_d k_{nn}^{(1)}\right)^2}; \\ \frac{\partial \bar{k}_{ss}}{\partial t_d} &= \chi\left(k_s^{(2)} - k_{ss}^{(1)} + t_d \frac{\partial k_s^{(2)}}{\partial t_d}\right) + \frac{\chi\left(k_{ns}^{(1)}\right)^2\left((\chi t_d)^2 k_{nn}^{(1)} - (1-\chi t_d)^2 k_n^{(2)}\right)}{\left((1-\chi t_d)k_n^{(2)} + \chi t_d k_{nn}^{(1)}\right)^2};\end{aligned} \tag{3.18}$$

$$\frac{\partial \bar{k}_{tn}}{\partial t_d} = \frac{\partial \bar{k}_{nt}}{\partial t_d} = -\frac{\chi k_{tn}^{(1)} k_n^{(2)} k_{nn}^{(1)}}{\Big((1-\chi t_d)k_n^{(2)} + \chi t_d k_{nn}^{(1)}\Big)^2};$$

$$\frac{\partial \bar{k}_{ts}}{\partial t_d} = \frac{\partial \bar{k}_{st}}{\partial t_d} = -\chi k_{ts}^{(1)} + \frac{\chi k_{tn}^{(1)} k_{ns}^{(1)} \Big((\chi t_d)^2 k_{nn}^{(1)} - (1-\chi t_d)^2 k_n^{(2)}\Big)}{\Big((1-\chi t_d)k_n^{(2)} + \chi t_d k_{nn}^{(1)}\Big)^2};$$

$$\frac{\partial \bar{k}_{ns}}{\partial t_d} = \frac{\partial \bar{k}_{sn}}{\partial t_d} = -\frac{\chi k_{ns}^{(1)} k_n^{(2)} k_{nn}^{(1)}}{\Big((1-\chi t_d)k_n^{(2)} + \chi t_d k_{nn}^{(1)}\Big)^2}$$

It should be noted that in the expressions above, $\boldsymbol{k}^{(2)}$ is a diagonal operator, whose tangential components $k_s^{(2)}$ and $k_t^{(2)}$ are assumed to follow the local cubic law (cf. [19]), i.e., $|\boldsymbol{k}^{(2)} \cdot \boldsymbol{t}^d| = |\boldsymbol{k}^{(2)} \cdot \boldsymbol{s}^d| = t_d^2/12$. Therefore, in Equation (3.18), there is $\partial k_t^{(2)}/\partial t_d = \partial k_s^{(2)}/\partial t_d = t_d/6$.

Apparently, given the component form of $\partial \bar{\boldsymbol{k}}^\star / \partial t_d$, this operator can be transformed into the global coordinate system by invoking the standard orthogonal transformation, i.e.,

$$\frac{\partial \bar{\boldsymbol{k}}}{\partial t_d} = \boldsymbol{\mathcal{Q}} \cdot \frac{\partial \bar{\boldsymbol{k}}^\star}{\partial t_d} \cdot \boldsymbol{\mathcal{Q}}^T \tag{3.19}$$

where $\boldsymbol{\mathcal{Q}}$ is the transformation tensor whose components are the direction cosines of the base vectors of the local coordinate system.

3.3 Coupled hydromechanical analysis of an axial splitting test

The numerical analysis presented here deals with the simulation of a tensile fracture in a splitting test conducted under fully saturated conditions. The coupled hydromechanical analysis is performed in 3D configuration and incorporates localization-induced permeability evolution. The finite element mesh contains trilinear isoparametric hexahedral elements for both the displacement and pressure fields (Figure 3.1). The coupled FE formulation, which employs the embedded discontinuity approach, follows the framework outlined in Reference [18]. The approach is enhanced by updating the permeability tensor in each loading step, cf. Equation (3.13), and incorporating a stabilization technique of Polynomial-Pressure-Projection (PPP) developed in Reference [20]. The latter is required in the mixed u–p analysis of nearly incompressible (or a very low-permeability) porous media to avoid the loss of stability (cf. [21]) when equal order interpolation functions are used for the field variables. The entire finite element code and the associated systems of linear algebraic equations were developed and solved in MATLAB R2020b.

In the analysis conducted here, the intact material is idealized as elastic-brittle. The onset of localization (tensile crack) is controlled by the maximum tensile strength (f_t) criterion, which stipulates that the macrocrack is perpendicular to the direction of the maximum tensile stress. In the post-localized regime, the strain-softening response along the discontinuity plane is described using a simple plasticity-based framework incorporating a degradation law for the tensile strength that is assumed to depend on the fracture energy (G_f). In particular, the yield function (F) in the localized region is taken in the form

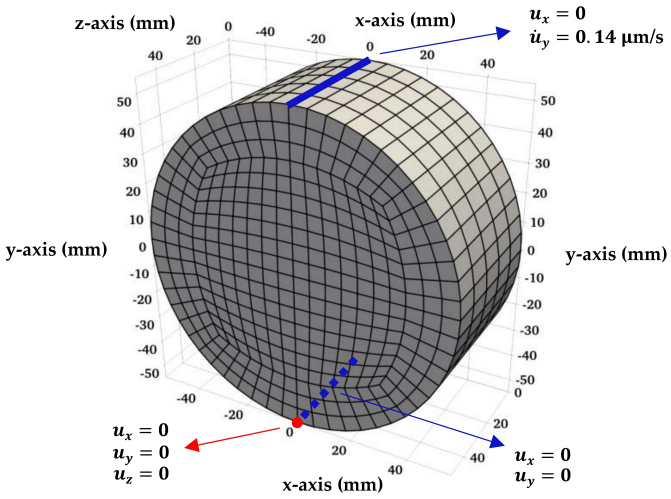

Figure 3.1: Geometry of the problem and the finite element discretization

$$F(\boldsymbol{t}', [\![\boldsymbol{u}]\!]) = \boldsymbol{n}^d \cdot \boldsymbol{\sigma}' \cdot \boldsymbol{n}^d - f_t \exp\left(-\frac{f_t}{G_f}\boldsymbol{n}^d \cdot [\![\boldsymbol{u}]\!]\right) = 0 \tag{3.20}$$

where $\boldsymbol{t}'$ is the effective traction vector. Following now the standard plasticity procedure, with F described by Equation (3.20), the tangent stiffness operator $\boldsymbol{k}$ can be defined. The integration process employs the return-mapping scheme of Reference [17], which is used for the stress update and the specification of the constitutive tensor (cf. Equation (3.6)) in the referential volume encompassing the localized region. The permeability tensor is then explicitly updated using representation (3.13).

The material properties, geometry, and boundary conditions are analogous to those in Reference [22] and pertain to simulation of an axial splitting test conducted on saturated concrete specimen [23]. The parameters used for the analysis are provided in Table 3.1, where E, ν, f_t, and G_f are Young's modulus, Poisson's ratio, tensile strength, and the fracture energy, respectively.

It should be noted that the test simulated here is not a standard Brazilian test. The experimental set-up and the testing protocol have been enhanced to examine the hydro-mechanical coupling and the evolution of permeability associated with the

Table 3.1: Material parameters for the splitting test simulation

α (GPa^{-1})	β	μ_f ($\mathrm{Pa}\cdot\mathrm{s}$)	$k^{(1)}$ (m^2)	E (GPa)	ν	f_t (MPa)	G_f (N/m)
0.01	0.3	10^{-3}	10^{-21}	47	0.2	3	15

onset and propagation of localized damage [23]. The cylindrical sample tested has a diameter of 110 mm and a thickness of 50 mm and is placed between upper and lower bearing plates. The lateral surface of the cylinder is assumed to be impermeable (i.e., no-flux boundary condition). The analysis has been conducted in two stages. In the first stage, a prescribed fluid pressure drop of 0.09 MPa is applied between the two faces of the cylinder. This pressure difference is maintained long enough until a steady-state condition is attained. Then, a prescribed displacement rate in the vertical y-direction is applied at the top of the cylinder (cf. Figure 3.1).

The main results of the analysis are presented in Figures 3.2-3.6. Figure 3.2a shows the variation of the resultant force with the applied vertical displacement. The ultimate load of 23.2 kN is reached at the vertical displacement of 49.7 μm, after which the predicted response is very brittle. Figure 3.2b shows the corresponding evolution of lateral displacements, which was recorded experimentally. Note that two sets of data are provided here (after [23]), which correspond to the same geometry and material type so that the difference indicates the actual scatter of the results. It is seen that both the predicted ultimate load, as well as the progressive increase in lateral displacements in the softening regime, are fairly consistent with the experimental data. Figures 3.3a,b depict the evolution of the horizontal displacement field at different load steps. It is evident here that at the advanced stages of loading the specimen tends to split into two halves, which is triggered by the localized nature of deformation. The results for the displacement field are supplemented by the lateral displacement profiles along the circumferential boundary of the specimen (Figure 3.3c). It should

be noted that these values are indicative of the crack opening, as the letter is the primary mechanism of deformation.

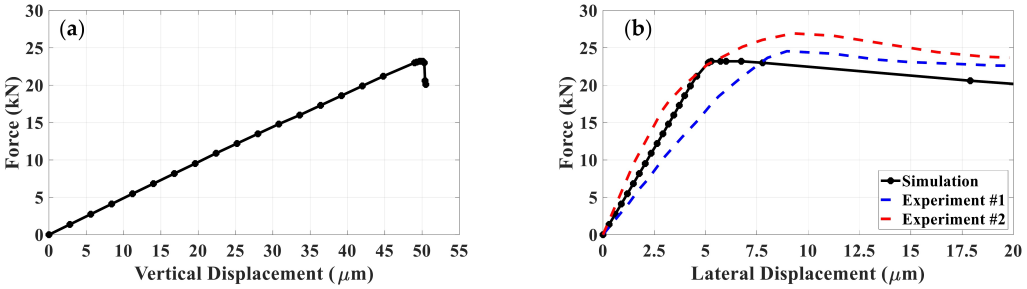

Figure 3.2: (a) Load-vertical displacement, (b) load-lateral displacement characteristics for the hydromechanical axial splitting test

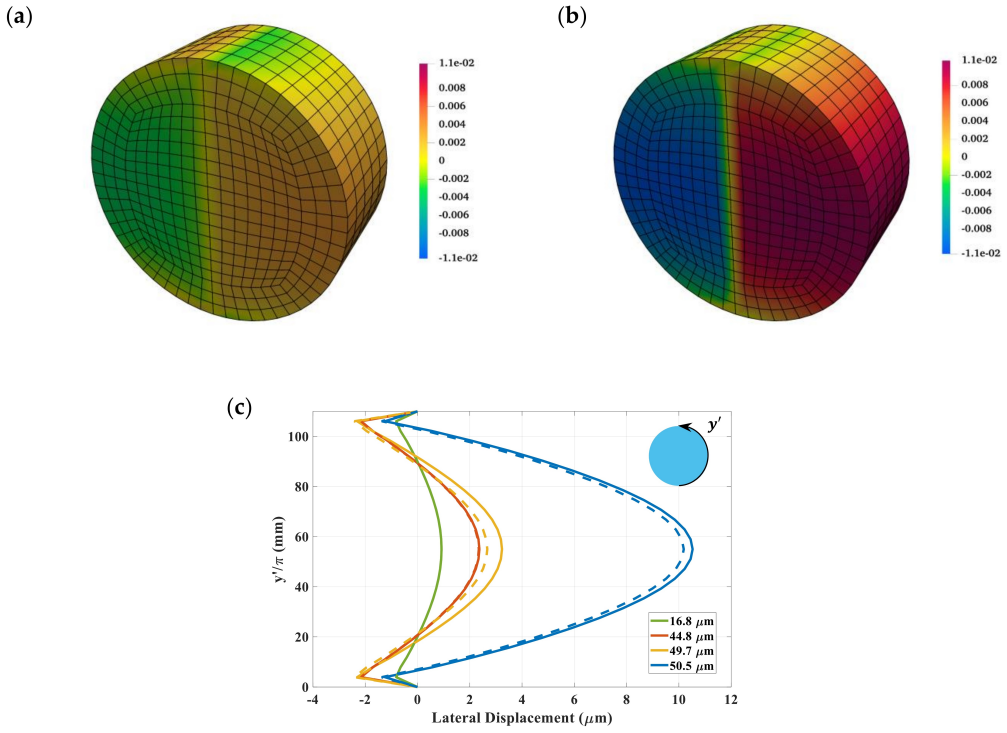

Figure 3.3: Lateral displacement field (mm) at (a) the vertical displacement of 49.7 µm (ultimate load), (b) the vertical displacement of 50.5 µm (final state), (c) the lateral displacement profiles along the circumferential boundary (solid line: front face; dash line: rear face)

It should be mentioned that the analysis conducted here traced the crack propagation in a 'smeared' rather than discrete way (cf. [8]). For the given boundary conditions (i.e., concentrated load), the damage initiated in the region adjacent to load application and the tensile damaged zone was fully developed in the final stages of the analysis. The formation of this tensile crack, penetrating the entire sample, affects the permeability of the specimen, as the latter depends on the crack opening. This is evidenced in Figure 3.4a, which depicts the distribution of the outflow flux. Clearly, the flow is contained to the fractured region and that through the intact domain is negligible. The outflow flux reaches a maximum value of 3.2 μm/s in the middle of the specimen, and progressively decreases along the height of the crack due to reduction of the aperture. The corresponding distribution of the pore-fluid pressure at the end of the analysis is shown in Figure 3.4b.

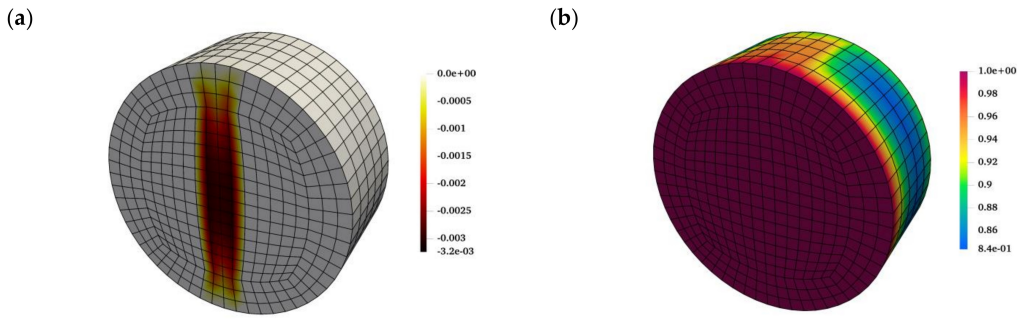

Figure 3.4: Distribution of (a) outflow flux (mm/s), (b) pore-fluid pressure (MPa) at the vertical displacement of 50.5 μm (final stage)

Finally, Figures 3.5 and 3.6 present the evolution of the fluid pressure field in the vertical cut through the middle of the specimen. The contours in Figure 3.5 depict the pore pressure distribution at different stages of loading and are supplemented by the profiles showing the variation along the center lines (Figure 3.6). A non-monotonic rise in fluid pressure with time (i.e., the Mandel–Cryer effect) is captured here in the early stages of analysis, which is due to a very low permeability in the intact region

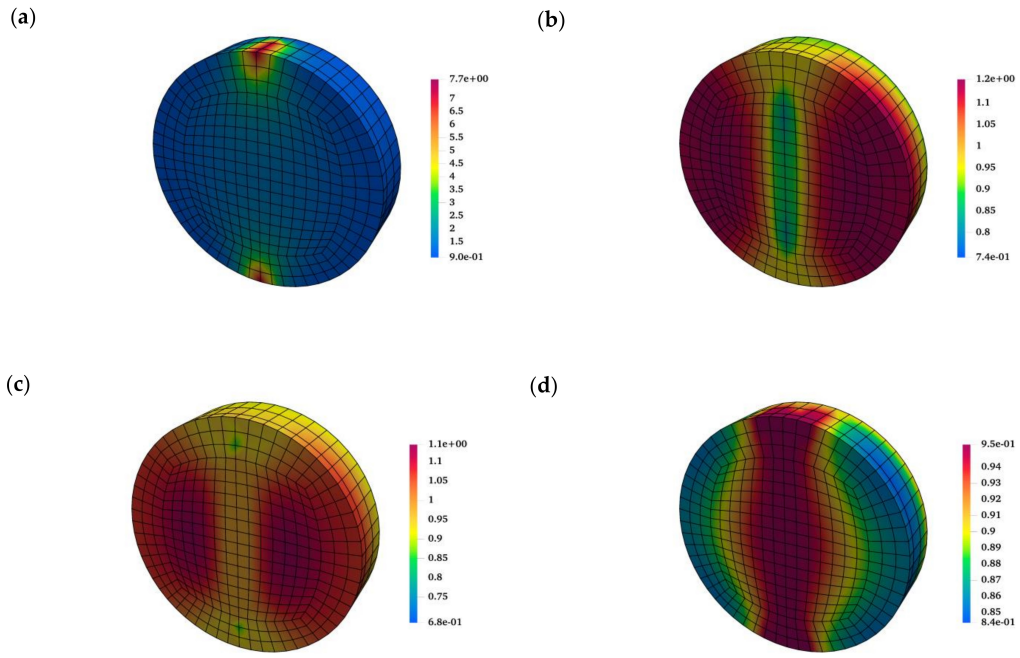

Figure 3.5: Distribution of the pore-fluid pressure (MPa) in a vertical cut through the middle of the specimen, at axial displacement of (a) 16.8 µm, (b) 44.8 µm, (c) 49.7 µm, and (d) 50.5 µm

(Figure 3.5a). As the deformation progresses and the tensile cracks develop, the pore-fluid pressure decreases in the fractured regions due to the volume expansion (Figure 3.5b–d). Moreover, in the softening regime, the dissipation of pore-fluid pressure is accelerated since the permeability in the cracked regions increases with the increase in the crack opening (cf. Figures 3.5d and 3.6).

3.4 Discussion

Many types of rocks, especially crystalline rocks, are brittle and have very low permeability. Thus, prior to the onset of localized damage, their behavior, in fully saturated conditions, may be perceived as undrained. In the course of deformation, the microcracks develop and progressively increase in density, ultimately coalescing and leading

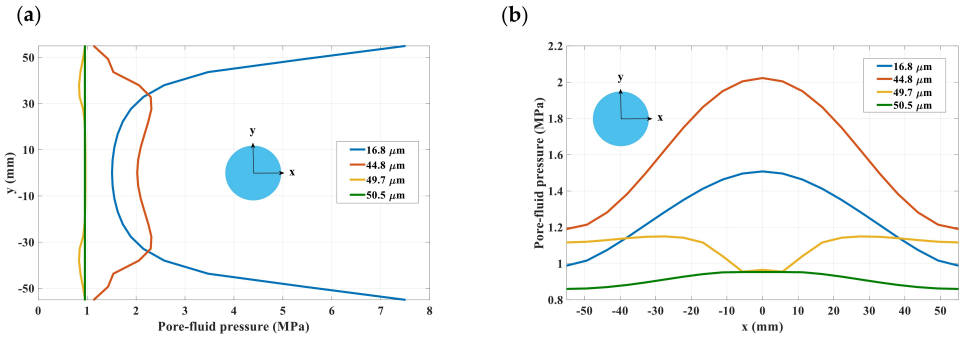

Figure 3.6: Profiles of the pore-fluid pressure (MPa) along (a) vertical, (b) horizontal axes at different vertical displacements

to formation of macrocracks at the continuum level. These fractures create a preferred pathway for the transport of fluid. The propagation of macrocracks within the rock mass is associated with a strong coupling between the hydraulic and mechanical properties in both intact and fractured zones. The present paper is focused on describing this hydromechanical interaction using a volume averaging in the referential domain adjacent to the fracture. Such an approach for dealing with discontinuities is of considerable interest since it is computationally very efficient as compared to other commonly used techniques, like XFEM. Within the proposed framework, the equivalent permeability as well as the tangential stiffness operators both incorporate an internal length scale parameter. This ensures that the solution does not display a pathological sensitivity to FE discretization.

Hydromechanical analysis involving the propagation of localized damage in saturated porous media is a challenging task. In this case, the equivalent permeability operator depends on the aperture (opening) of the fracture and, at the same time, the crack opening evolves during the continuing deformation. In the research reported here, an evolution law was derived governing the variation of equivalent permeability with the macroscopic strain rates. The fully coupled formulation has been implemented in a finite element code developed in MATLAB R2020b and an illustrative

example was provided involving a 3D simulation of an axial splitting test carried out on a saturated cylindrical sample. The results show that the load-vertical displacement characteristic displays an abrupt transition to brittle response after reaching the ultimate load, which is accompanied by the development of excessive lateral deformation. In the softening regime, an intense outflow flux is captured in the proximity of the localized regions triggered by the increase in permeability. Moreover, in the softening range, the pore-fluid pressure is rapidly dissipated because of the volume expansion of the solid matrix along with the evolving permeability in the cracked regions. The results, in terms of assessment of ultimate load, the fracture pattern and the fluid transmissivity are in fair agreement with the experimental data, thus providing a proof of concept in terms of the feasibility of the proposed approach. It should be noted that in the numerical simulations presented here, no special algorithm for the crack tracing was employed and, as a result, the cracks appear as smeared over a narrow region. While this has no visible impact on the predicted ultimate load [24], it does not give a very accurate representation of the crack pattern. The discrete tracing can be incorporated into the present framework using a numerical scheme described in Reference [8]. The latter, however, has only been employed for 2D applications so far and would need to be extended for a 3D geometry.

Author contribution: Conceptualization, A.A.J. and S.P.; formal analysis, A.A.J.; supervision, S.P.; writing—review & editing, A.A.J. and S.P. All authors have read and agreed to the published version of the manuscript.

Funding: The research presented here was supported by the Natural Sciences and Engineering Research Council of Canada (Discovery Grant) and the Canadian Nuclear Safety Commission (CNSC).

References

[1] M. H. B. Nasseri, S. D. Goodfellow, T. Wanne, and R. P. Young, "Thermo-hydro-mechanical properties of cobourg limestone," *International Journal of Rock Mechanics and Mining Sciences*, vol. 61, pp. 212–222, 2013.

[2] E. Ghazvinian, M. S. Diederichs, D. Labrie, and C. D. Martin, "An investigation on the fabric type dependency of the crack damage thresholds in brittle rocks," *Geotechnical and Geological Engineering*, vol. 33, no. 6, pp. 1409–1429, 2015.

[3] T. S. Nguyen, Z. Li, G. Su, M. H. B. Nasseri, and R. P. Young, "Hydro-mechanical behavior of an argillaceous limestone considered as a potential host formation for radioactive waste disposal," *Journal of Rock Mechanics and Geotechnical Engineering*, vol. 10, no. 6, pp. 1063–1081, 2018.

[4] A. P. S. Selvadurai and M. Najari, "Thermo-hydro-mechanical behaviour of the argillaceous cobourg limestone," *Journal of Geophysical Research: Solid Earth*, vol. 122, no. 6, pp. 4157–4171, 2017.

[5] B. Duevel and B. Haimson, "Mechanical characterization of pink Lac du bonnet granite: Evidence of nonlinearity and anisotropy," *International Journal of Rock Mechanics and Mining Sciences*, vol. 34, no. 3-4, p. 117, 1997.

[6] C. D. Martin, "Seventeenth Canadian Geotechnical Colloquium: The effect of cohesion loss and stress path on brittle rock strength," *Canadian Geotechnical Journal*, vol. 34, no. 5, pp. 698–725, 1997.

[7] J. W. Rudnicki and J. R. Rice, "Conditions for the localization of deformation in pressure-sensitive dilatant materials," *Journal of the Mechanics and Physics of Solids*, vol. 23, no. 6, pp. 371–394, 1975.

[8] E. Haghighat and S. Pietruszczak, "On modeling of discrete propagation of localized damage in cohesive-frictional materials," *International Journal for Numerical and Analytical Methods in Geomechanics*, vol. 39, no. 16, pp. 1774–1790, 2015.

[9] R. de Borst and C. V. Verhoosel, "Damage, material instabilities, and failure," *Encyclopedia of Computational Mechanics, Second Edition*, pp. 1–50, 2017.

[10] J. L. Mroginski, G. Etse, and S. M. Vrech, "A thermodynamical gradient theory for deformation and strain localization of porous media," *International Journal of Plasticity*, vol. 27, no. 4, pp. 620–634, 2011.

[11] M. E. Mobasher, L. Berger-Vergiat, and H. Waisman, "Non-local formulation for transport and damage in porous media," *Computer Methods in Applied Mechanics and Engineering*, vol. 324, pp. 654–688, 2017.

[12] M. Luege, J. Lucero, C. Torrijos, and A. Orlando, "Coupled mechanical and fluid flow analysis in fractured saturated porous media using the XFEM," *Applied Mathematical Modelling*, vol. 40, no. 7-8, pp. 4480–4504, 2016.

[13] E. Mikaeili and B. Schrefler, "XFEM, strong discontinuities and second-order work in shear band modeling of saturated porous media," *Acta Geotechnica*, vol. 13, no. 6, pp. 1249–1264, 2018.

[14] R. I. Borja, "On the mechanical energy and effective stress in saturated and unsaturated porous continua," *International Journal of Solids and Structures*, vol. 43, no. 6, pp. 1764–1786, 2006.

[15] S. Pietruszczak and Z. Mróz, "Finite element analysis of deformation of strain-softening materials," *International Journal for Numerical Methods in Engineering*, vol. 17, no. 3, pp. 327–334, 1981.

[16] S. Pietruszczak, "On homogeneous and localized deformation in water-infiltrated soils," *International Journal of Damage Mechanics*, vol. 8, no. 3, pp. 233–253, 1999.

[17] S. Pietruszczak and E. Haghighat, "Modeling of deformation and localized failure in anisotropic rocks," *International Journal of Solids and Structures*, vol. 67, pp. 93–101, 2015.

[18] A. A. Jameei and S. Pietruszczak, "Embedded discontinuity approach for coupled hydromechanical analysis of fractured porous media," *International Journal for Numerical and Analytical Methods in Geomechanics*, vol. 44, no. 14, pp. 1880–1902, 2020.

[19] R. W. Zimmerman and I.-W. Yeo, "Fluid flow in rock fractures: From the navier-stokes equations to the cubic law," *Dynamics of Fluids in Fractured Rock, Geophysical Monograph-American Geophysical Union*, vol. 122, pp. 213–224, 2000.

[20] J. A. White and R. I. Borja, "Stabilized low-order finite elements for coupled solid-deformation/fluid-diffusion and their application to fault zone transients," *Computer Methods in Applied Mechanics and Engineering*, vol. 197, no. 49-50, pp. 4353–4366, 2008.

[21] F. Brezzi and K.-J. Bathe, "A discourse on the stability conditions for mixed finite element formulations," *Computer Methods in Applied Mechanics and Engineering*, vol. 82, no. 1-3, pp. 27–57, 1990.

[22] M. Matallah and C. La Borderie, "3D numerical modeling of the crack-permeability interaction in fractured concrete," in *Proceedings of the 9th International Conference on Fracture Mechanics of Concrete and Concrete Structures (Framcos 9), Berkeley, CA, USA*, pp. 22–25, 2016.

[23] G. Rastiello, C. Boulay, S. Dal Pont, J.-L. Tailhan, and P. Rossi, "Real-time water permeability evolution of a localized crack in concrete under loading," *Cement and Concrete Research*, vol. 56, pp. 20–28, 2014.

[24] E. Haghighat and S. Pietruszczak, "On modeling of fractured media using an enhanced embedded discontinuity approach," *Extreme Mechanics Letters*, vol. 6, pp. 10–22, 2016.

Chapter 4

Coupled hydromechanical analysis of sparsely fractured crystalline rocks

Submitted to a peer reviewed journal.

Coupled hydromechanical analysis of sparsely fractured crystalline rocks

A. A. Jameei and S. Pietruszczak

Department of Civil Engineering, McMaster University, Hamilton, Ontario, Canada

Abstract: This paper addresses the issue of evolution and coalescence of localized damage zones in sparsely fractured crystalline rocks. The approach incorporates a constitutive law with embedded discontinuity, which is phrased in terms of both the hydraulic and mechanical response. The formulation takes into account the hydromechanical interaction in regions intercepted by discontinuities. An internal length scale parameter is employed in the definition of equivalent hydraulic conductivity and the tangential stiffness operators, and the onset of newly developed macrocracks is detected by the bifurcation analysis. An enhanced mixed u-p finite element formulation is derived which considers the effect of progressive evolution of the fracture aperture in the weak statements of balance equations. Fully implicit temporal discretization is employed, and the finite element formulation is stabilized by invoking the Polynomial-Pressure-Projection (PPP) technique. A coupled FE analysis is conducted examining the response of Luc du Bonnet granite, with pre-existing fracture network, subjected to plane strain compression that triggers the crack propagation and coalescence. The approach is first verified on some benchmark problems that involve the presence of a dominant fracture. The results of simulations are compared with those obtained using a very fine mesh incorporating interface elements. Later, a series of coupled analyses are carried out examining the hydromechanical response in the presence of multiple fractures.

Keyword: constitutive law with embedded discontinuity, coupled hydromechanical analysis, localized deformation, sparse fractures, crystalline rocks

4.1 Introduction

Sparsely fractured igneous crystalline rocks constitute an effective barrier to radionuclide migration in deep geological repositories. An example of this type of rock is the Lac du Bonnet granite, which is currently considered as a potential host rock for geological repository of a low and intermediate level nuclear waste in Canada. The Lac du Bonnet batholith is a late-tectonic granite in the western Superior Province of the Canadian Shield, which comprises several lithotectonic regions in northwestern Ontario and eastern Manitoba. The intact rock has a very low permeability and high strength; however, it contains ubiquitous fractures that largely control the deformation and fluid transport characteristics [1,2]. In fact, in most crystalline rocks the interconnected fractures are the main flow conduits for the transport of radionuclide [3,4].

The pre-existing cracks, as well as the onset and progressive coalescence of new macrocracks, directly influence the geophysical properties at the macroscale. In mechanical terms, the study of macrocracks propagation, which involves strain softening behaviour, requires incorporation of some internal length scale parameter. Unfortunately, classical continuum mechanics does not employ such a measure [5]. Consequently, the numerical analysis associated with the presence of discontinuities often suffers from a systemic sensitivity to spatial discretization [6]. There are several remedies to address the problem. Those include non-local theories [7,8,9], as well as the use of advanced micropolar continuum frameworks [10,11,12]. The non-local approach incorporates a characteristic dimension; its definition, however, is somewhat ambiguous. For micropolar continua, the primary difficulty is the identification of additional material parameters that stem from the notion of non-symmetry of the stress tensor. Other techniques dealing with localized deformation involve the use

of interface elements [13,14,15,16] and/or implementation of the extended finite element method (XFEM; [17,18,19]). In the former case, the analysis requires a fine unstructured mesh and is not, in general, suitable for tracing the crack propagation process. Furthermore, it often suffers from numerical instabilities since the geometric and hydraulic properties of fractures and intact rock are significantly different. On the other hand, the XFEM allows for modelling the discontinuous deformation by partitioning the velocity fields at both sides of the discontinuity by a signed distance function. Although the approach is accurate, it is computationally costly. The latter stems from incorporation of additional degrees of freedom that account for the presence of discontinuities, as well the need for partitioning of the domain with triangular sub-elements for the Gaussian integration scheme.

An alternative way to model the localized deformation is to explicitly incorporate an internal length scale parameter in the global form of macroscopic constitutive relations. In this case, the mechanical properties are defined by employing volume averaging of the gradient of a discontinuous velocity field [20,21,22]. This approach, commonly referred to as the constitutive law with embedded discontinuity (CLED), has recently been extended to describe the hydromechanical interaction in the fluid-infiltrated porous media. In particular, an enhanced form of Darcy's law was introduced in which the equivalent hydraulic conductivity was defined as a symmetric second-order tensor [23]. The components of this operator are function of hydraulic properties of both constituents, i.e. intact material and the fracture zone, and the definition incorporates the above mentioned internal scale parameter. The proposed methodology was verified by some preliminary numerical examples which included a hydro-mechanical analysis of an axial splitting test [24].

In this study, a new CLED finite element formulation is presented which considers the coupling between evolution of hydraulic and mechanical properties in the weak

statements of the governing field equations. This approach is then applied to examine the crack propagation and coalescence in the fractured Lac du Bonnet granite. The intact rock is considered as an elastoplastic-brittle material. The plasticity formulation is derived by attributing the hardening effects to the deviatoric plastic strain and the formation of macrocracks is described as a bifurcation problem. A series of coupled analyses are carried out examining the hydro-mechanical response in the presence of multiple fractures. In this case, the deformation process affects the fracture aperture which, in turn, influences the generation of fluid pressure. The notion of the loss of stability in a saturated porous medium is also addressed by examining the evolution of the second rate of internal work.

4.2 Coupled formulation for crystalline rocks containing discontinuities

4.2.1 Local balance equations governing homogeneous deformation

The formulation of an initial boundary value problem involving a coupled hydromechanical interaction incorporates the mass and linear momentum balance equations supplemented by constitutive relations governing the deformation and the transient flow processes. Denote the spatial domain and its external boundary as $\Omega \in \mathbb{R}^m$ and $\partial\Omega$ respectively, where m stands for the spatial dimension of the problem. Let $\tilde{n}_i$ represent the outward normal to $\partial\Omega$ and Θ be the time interval, such that $\Theta := (0, t]$. Furthermore, assume that $\partial\Omega$ comprises non-overlapping Dirichlet ($\partial_u\Omega$ and $\partial_p\Omega$) and Neumann boundaries ($\partial_t\Omega$ and $\partial_q\Omega$). Restricting the considerations to static regime, the field equations can be stated as [25]

$$\sigma'_{ij,j} - \beta p_{,i} + \rho g_i = 0 \quad \text{in} \quad \Omega \times \Theta \tag{4.1}$$

$$\alpha \dot{p} + \beta \dot{u}_{i,i} + (1/\rho_f g)(k_{ij}(-p_{,j} + \rho_f g_j))_{,i} = 0 \quad \text{in} \quad \Omega \times \Theta \tag{4.2}$$

subject to

$$u_i = u_i^\star \quad \text{on} \quad \partial_u \Omega \times \Theta \tag{4.3}$$

$$p = p^\star \quad \text{on} \quad \partial_p \Omega \times \Theta$$

$$(\sigma'_{ij} - \beta p \delta_{ij})\tilde{n}_j = T_i^\star \quad \text{on} \quad \partial_t \Omega \times \Theta$$

$$(1/\rho_f g) k_{ij}(-p_{,j} + \rho_f g_j)\tilde{n}_i = q^\star \quad \text{on} \quad \partial_q \Omega \times \Theta$$

Here, u_i and p denote the displacement vector and the pore-fluid pressure, respectively, β is the Biot coefficient and σ'_{ij} represents the effective stress tensor ($\sigma'_{ij} = \sigma_{ij} + \beta p \delta_{ij}$). Furthermore, g is the gravitational acceleration while g_i denotes its vectorial representation, α is defined as the porosity divided by the bulk modulus of fluid, ρ represents the density of mixture, ρ_f is the intrinsic fluid density, and k_{ij} is the hydraulic conductivity tensor. It should be noted that the balance Equations (4.1) and (4.2) explicitly incorporate the effective stress principle together with Darcy's law, and the validity of these equations is restricted to the case when the process is isothermal and there is no mass exchange between the solid and fluid phases.

The above stated balance equations, together with the constitutive relations, represent a system of non-linear partial differential equations which, in general, cannot be solved analytically. A common approach to obtain an approximate numerical solution is to replace them by a weak (e.g., Galerkin) form, which lowers the degree of non-linearity, and then discretize them in order to obtain a system of algebraic equations. This approach is discussed in detail in Section 4.2.4.

4.2.2 Description of deformation process prior to the onset of localization

The experimental evidence on the mechanical properties of the Lac du Bonnet granite comes primarily from tests conducted on samples collected at Underground Research Laboratory (URL) located in south-eastern Manitoba. The experimental work involved a number of standard tests, which included uniaxial compression, Brazilian splitting tests as well as triaxial compression (cf. [26,27]). The existing evidence indicates that the intact rock is isotropic. At the same time, the samples collected from around URL galleries contain multiple fractures. Thus, the main challenge in terms of modeling of the behaviour of Lac du Bonnet granite is the assessment of hydromechanical properties in the presence of discontinuities. This topic will be explicitly addressed in detail in Section 4.2.3.

The experimental data involving triaxial tests shows that the behaviour under higher confinement is plastic-brittle. The results also indicate that the failure envelopes are non-linear in the meridional sections. Thus, the approximation based on Mohr-Coulomb criterion is not, in general, accurate. This conclusion is evident from the data reported by several investigators (e.g., [27,1,28]). In view of this, the conditions at failure have been defined here using a quadratic form [29]

$$F = c_1(\frac{\sqrt{3}\bar{\sigma}}{g(\theta)f_0}) + c_2(\frac{\sqrt{3}\bar{\sigma}}{g(\theta)f_0})^2 - (c_3 + \frac{\sigma_m}{f_0}) = 0 \tag{4.4}$$

where f_0 is a normalizing constant, taken here as 1 MPa, and c's are dimensionless material parameters. In addition, σ_m, $\bar{\sigma}$, and θ are the invariants of the effective stress tensor σ'_{ij} defined as

$$\sigma_m = -\frac{1}{3}\sigma'_{ii}; \quad \bar{\sigma} = \sqrt{J_2}; \quad \theta = \frac{1}{3}\arcsin\left(\frac{-3\sqrt{3}}{2\bar{\sigma}^3}J_3\right) \tag{4.5}$$

where J_2 and J_3 are the basic invariants of the stress deviator, θ denotes the Lode's angle and $g(\theta)$ is specified in ref. [30].

Note that solving Equation (4.4) for $\bar{\sigma}$, gives an equivalent form of the failure function, viz.

$$F = \sqrt{3}\bar{\sigma} - g(\theta)\bar{\sigma}_c = 0; \quad \bar{\sigma}_c = \frac{-c_1 + \sqrt{c_1^2 + 4c_2(c_3 + \sigma_m/f_0)}}{2c_2} f_0 \tag{4.6}$$

The plasticity formulation can be derived by attributing the hardening effects to the deviatoric plastic strain and assuming the yield surface in a functional form similar to representation (4.6), i.e.

$$f = \sqrt{3}\bar{\sigma} - bg(\theta)\bar{\sigma}_c = 0 \tag{4.7}$$

Here, $b \subset \langle b_0, 1]$ represents the hardening parameter, which is a function of the local internal variable κ

$$b(\kappa) = b_0 + (1 - b_0)\frac{\kappa}{B + \kappa}; \quad \kappa = \frac{2}{\sqrt{3}}\sqrt{J_{2\epsilon^p}} \tag{4.8}$$

while b_0 and B are material constants. It should be noted that in Equation (4.8) $J_{2\epsilon^p}$ represents the second invariant of the plastic strain deviator, so that the hardening effects are attributed to irreversible distortions. The plastic potential surface is assumed in the form

$$\Psi = \sqrt{3}\bar{\sigma} + \eta_c g(\theta)\hat{\sigma}_m \ln\frac{\hat{\sigma}_m}{\hat{\sigma}_m^0} = 0 \tag{4.9}$$

where $\hat{\sigma}_m = c_3 f_0 + \sigma_m$, $\hat{\sigma}_m^0$ is defined from the condition $\Psi = 0$, and η_c represents the value of $\sqrt{3}\bar{\sigma}/g(\theta)\hat{\sigma}_m$ for which a transition from plastic compaction to dilatancy occurs. Assuming that such a transition takes place along the locus

$$\tilde{f} = \sqrt{3}\bar{\sigma} + a g(\theta)\bar{\sigma}_c = 0 \tag{4.10}$$

where a is a material constant, the variable η_c can be determined as (cf. [29])

$$\eta_c = \frac{a e f_0}{2 c_2 \hat{\sigma}_m^0}\left(\sqrt{c_1^2 + \frac{4 c_2}{e f_0}\hat{\sigma}_m^0} - c_1\right) \tag{4.11}$$

where e denotes the Euler's number. Equation (4.9) in conjunction with Equation (4.11) can be solved for η_c by employing the Newton's method. Given now Equations (4.7) and (4.9), the constitutive relation can be formulated using the standard plasticity procedure, i.e. invoking the additivity of elastic and plastic strain rates as well as the consistency condition $\dot{f} = 0$. The details in this respect are provided, for example, in ref. [30].

In order to verify the performance of the approach described above, the experimental data reported in ref. [26] has been employed. The Lac du Bonnet granite used in that study was composed of approx. 30% potassium feldspar, 30% plagioclase, 30% quartz, and 10% mafic minerals. The samples were obtained from 420 Level of AECL's underground research lab in Manitoba. The testing program included uniaxial compression, Brazilian indirect tensile tests as well as over thirty triaxial compression tests.

The identification of material parameters requires, first of all, the specifications of conditions at failure. Based on the information reported in ref. [26], the tensile strength under slow loading rates can be estimated as being close to 7.9 MPa. The

latter, according to Equation (4.4), gives $c_3 = 7.9$ for $f_0 = 1\,\text{MPa}$. The remaining strength parameters were then assessed using the best-fit approximation to the triaxial data. Figure 4.1 presents the peak strength envelope incorporating the representation (4.4). Note that in this case, some additional results from the tests conducted in ref. [31] have also been included for the purpose of comparison. The obtained coefficients of approximation are $c_1 = 0.35$ and $c_2 = 1.64 \times 10^{-4}$.

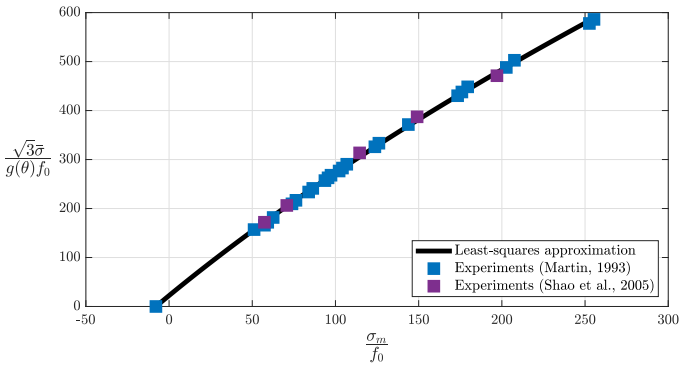

Figure 4.1: The failure envelope, Equation (4.4), for the Lac du Bonnet granite (Level 420 of URL)

The modeling of deformation characteristics entails the specification of elastic constants (E, ν) as well as the parameters governing the hardening law (4.8), i.e. (b_0, B), and the transition to dilatancy a. Based on the results reported in ref. [26], the following values were assumed

$$E = 60\,\text{GPa}, \quad \nu = 0.14, \quad b_0 = 0.8, \quad a = 0.73, \quad B = 1.12 \times 10^{-4}$$

Note that the value of parameter B was assessed by trial and error to obtain a good approximation to the deviatoric stress-strain characteristics.

The onset of localization may be considered as a bifurcation problem. Bifurcation

refers to inception of a nonhomogeneous deformation mode which is typically associated with formation of a discrete shear band. The most widely used criterion for localization in geomaterials is that developed in ref. [32]. In the context of infinitesimal deformation, the condition for strain localization takes the form

$$\det A_{jk} = \det n_i D_{ijkl} n_l = 0 \tag{4.12}$$

where D_{ijkl} is the elastoplastic constitutive tensor [30] and n_i is the unit normal to the shear band. The onset of bifurcation is said to occur when Equation (4.12) has real roots [33]. Complementary details regarding the bifurcation and shear band analysis in triaxial and biaxial testing configurations are given in ref. [34].

The key results of the numerical analysis are presented in Figures 4.2 and 4.3. Figure 4.2 shows the simulations of a series of triaxial tests reported in ref. [26]. It should be noted that these tests were carried out on samples which were extracted in-situ and thus have already been subjected to some stress paths that might have induced initial damage. In simulating the triaxial tests, this past loading history was not followed, and the early stage of deformation associated with closing of microcracks and the build-up of stiffness was not considered. The analysis was stopped here at the stage when the bifurcation criterion (4.12) was satisfied. At this point, the inhomogeneous deformation associated with strain softening commences, which is shown schematically by an arrow. Note that the post-bifurcation response needs to be considered at the level of a boundary value problem, as addressed in Section 4.2.3. The results of simulations are, in general, in a fairly good agreement with the experimental data. Finally, Figure 4.3 shows a set of bifurcation points obtained for the considered triaxial tests. It should be noted that the bifurcation criterion is, in general, path-dependent, which is in contrast to the functional form (4.4) that

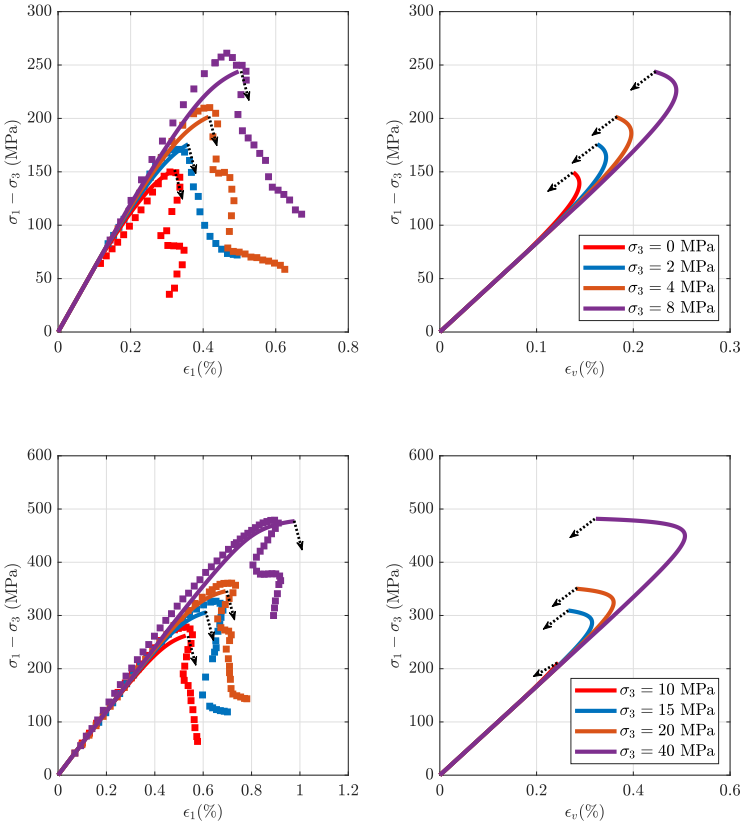

Figure 4.2: Numerical simulations of triaxial compression tests at different confinements; deviatoric and volume change characteristics (exptl. results of ref. [26] are shown using the square symbols)

specifies the conditions at failure. It is evident though that the bifurcation is predicted to occur when the stress state is in close proximity to the postulated failure criterion (4.4). In that sense, the results of bifurcation analysis are quite consistent with the experimental data.

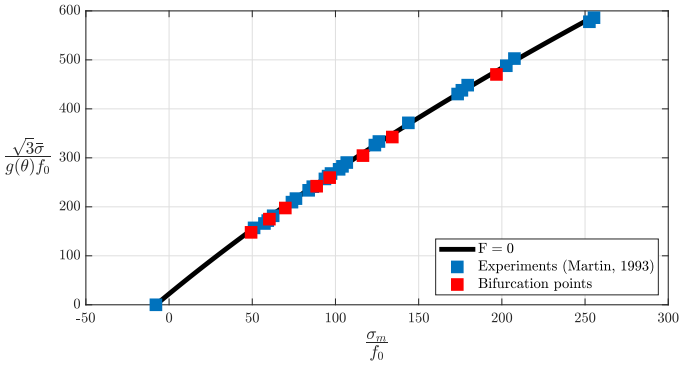

Figure 4.3: The peak strength envelope for the Lac du Bonnet granite

4.2.3 Description of hydromechanical behaviour in the post-localized regime

In the presence of localization, the average mechanical properties within a domain containing macrocracks are assessed by incorporating a constitutive law with embedded discontinuity (CLED, cf. [35]). For this purpose, a referential volume $\Delta\Omega$ is considered, which includes the intact parts $\Delta\Omega^+$ and $\Delta\Omega^-$ intercepted by a fractured region with the surface area $\Delta\Gamma_d$ and the unit normal n_i. In this case, the discontinuous velocity field v_i may be defined as a sum of two continuous functions $\hat{v}_i$ and $\bar{v}_i$ combined with a Heaviside step function. By calculating the velocity gradient and averaging it over the entire referential volume $\Delta\Omega$, the total strain rate may be expressed as [21]

$$\dot{\epsilon}_{ij} = \dot{\epsilon}^{(1)}_{ij} + \chi([\![v_i]\!]n_j)^s \tag{4.13}$$

Here, $\dot{\epsilon}^{(1)}_{ij}$ is the average strain rate in the intact material (viz. subscript (1)), $[\![v_i]\!]$ is the velocity jump across the localized zone and χ is a length scale parameter whose inverse χ^{-1} is defined as the ratio of the referential volume to the surface area of the fractured region (i.e. $\chi^{-1} = \Delta\Omega/\Delta\Gamma_d$).

The localization law, i.e. the relation between the velocity jump $[\![v_i]\!]$ and the macroscopic strain rate $\dot{\epsilon}_{ij}$ may be established by imposing the continuity of traction across the localized region. Thus,

$$\dot{T}_i = \dot{\sigma}_{ij}^{(1)} n_j \simeq \dot{\sigma}_{ij} n_j \;\Rightarrow\; S_{ij}[\![v_j]\!] = D_{ijkl}\dot{\epsilon}_{kl}^{(1)} n_j \tag{4.14}$$

where $\dot{T}_i$ is the traction vector, S_{ij} is the tangential stiffness operator for the fractured zone, and D_{ijkl} is the fourth-order stiffness tensor which defines the properties in the intact region. Combining the above equations and rearranging leads to the localization law in the form

$$[\![v_i]\!] = E_{ip} D_{pqjk} n_q \dot{\epsilon}_{jk};\; E_{ij} = (S_{ij} + \chi D_{ipqj} n_p n_q)^{-1} \tag{4.15}$$

Given now the representation above, the macroscopic stress rate can be defined as

$$\dot{\sigma}_{ij} = \bar{D}_{ijkl}\dot{\epsilon}_{kl};\; \bar{D}_{ijkl} = D_{ijpq}\left(\delta_{pk}\delta_{ql} - \chi n_p E_{qr} D_{rskl} n_s\right) \tag{4.16}$$

Here, $\bar{D}_{ijkl}$ is the equivalent tangential stiffness operator which depends on the properties of both constituents and the scale parameter χ, the latter defined at the finite element level based on the orientation and location of the macrocrack.

As mentioned earlier, the operator D_{ijkl} is calculated using the standard plasticity procedure that incorporates the consistency condition for the yield surface (4.7) together with the strain rate additivity postulate and a non-associated flow rule employing the potential function (4.9). The tangential stiffness operator for the fracture zone, S_{ij}, is also established here within the framework of elasto-plasticity. The yield as well as the potential function are both defined in the local coordinate system (t_i,

$n_i,\ s_i$) attached to the crack. A simple linear form consistent with Coulomb criterion is employed, while the softening (degradation) effects are attributed to tangential component of velocity discontinuity, i.e.

$$f = |\tau| + m(\kappa)\sigma'_n - c = 0;\ \Psi = |\tau| + \eta\sigma'_n;\ \kappa = \int_0^t \sqrt{(t_i[\![v_i^p]\!])^2 + (s_i[\![v_i^p]\!]))^2}\, dt \tag{4.17}$$
$$m(\kappa) = m_r + (m_0 - m_r)\exp(-\omega_1\kappa);\ c(\kappa) = c_0\exp(-\omega_2\kappa)$$

Here (τ, σ'_n) are the shear and normal components of the surface traction, $[\![v_i^p]\!]$ is the plastic part of velocity jump, η is the dilatancy coefficient, m_0 and m_r denote the initial and residual values of the friction coefficient, respectively, c_0 is the cohesion intercept, while ω's control the rate of strength degradation. It should be noted that for newly formed macrocracks, m_0 and c_0 are calculated at the bifurcation point by imposing the condition of $f = 0$.

A conceptually similar averaging procedure may be employed to define the equivalent hydraulic properties within the intact domain intercepted by a fracture. The approach involves imposing a weak discontinuity in fluid pressure within the considered referential volume. By enforcing admissible constraints in the flow regime an average hydraulic conductivity operator can be established, which again incorporates the length scale parameter χ. The homogenized constitutive relation governing the fluid flow within the referential volume adjacent to the localized region takes the form [23]

$$w_i = \frac{1}{\rho_f g}\bar{k}_{ij}(-p_{,j} + \rho_f g_j) \tag{4.18}$$
$$\bar{k}_{ij} = ((1-\chi t_D)k_{iq}^{(1)} + \chi t_D k_{ip}^{(2)}\mathcal{C}_{pq})[\delta_{qj} + \chi t_D(\mathcal{C}_{qj} - \delta_{qj})]^{-1}$$

Here w_i is average superficial velocity of fluid flow, $k_{ij}^{(1)}$ and $k_{ij}^{(2)}$ are the hydraulic

conductivity tensors in the intact and fractured regions, respectively, and t_D is the fracture thickness. In addition, $\mathcal{C}_{ij}$ is an operator which defines the coefficients of the hydraulic constraints, viz.

$$\mathcal{C}_{ij} = \begin{bmatrix} t_i \\ k^{(2)}_{qi} n_q \\ s_i \end{bmatrix}^{-1} \begin{bmatrix} t_j \\ k^{(1)}_{pj} n_p \\ s_j \end{bmatrix} \tag{4.19}$$

where t_i and s_i are the unit vectors along the discontinuity surface.

It has to be noted that the conductivity tensor for the fractured region, $k^{(2)}_{ij}$, is a diagonal operator in the local coordinate system of (t_i, n_i, s_i), whose tangential components of $k^{(2)}_{ij} t_i$ and $k^{(2)}_{ij} s_i$ are assumed to obey the cubic law [36], i.e. $k^{(2)}_{ij} t_i = \frac{g}{12\vartheta} t^2_D t_i$ and $k^{(2)}_{ij} s_i = \frac{g}{12\vartheta} t^2_D s_i$ (where ϑ is the fluid's kinematic viscosity). At the same time, the normal components of the conductivity operators in the intact and fractured regions are assumed to be identical, i.e. $k^{(2)}_{ij} n_i = k^{(1)}_{ij} n_i$.

The constitutive relations (4.16) and (4.18) form the basis for defining the problem of hydro-mechanical interaction in the presence of discontinuous fractures. The onset of new macrocracks and their orientation is assessed through the bifurcation analysis (4.12). The methodology is applicable to various types of rocks but is particularly relevant to in-situ crystalline formations, which are known to contain multiple joints and/or major sparse fracture zones.

4.2.4 CLED finite element formulation for CLED approach

The time interval Θ in Equations (4.1) and (4.2) is divided into a number of incremental steps so that $t = t^{(n)} + \Delta t$, and the backward Euler scheme is used for the temporal discretization of the rate of u_i and p in the balance of mass expression (4.2).

Therefore,

$$\alpha(p - p^{(n)}) + \beta(u_{i,i} - u_{i,i}^{(n)}) + (\Delta t/\rho_f g)(k_{ij}(-p_{,j} + \rho_f g_j))_{,i} \approx 0 \text{ in } \Omega \times \Theta \tag{4.20}$$

In order to provide the finite element implementation based on the calculus of variations, the spaces of admissible solutions ($\mathscr{L}_{\dot{u}}$ and $\mathscr{L}_{\dot{p}}$) and their variations ($\mathscr{T}_{\dot{u}}$ and $\mathscr{T}_{\dot{p}}$) are defined as

$$\begin{aligned}
&\mathscr{L}_{\dot{u}} = \{\dot{u}_i \mid \dot{u}_i \in [C^1(\Omega)]^{dim},\ \dot{u}_i = \dot{u}_i^\star \text{ on } \partial_u\Omega\} \\
&\mathscr{L}_{\dot{p}} = \{\dot{p} \mid \dot{p} \in [C^1(\Omega)],\ \dot{p} = \dot{p}^\star \text{ on } \partial_p\Omega\} \\
&\mathscr{T}_{\dot{u}} = \{\delta\dot{u}_i \mid \delta\dot{u}_i \in [C^1(\Omega)]^{dim},\ \delta\dot{u}_i = 0 \text{ on } \partial_u\Omega\} \\
&\mathscr{T}_{\dot{p}} = \{\delta\dot{p} \mid \delta\dot{p} \in [C^1(\Omega)],\ \delta\dot{p} = 0 \text{ on } \partial_p\Omega\}
\end{aligned} \tag{4.21}$$

where C^1 stands for the Sobolev space of order 1.

The mixed field $(u - p)$ finite element formulation originates from weak forms of the local balance equations. In this case, multiplying Equations (4.1) and (4.20) by $\delta\dot{u}_i$ and $\delta\dot{p}$, integrating over the entire domain Ω, and applying the Gauss theorem together with the Neumann boundary conditions (Equations (4.3)c and (4.3)d), leads to the following weak statements

$$\int_\Omega \Big[\delta\dot{\epsilon}_{ij}\sigma'_{ij} - \beta(\delta\dot{u}_{i,i})p - \rho(\delta\dot{u}_i)g_i\Big]\, d\Omega - \int_{\partial_t\Omega}(\delta\dot{u}_i)T_i^\star\, d\Gamma = 0 \tag{4.22}$$

$$\begin{aligned}
&\int_\Omega \Big[\alpha(\delta\dot{p})p^{(n)} + \beta(\delta\dot{p})u_{i,i}^{(n)} - \alpha(\delta\dot{p})p - \beta(\delta\dot{p})u_{i,i}\Big]\, d\Omega \\
&+ \int_\Omega \Big[-\tfrac{\Delta t}{\rho_f g}(\delta\dot{p}_{,i})\bar{k}_{ij}p_{,j} + \tfrac{\Delta t}{g}(\delta\dot{p}_{,i})\bar{k}_{ij}g_j\Big]\, d\Omega - \int_{\partial_q\Omega}\Delta t(\delta\dot{p})q^\star\, d\Gamma \\
&- \int_\Omega \Big[\tfrac{1}{2G}(\delta\dot{p} - \Pi\delta\dot{p})(p - \Pi p) - \tfrac{1}{2G}(\delta\dot{p} - \Pi\delta\dot{p})(p^{(n)} - \Pi p^{(n)})\Big]\, d\Omega \approx 0
\end{aligned} \tag{4.23}$$

Here, $\delta\dot{\epsilon}_{ij} = (\delta\dot{u}_{i,j})^s$ and $\bar{k}_{ij}$ is the equivalent hydraulic conductivity tensor as defined by Equation (4.18)b. Apparently, in the absence of discontinuities $\bar{k}_{ij}$ reduces to $k_{ij}^{(1)}$, i.e the conductivity in the intact region. It is noted that the last integral in Equation (4.23) is an additional term augmenting the balance of mass in order to stabilize the FE formulation. This expression is based on the Polynomial-Pressure-Projection (PPP) technique developed in ref. [37]. The latter is used to avoid the loss of stability when equal-order interpolation functions are employed in the analysis of porous media that have a very low compressibility and/or permeability (such as crystalline rocks). In Equation (4.23), G is the shear modulus, and Π denotes a projection operator in the PPP stabilization technique. The definition of this operator and the derivation of the mathematical expressions used in the PPP technique are given in ref. [37].
In Equations (4.22) and (4.23), σ'_{ij}, u_i, p, and $\bar{k}_{ij}$ can be written as

$$\sigma'_{ij} = \sigma'^{(i)}_{ij} + \bar{D}_{ijkl}\dot{\epsilon}_{kl}dt \tag{4.24}$$
$$u_i = u_i^{(i)} + \dot{u}_i dt$$
$$p = p^{(i)} + \dot{p}dt$$
$$\bar{k}_{ij} = \bar{k}_{ij}^{(i)} + \dot{\bar{k}}_{ij}dt$$

where $\sigma'_{ij} := \sigma'^{(i+1)}_{ij}$, $u_i := u_i^{(i+1)}$, $p := p^{(i+1)}$, and $\bar{k}_{ij} := \bar{k}_{ij}^{(i+1)}$, and the equivalent stiffness operator $\bar{D}_{ijkl}$ is defined in Equation (4.16). Furthermore, the change in equivalent hydraulic conductivity during the ongoing deformation may be expressed in the form [24],

$$\dot{\bar{k}}_{ij} = \zeta_{ijkl}\dot{\epsilon}_{kl}dt \tag{4.25}$$

where ζ_{ijkl} is a minor symmetric fourth-order tensor ($\zeta_{ijkl} = \zeta_{jikl} = \zeta_{jilk} = \zeta_{ijlk}$) which

is defined as [24]

$$\zeta_{ijkl} = \frac{\partial \bar{k}_{ij}}{\partial t_D} n_m \left(S_{mn} + \chi n_o D_{omnp} n_p\right)^{-1} n_q D_{nqkl} \tag{4.26}$$

Thus, it is evident that the change in the deformation field affects the fluid transmissivity which, in turn, influences the velocity of flow and the generation of pore-fluid pressure. Substituting now Equation (4.24) into Equations (4.22) and (4.23), the following statements are obtained

$$\begin{aligned}
&\int_\Omega \left[\delta\dot{\epsilon}_{ij}\ \bar{D}_{ijkl}\ \delta\dot{\epsilon}_{kl} dt + \delta\dot{\epsilon}_{ij}\sigma'^{(i)}_{ij}\right]\ d\Omega \qquad (4.27)\\
&- \int_\Omega \left[\beta\delta\dot{u}_{i,i}\dot{p} dt + \beta\delta\dot{u}_{i,i}p^{(i)} + \rho\delta\dot{u}_i g_i\right]\ d\Omega - \int_{\partial_t\Omega} \delta\dot{u}_i T^\star_i\ d\Gamma = 0\\
&\int_\Omega \left[\alpha\delta\dot{p}(p^{(n)} - p^{(i)}) + \beta\delta\dot{p}(u^{(n)}_{i,i} - u^{(i)}_{i,i}) - \alpha\delta\dot{p}\dot{p} dt - \beta\delta\dot{p}\dot{u}_{i,i} dt\right]\ d\Omega \qquad (4.28)\\
&+ \int_\Omega \Big[- \tfrac{\Delta t}{\rho_f g}(\delta\dot{p}_{,i}p^{(i)}_{,j} + \delta\dot{p}_{,j}p^{(i)}_{,i})\zeta_{ijkl}\delta\dot{\epsilon}_{kl} dt - \tfrac{\Delta t}{\rho_f g}\delta\dot{p}_{,i}\bar{k}^{(i)}_{ij}p^{(i)}_{,j}\Big]\ d\Omega\\
&+ \int_\Omega \Big[- \tfrac{\Delta t}{\rho_f g}\delta\dot{p}_{,i}\bar{k}^{(i)}_{ij}\dot{p}_{,j} dt + \tfrac{\Delta t}{\rho_f g}(\delta\dot{p}_{,i}g_j + \delta\dot{p}_{,j}g_i)\zeta_{ijkl}\delta\dot{\epsilon}_{kl} dt\Big]\ d\Omega\\
&+ \int_\Omega \tfrac{\Delta t}{g}\delta\dot{p}_{,i}\bar{k}^{(i)}_{ij} g_j\ d\Omega - \int_{\partial_q\Omega} \Delta t\delta\dot{p}q^\star\ d\Gamma\\
&- \int_\Omega \left[\tfrac{1}{2G}(\delta\dot{p} - \Pi\delta\dot{p})(\dot{p} - \Pi\dot{p}) dt + \tfrac{1}{2G}(\delta\dot{p} - \Pi\delta\dot{p})(p^{(i)} - \Pi p^{(i)})\right]\ d\Omega\\
&+ \int_\Omega \tfrac{1}{2G}(\delta\dot{p} - \Pi\delta\dot{p})(p^{(n)} - \Pi p^{(n)})\ d\Omega \approx 0
\end{aligned}$$

According to the calculus of variations, the weak forms of the governing equations require finding $\dot{u}_i \in \mathscr{L}_{\dot{u}}$ and $\dot{p} \in \mathscr{L}_{\dot{p}}$ such that

$$\begin{aligned}
\delta F_{\dot{u}} = \delta\Bigg(&\int_\Omega \left[\tfrac{1}{2}\delta\dot{\epsilon}_{ij}\ \bar{D}_{ijkl}\ \delta\dot{\epsilon}_{kl} dt + \delta\dot{\epsilon}_{ij}\sigma'^{(i)}_{ij}\right]\ d\Omega \qquad (4.29)\\
&- \int_\Omega \left[\beta\dot{u}_{i,i}\dot{p} dt + \beta\dot{u}_{i,i}p^{(i)} + \rho\dot{u}_i g_i\right]\ d\Omega - \int_{\partial_t\Omega} \dot{u}_i T^\star_i\ d\Gamma\Bigg) = 0
\end{aligned}$$

$$\delta F_{\dot{p}} = \delta\Bigg(\int_\Omega \Big[\alpha\dot{p}(p^{(n)} - p^{(i)}) + \beta\dot{p}(u^{(n)}_{i,i} - u^{(i)}_{i,i}) - \tfrac{\alpha}{2}\dot{p}\dot{p}dt - \beta\dot{p}\dot{u}_{i,i}dt\Big]\, d\Omega \tag{4.30}$$
$$+ \int_\Omega \Big[-\tfrac{\Delta t}{\rho_f g}(\dot{p}_{,i}p^{(i)}_{,j} + \dot{p}_{,j}p^{(i)}_{,i})\zeta_{ijkl}\delta\dot{\epsilon}_{kl}dt - \tfrac{\Delta t}{\rho_f g}\dot{p}_{,i}\bar{k}^{(i)}_{ij}p^{(i)}_{,j}\Big]\, d\Omega$$
$$+ \int_\Omega \Big[-\tfrac{\Delta t}{2\rho_f g}\dot{p}_{,i}\bar{k}^{(i)}_{ij}\dot{p}_{,j}dt + \tfrac{\Delta t}{\rho_f g}(\dot{p}_{,i}g_j + \dot{p}_{,j}g_i)\zeta_{ijkl}\delta\dot{\epsilon}_{kl}dt\Big]\, d\Omega$$
$$+ \int_\Omega \tfrac{\Delta t}{g}\dot{p}_{,i}\bar{k}^{(i)}_{ij}g_j\, d\Omega - \int_{\partial_q\Omega} \Delta t\dot{p}q^\star\, d\Gamma$$
$$- \int_\Omega \Big[\tfrac{1}{4G}(\dot{p} - \Pi\dot{p})(\dot{p} - \Pi\dot{p})dt + \tfrac{1}{2G}(\dot{p} - \Pi\dot{p})(p^{(i)} - \Pi p^{(i)})\Big]\, d\Omega$$
$$+ \int_\Omega \tfrac{1}{2G}(\dot{p} - \Pi\dot{p})(p^{(n)} - \Pi p^{(n)})\, d\Omega\Bigg) \approx 0$$

Equations (4.27) and (4.28) can be transformed into a discrete linear system of equations by spatial discretization of the domain Ω, i.e. by employing non-overlapping finite elements for partitioning this domain. In this case, the standard Galerkin approximation [38] is typically used which, in Voigt (matrix) notation, takes the form

$$\{\boldsymbol{u}\} = [\boldsymbol{N_u}]\{\widetilde{\boldsymbol{u}}\}; \quad \{\boldsymbol{du}\} = [\boldsymbol{N_u}]\{\dot{\widetilde{\boldsymbol{u}}}\}dt = [\boldsymbol{N_u}]\{\widetilde{\boldsymbol{du}}\} \tag{4.31}$$
$$\{\boldsymbol{p}\} = \{\boldsymbol{N_p}\}\{\widetilde{\boldsymbol{p}}\}; \quad \{\boldsymbol{dp}\} = \{\boldsymbol{N_p}\}\{\dot{\widetilde{\boldsymbol{p}}}\}dt = \{\boldsymbol{N_p}\}\{\widetilde{\boldsymbol{dp}}\}$$

where $\{\widetilde{\boldsymbol{u}}\}$, $\{\widetilde{\boldsymbol{p}}\}$, $\{\widetilde{\boldsymbol{du}}\}$, and $\{\widetilde{\boldsymbol{dp}}\}$ denote the nodal values of the respective variables, while $[\boldsymbol{N_u}]$ and $\{\boldsymbol{N_p}\}$ are suitable interpolation (shape) functions. In the context of Newton-Raphson scheme, for $t : t^{(n)} \to t^{(n)} + \Delta t$ the following system of linear algebraic equations at iteration (i) is obtained by substituting Equation (4.31) into Equations (4.27) and (4.28)

$$\begin{bmatrix} \boldsymbol{K} & \boldsymbol{L} \\ \boldsymbol{M} & \boldsymbol{N} \end{bmatrix}^{(i)} \begin{Bmatrix} \widetilde{\boldsymbol{du}} \\ \widetilde{\boldsymbol{dp}} \end{Bmatrix} = \begin{Bmatrix} \boldsymbol{R_1} \\ \boldsymbol{R_2} \end{Bmatrix}^{(i)}; \qquad \begin{Bmatrix} \widetilde{\boldsymbol{u}} \\ \widetilde{\boldsymbol{p}} \end{Bmatrix}^{(i+1)} = \begin{Bmatrix} \widetilde{\boldsymbol{u}} \\ \widetilde{\boldsymbol{p}} \end{Bmatrix}^{(i)} + \begin{Bmatrix} \widetilde{\boldsymbol{du}} \\ \widetilde{\boldsymbol{dp}} \end{Bmatrix} \tag{4.32}$$

where

$$
\begin{aligned}
\boldsymbol{R_1} &= \int_{\partial_t \Omega} [\boldsymbol{N_u}]^T \{\boldsymbol{T^\star}\}\ d\Gamma + \int_\Omega \rho [\boldsymbol{N_u}]^T \{\boldsymbol{g}\}\ d\Omega - \int_\Omega [\boldsymbol{L N_u}]^T \{\boldsymbol{\sigma'}\}^{(i)}\ d\Omega \\
&\quad + \left[\int_\Omega \beta [\boldsymbol{L N_u}]^T \{\boldsymbol{m}\}\{\boldsymbol{N_p}\}\ d\Omega\right] \{\widetilde{\boldsymbol{p}}\}^{(i)} \\
\boldsymbol{R_2} &= \int_{\partial_q \Omega} \Delta t \{\boldsymbol{N_p}\}^T q^\star\ d\Gamma + \left[\int_\Omega \beta \{\boldsymbol{N_p}\}^T \{\boldsymbol{m}\}^T [\boldsymbol{L N_u}]\ d\Omega\right] \left(\{\widetilde{\boldsymbol{u}}\}^{(i)} - \{\widetilde{\boldsymbol{u}}\}^{(n)}\right) \\
&\quad + \left[\int_\Omega \alpha \{\boldsymbol{N_p}\}^T \{\boldsymbol{N_p}\}\ d\Omega + \int_\Omega \tfrac{1}{2G} (\{\boldsymbol{N_p}\}^T - \Pi \{\boldsymbol{N_p}\}^T)(\{\boldsymbol{N_p}\} - \Pi \{\boldsymbol{N_p}\})\ d\Omega\right] \\
&\quad \left(\{\widetilde{\boldsymbol{p}}\}^{(i)} - \{\widetilde{\boldsymbol{p}}\}^{(n)}\right) + \left[\int_\Omega \tfrac{\Delta t}{\rho_f g} [\boldsymbol{\nabla N_p}]^T [\bar{\boldsymbol{k}}]^{(i)} [\boldsymbol{\nabla N_p}]\ d\Omega\right] \{\widetilde{\boldsymbol{p}}\}^{(i)} \\
&\quad - \int_\Omega \tfrac{\Delta t}{g} [\boldsymbol{\nabla N_p}]^T [\bar{\boldsymbol{k}}]^{(i)} \{\boldsymbol{g}\}\ d\Omega \\
\boldsymbol{K} &= \int_\Omega [\boldsymbol{L N_u}]^T [\bar{\boldsymbol{D}}] [\boldsymbol{L N_u}]\ d\Omega \\
\boldsymbol{L} &= -\int_\Omega \beta [\boldsymbol{L N_u}]^T \{\boldsymbol{m}\}\{\boldsymbol{N_p}\}\ d\Omega \\
\boldsymbol{M} &= -\int_\Omega \beta \{\boldsymbol{N_p}\}^T \{\boldsymbol{m}\}^T [\boldsymbol{L N_u}]\ d\Omega - \int_\Omega \tfrac{\Delta t}{\rho_f g} [\Xi \boldsymbol{\nabla p}^{(i)}] [\boldsymbol{L N_u}]^T [\boldsymbol{Z}]^{(i)} [\boldsymbol{L N_u}]\ d\Omega \\
&\quad + \int_\Omega \tfrac{\Delta t}{g} [\Xi \boldsymbol{g}] [\boldsymbol{L N_u}]^T [\boldsymbol{Z}]^{(i)} [\boldsymbol{L N_u}]\ d\Omega \\
\boldsymbol{N} &= -\int_\Omega \alpha \{\boldsymbol{N_p}\}^T \{\boldsymbol{N_p}\}\ d\Omega - \int_\Omega \tfrac{\Delta t}{\rho_f g} [\boldsymbol{\nabla N_p}]^T [\bar{\boldsymbol{k}}]^{(i)} [\boldsymbol{\nabla N_p}]\ d\Omega \\
&\quad - \int_\Omega \tfrac{1}{2G} (\{\boldsymbol{N_p}\}^T - \Pi \{\boldsymbol{N_p}\}^T)(\{\boldsymbol{N_p}\} - \Pi \{\boldsymbol{N_p}\})\ d\Omega
\end{aligned}
\tag{4.33}
$$

In the expressions above, $[\boldsymbol{L}]$ is a matrix of the gradient operator specifying the kinematic strain-displacement relations, $[\boldsymbol{\nabla N_p}]$ is a matrix which defines the relation between the pressure gradient and the nodal values of fluid pressure, $\{\boldsymbol{m}\}^T$ equals $\{1, 1, 1, 0, 0, 0\}$. Moreover, Ξ is an operator which, when applied to an arbitrary column vector $\mathbf{v}$, generates a diagonal matrix whose elements are $\mathbf{v}^T$.

It should be noted that numerical integration in Equation (4.33) is carried out

using Gaussian quadrature methods. The governing constitutive relations, viz. Equation (4.16), which incorporate a plasticity formulation, are integrated using an implicit scheme incorporating the cutting-plane algorithm for return-mapping (cf. [39]). The operators $[\boldsymbol{Z}]$ and $[\bar{\boldsymbol{k}}]$, as well as the fracture thickness obtained at the iteration (i), are all updated as

$$
\begin{aligned}
&[\boldsymbol{Z}]^{(i)} = \{\tfrac{\partial \bar{\boldsymbol{k}}}{\partial \boldsymbol{t_D}}\}^{(i-1)}\{\boldsymbol{n}\}^T\Big[[\boldsymbol{S}]^{(i)} + \chi[\boldsymbol{n}]^T[\boldsymbol{D}]^{(i)}[\boldsymbol{n}]\Big]^{-1}[\boldsymbol{n}]^T[\boldsymbol{D}]^{(i)} \qquad (4.34)\\
&\{\bar{\boldsymbol{k}}\}^{(i)} = \{\bar{\boldsymbol{k}}\}^{(i-1)} + [\boldsymbol{Z}]^{(i)}\{\boldsymbol{d\epsilon}\}\\
&t_D^{(i)} = t_D^{(i-1)} + \{\boldsymbol{n}\}^T\Big[[\boldsymbol{S}]^{(i)} + \chi[\boldsymbol{n}]^T[\boldsymbol{D}]^{(i)}[\boldsymbol{n}]\Big]^{-1}[\boldsymbol{n}]^T[\boldsymbol{D}]^{(i)}\{\boldsymbol{d\epsilon}\}
\end{aligned}
$$

Here $\{\bar{\boldsymbol{k}}\}$ and $\{\boldsymbol{d\epsilon}\}$ are the vectors representing the hydraulic conductivity and the strain increment, respectively, while $[\boldsymbol{Z}]$ is a 6×6 matrix (for a 3D configuration). The components of $\{\frac{\partial \bar{\boldsymbol{k}}}{\partial \boldsymbol{t_D}}\}$ appearing in the expression for $[\boldsymbol{Z}]$ are explicitly defined in ref. [24].

4.3 Numerical examples

The numerical analysis presented here deals with uniaxial plane strain compression of sparsely fractured dry and fully saturated samples of Lac du Bonnet granite. The simulations take into account the pre-existing fractures and the onset and propagation of new macrockraks, as well as the evolution of localization-induced changes in hydraulic conductivity. The analysis has been carried out using the formulation outlined in Section 4.2.4. The finite element mesh incorporated bilinear quadrilateral elements for both the displacement and pressure fields. The finite element code, including the component for visualization of the results, was written in MATLAB R2020b.

The mechanical properties of intact Lac du Bonnet granite have been described

using the plasticity framework provided in Section 4.2.2. The onset of localization was considered as a bifurcation problem (cf. [32,34]) and in the post-localization regime, the CLED formulation, viz. Section 4.2.3, was employed. The numerical simulations discussed here were completed using the set of material parameters for *intact* Lac du Bonnet granite that were identified earlier (cf. Section 4.2.2). For convenience, these parameters are listed in Table 4.1. For the fracture zone, the following mechanical properties have been assigned: $m_0 = 0.8$, $m_r = 0.6m_0$, $c_0 = 0.01$ MPa, $\omega_1 = \omega_2 = 0.01$ mm^{-1}.

Table 4.1: Mechanical properties of the *intact* Lac du Bonnet granite

Parameter	Value	Unit
E	60	GPa
ν	0.14	-
f_0	1	MPa
c_1	0.35	-
c_2	1.64E-4	-
c_3	7.9	-
a	0.73	-
B	1.12E-4	-
b_0	0.8	-

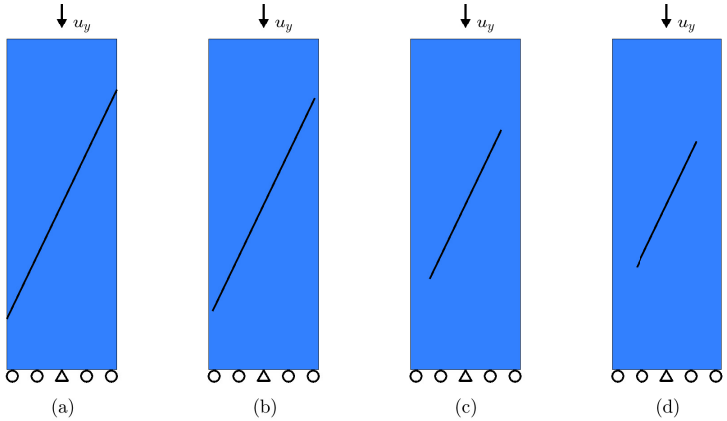

Figure 4.4: Sample geometry and the boundary conditions. The length of inclined fracture: (a) L = 462 mm; (b) L = 439 mm; (c) L = 300 mm; (d) L = 254 mm

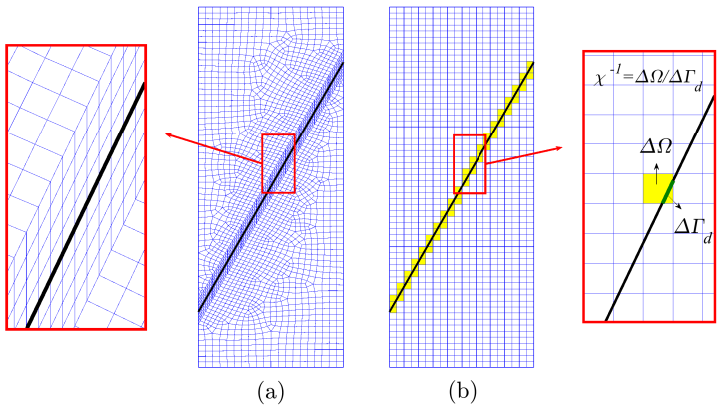

Figure 4.5: Finite element discretization (a) Interface elements; (b) CLED

4.3.1 Plane strain compression in the presence of a dominant fracture

The first example provided here involves simulations of a plane-strain uniaxial compression test. The analyzed samples had the dimension of 20 cm $\times$ 60 cm and contained a pre-existing fracture of different length and the same orientation. All simulations were conducted under displacement-controlled conditions. The geometry of the problem and boundary conditions are shown in Figure 4.4. One of the objectives of this analysis was to validate the CLED approach against that employing zero-thickness interface elements (IE). The latter study incorporated the formulation outlined in refs. [13,14] was conducted for the case of fully developed fracture intercepting the vertical boundaries (cf. Figure 4.4a). Note that all the remaining cases, viz. Figs. 4.4b-d, involve propagation of the pre-existing crack prior to reaching the ultimate load. Such a scenario cannot be efficiently modelled within the IE formulation, so that this part of analysis was conducted based only on the CLED approach. The IE framework is described in Appendix A (Section 4.6) using the format that is consistent with that employed for CLED. The finite element discretization, for both the CLED and IE methodologies, is shown in Figure 4.5. In the former case, a simple structured mesh

was employed incorporating 1,200 elements. In this case, for the elements containing the fracture, the length scale parameter χ, Equation (4.13), was assessed based on its location and orientation within the element (cf. Figure 4.5b). For the IE approach, a fine unstructured mesh with 2,588 elements was used (cf. Figure 4.5a).

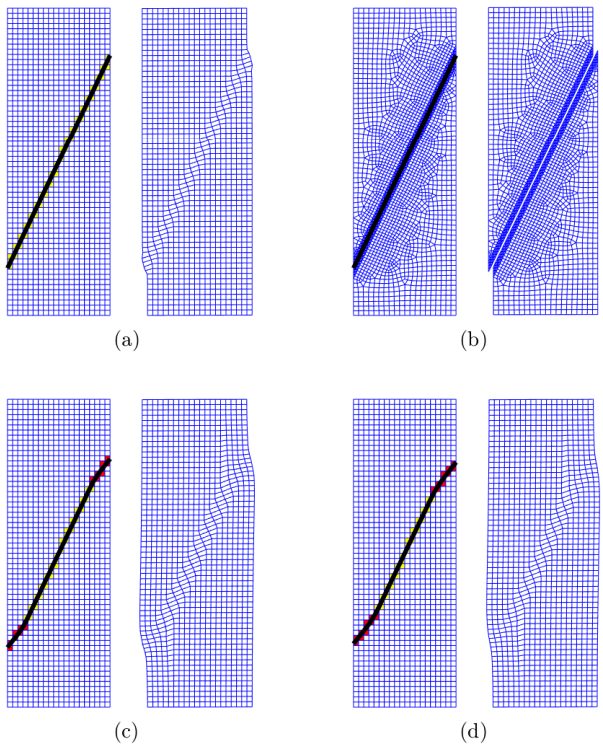

Figure 4.6: Crack propagation and the deformation pattern: (a) CLED, L = 462 mm; (b) IE, L = 462 mm; (c) CLED, L = 300 mm; (d) CLED, L = 254 mm

The main results of numerical simulations are shown in Figures 4.6-4.9. The first part of analysis involved examining the response of dry samples. Figure 4.6 shows the fracture pattern and the deformed mesh at the ultimate load, while Figure 4.7 presents the obtained load-displacement characteristics. The results correspond to $\eta = m$ in Equation (4.17), i.e. an associated flow rule, which leads to a dilative behaviour within the fracture zone. It is evident that for the fully developed pre-existing crack (i.e. L = 462 mm), the solutions for IE and CLED are virtually identical in terms of assessment of ultimate load as well as the deformation pattern. For shorter initial cracks (Figures

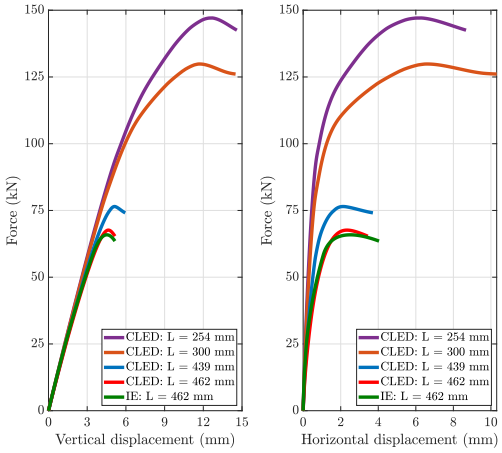

Figure 4.7: Vertical and horizontal deformation (mm) versus axial force (kN)

4.4b-d), further propagation takes place as the deformation progresses. In this case, the strength significantly increases with the decrease in the length of pre-existing fracture.

In the second part of this study, an undrained analysis for the same set of sample geometries was conducted. The samples were assumed to be fully saturated, however the external boundaries were considered as impervious, so that the outward drainage was prevented. The simulations were carried out assuming that the hydraulic conductivity of the intact material was $k_{ij}^{(1)} = 1 \times 10^{-13} \delta_{ij}$ (m/s), the initial fracture aperture was $t_D = 0.1$ mm, while the Biot coefficient and the parameter α, viz. Equation (4.2), were equal to $\beta = 0.3$, and $\alpha = 0.01$ GPa^{-1}. The load-displacement characteristics corresponding to different fracture lengths are provided in Figure 4.8, while Figure 4.9 shows the distribution of fluid pressure at the end of analysis. The simulations employed again an associated flow rule, i.e. $\eta = m$ in Equation (4.17), which led to a generation of significant negative pore pressure within the fracture zone. As a result of this, the mechanical load-displacement curves remained stable, with no indication of the sample reaching the ultimate strength. This is consistent with the existing

experimental evidence (cf. [40]) and indicates that in this case the most likely source of sample failure is the cavitation. The latter is associated with formation of small vapour-filled cavities in the liquid resulting in partial saturation that may trigger the loss of mechanical stability.

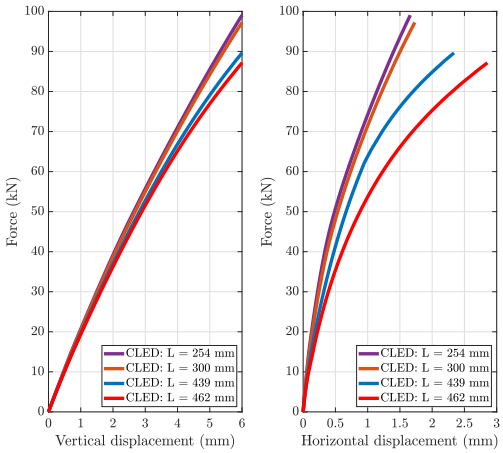

Figure 4.8: Undrained analysis: vertical and horizontal deformation (mm) versus axial force (kN)

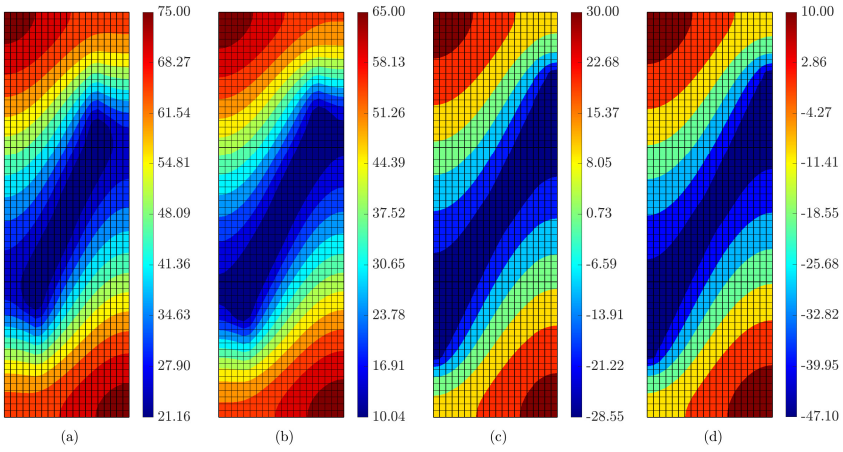

Figure 4.9: Pore-fluid distribution (MPa) in undrained samples with different fracture lengths: (a) L=254 mm; (b) L=300 mm; (c) L = 439 mm; (d) L = 462 mm

4.3.2 Plane strain compression of sparsely fractured samples of Lac du Bonnet granite

This study involved simulation of series of plane-strain uniaxial compression tests conducted on samples of Lac du Bonnet granite containing a set of sparsely distributed fractures. The first part of analysis was focused on both dry and undrained conditions. The undrained tests involved again fully saturated samples subjected to axial load under the constraint of zero flux at the outer boundaries. In this case, the effect of dilatancy has been studied by considering both associated ($\eta = m$) and non-associated flow rules for the fracture zone. For dry samples, the displacement as well as the load-controlled simulations were conducted, and the results compared. The geometry of the problem and the finite element mesh, which incorporated 1,200 bilinear quadrilateral elements, are shown in Figure 4.10. Once again, the inception of new macrocracks, which lead to coalescence of the initial set of fractures, was detected by the bifurcation analysis.

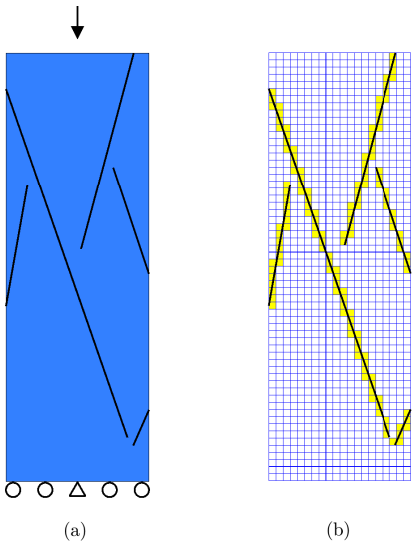

Figure 4.10: (a) Geometry and (b) finite element mesh for a sample with a sparse discrete fracture network

Figure 4.11a shows the load-displacement curves obtained for both the dry sample

and the undrained conditions. For dry sample, the prediction of ultimate strength is virtually identical for the load and displacement-controlled scenarios. It is evident, however, that in the latter case, the simulations could continue into the post-peak regime associated with a descending branch. In case of undrained deformation, the mechanical characteristics are similar to those obtained for a single dominant crack (viz. Figure 4.8), i.e. the response is stable with no indication of the sample reaching the ultimate load. The stable response is again the result of a build up of negative excess of fluid pressure within the fractures undergoing irreversible deformation. The simulations were conducted here using an associated flow rule as well as a non-associated one with the angle of dilatancy $\psi = 0.1\phi$, where ϕ is the friction angle. The former case (i.e. associated flow) resulted in a higher stiffness which may be attributed to more pronounced plastic dilatancy within the active fracture zones.

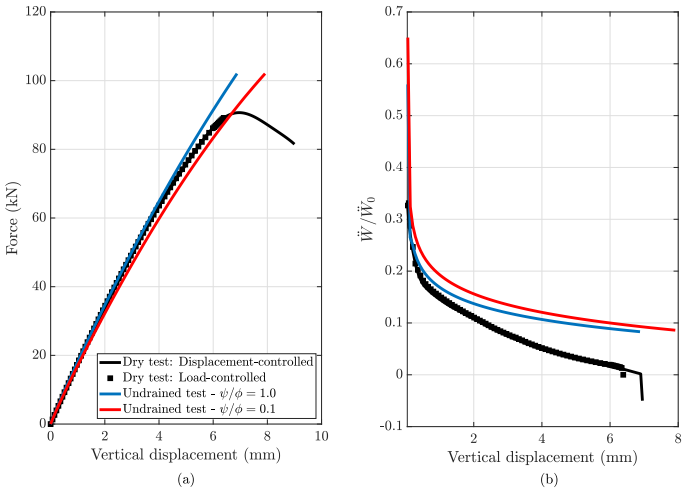

Figure 4.11: (a) Load-vertical displacement curves and (b) evolution of the second rate of internal work normalized by $\ddot{\mathrm{w}}_0 = \int_\Omega D^e_{ijkl}\dot{\epsilon}_{ij}\dot{\epsilon}_{kl}\ d\Omega$

It should be noted that the onset of physical instability in a boundary-value problem may be assessed by examining the second rate of internal work (cf. [41]). The stability of the system is associated with a positive value, i.e. $\ddot{\mathrm{w}} > 0$, while the onset

of instability corresponds to $\ddot{\mathrm{w}} = 0$. In a saturated porous medium, the rate of internal work, under a homogeneous distribution of porosity and fluid density, may be expressed as [23]

$$\rho\dot{e} = \sigma'_{ij}\dot{\epsilon}_{ij} + \alpha\dot{p}p \tag{4.35}$$

where e denotes the stored internal energy density and α is a constant appearing in the balance equation (4.2). Taking the time derivative of Equation (4.35) under a slow process (i.e. $\ddot{\epsilon}_{ij} = 0$, $\ddot{p} = 0$) and integrating over the entire domain gives

$$\ddot{\mathrm{w}} = \int_{\Omega} \rho\ddot{e}\ d\Omega = \int_{\Omega} \dot{\sigma}'_{ij}\dot{\epsilon}_{ij}\ d\Omega + \int_{\Omega} \alpha\dot{p}^2\ d\Omega \tag{4.36}$$

In Figure 4.11b, the load-displacement curves are supplemented by the evolution of the normalized value of the second rate of work. It is seen that for a dry sample, this variable gradually decreases reaching zero as the ultimate load is attained. On the other hand, for undrained tests the second rate of internal work approaches a positive value, which is indicative of a stable response. In general, the tracing of evolution of $\ddot{\mathrm{w}}$ is particularly useful in a class of problems involving a spontaneous loss of stability, like in the case of a load-controlled scheme.

Figure 4.12 shows the fracture pattern and the distribution of fluid pressure at the end of undrained analysis. It is seen that the propagation of fractures, as indicated in red colour, is quite limited at this stage. For the fluid pressure, the results for associated flow rule are compared here with those corresponding to $\psi = 0.1\phi$. Evidently, the build-up of pore pressure is markedly different. While for the associated flow rule a significant negative excess of pore pressure develops, for $\psi = 0.1\phi$ the average values remain in the positive range. Once again, this stems from the difference in the evolution of volumetric strain within the fracture zones, as implied by the type of flow rule.

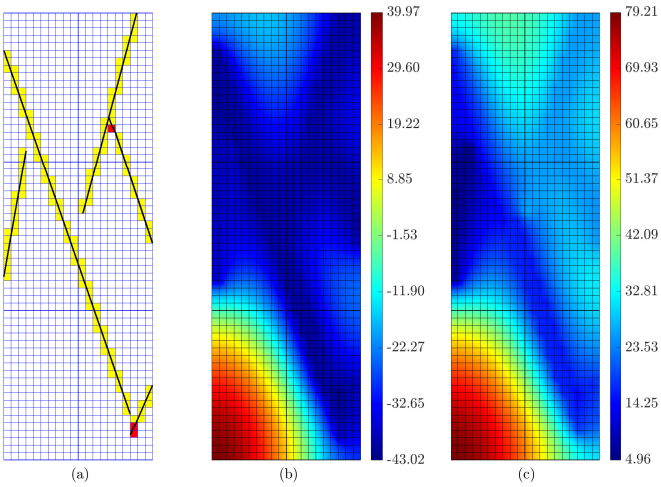

Figure 4.12: (a) Fracture pattern and the distribution of fluid pressure at the end of undrained stage: (b) associated flow rule; (c) non-associated flow rule

The undrained analysis was terminated at the stage when the external load was 15% above the ultimate strength of dry material. At this point, a second stage of the test was simulated in which the drainage out of vertical boundaries of the sample was permitted under a sustained load. This is similar to a consolidation test in which the settlement is triggered by the dissipation of the excess of pore pressure. Figure 4.13 shows the fracture pattern and the distribution of fluid pressure within the domain. During this stage of the test, new macrocracks form coalescing with the pre-existing fractures and the excess of pore pressure progressively reduces (cf. Figure 4.12). This is the case for both associated and non-associated flow rule. As the pore pressure dissipates the surface settlement takes place, as indicated in Figure 4.14. The settlement is significant in case of associated flow, while for non-associated case, it remains at negligibly low level. Soon after the drainage initiates, a rapid increase in the rate of settlement occurs, which is indicative of a spontaneous loss of stability. The latter stems from the fact that the intensity of sustained load is above the ultimate value corresponding to drained conditions. Note again that the loss of

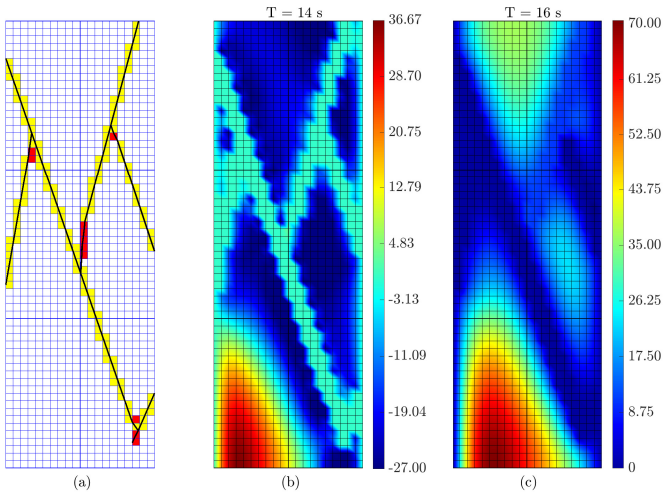

Figure 4.13: Fracture pattern(left) and the distribution of fluid pressure at the end of consolidation stage: (a) associated flow rule; (b) non-associated flow rule

stability, for both associated and non-associated flow rule, occurs at quite early stages of the pore-pressure dissipation process.

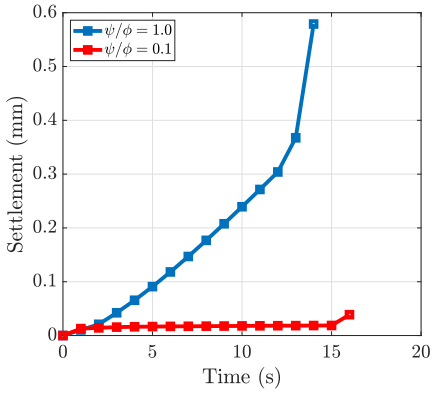

Figure 4.14: Evolution of settlement (mm) during the drainage process at load intensity 15% *above* the ultimate strength of the dry sample

Finally, Figures 4.15 and 4.16 show similar results for the case when drainage occurs at the load intensity which is 15% *below* that corresponding to ultimate strength of the dry sample. In this case, the settlement increases with a progressively decreasing rate. The process continues until stationary conditions are reached. Note

that at this stage of analysis the excess of pore pressure is close to zero. This is evidenced in Figure 4.16 that shows the corresponding pore pressure evolution during the consolidation stage.

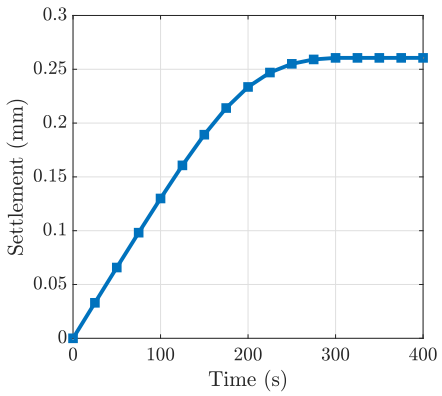

Figure 4.15: Time-history of settlement (mm) during the drainage process at load intensity 15% *below* the ultimate strength of the dry sample

4.4 Final remarks

In this paper, a finite element formulation was developed which incorporates a coupling between the equivalent hydraulic conductivity and the continuing deformation. Evidently, the latter affects the fracture aperture which, in turn, influences the generation of fluid pressure. The approach employed a constitutive law with embedded discontinuity (CLED) for assessing both the hydraulic as well as mechanical properties of the material. The framework was implemented in an FE code developed in MATLAB 2020b and applied to a numerical study involving axial plane strain compression of samples of Lac du Bonnet granite containing discontinuities. The mechanical properties of intact rock were described using a plasticity formulation with deviatoric hardening. The analysis examined the crack propagation and coalescence in both dry and saturated rock.

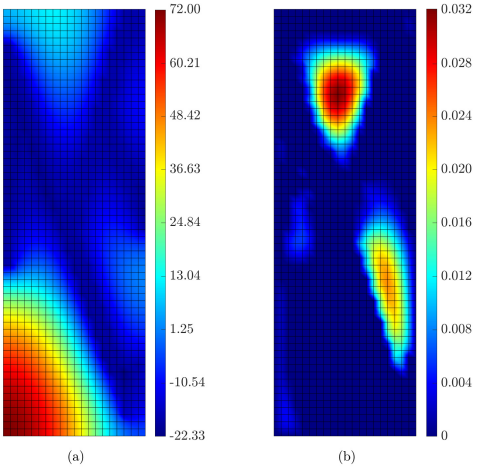

Figure 4.16: Pore-fluid pressure distribution (MPa) at the end of (a) undrained and (b) consolidation stage

The approach was first validated on some benchmark problems that involved the presence of a dominant fracture. The results of CLED approach were compared with those generated using a very fine mesh incorporating interface elements (IE). It was demonstrated that CLED formulation is computationally very efficient and quite accurate in relation to IE approach. It also allows for tracing the crack propagation, which cannot be efficiently done using interface elements. The numerical study indicated that for the dry material the results, particularly in terms of ultimate load, are very sensitive to the length of the dominant pre-existing crack. On the other hand, in case of undrained conditions the response is affected by the flow rule, which impacts the rate of generation of the excess pore pressure. In this case, the load-deformation characteristic remains stable and the most likely source of sample failure is the cavitation.

The analysis employing a dominant crack was supplemented by a comprehensive numerical study involving coupled HM simulations for the case of sparsely distributed fractures. Here, the notion of the loss of stability in a saturated porous medium was

addressed by examining the second rate of internal work. The analysis demonstrated that the propagation of macrocracks and their subsequent coalescence is more pronounced under drained conditions. For undrained deformation, the results were again sensitive to the type of flow rule, indicating a significant build-up of negative excess of pore pressures in case of an associated flow. The simulations involving drainage under a sustained load showed a progressive increase in settlement triggered by dissipation of the pore pressure gradients. When the load intensity was above the ultimate value corresponding to dry conditions, the lateral drainage resulted in a rapid increase in the rate of settlement, which is indicative of a spontaneous loss of stability. In general, the numerical studies conducted here clearly demonstrate the predictive abilities of the CLED approach in assessing both the flow properties and the coupled HM response of crystalline rocks in the presence of both pre-existing and propagating fractures.

4.5 Acknowledgement

The research presented in this paper was supported by the Natural Sciences and Engineering Research Council of Canada (Discovery Grant) and the Canadian Nuclear Safety Commission (CNSC).

4.6 Appendix A: IE formulation

Refering to Figure 4.17, in a dry region containing a discrete fracture, the surface boundaries ($\partial\Omega$) are defined as

$$\emptyset = \partial_u\Omega \cap \partial_t\Omega = \partial_u\Omega \cap \partial_t^d\Omega = \partial_t\Omega \cap \partial_t^d\Omega; \quad \partial\Omega = \partial_u\Omega \cup \partial_t\Omega \cup \partial_t^d\Omega \tag{4.37}$$

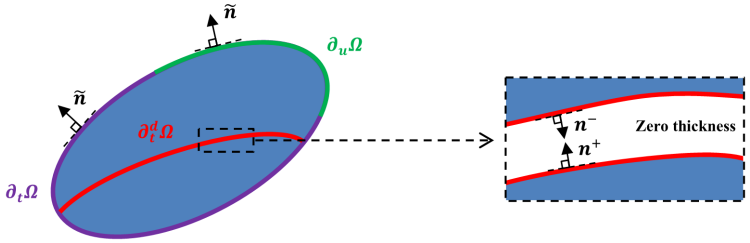

Figure 4.17: External and internal boundary surfaces of a dry domain

Restricting the considerations to static regime, the balance of linear momentum is written as

$$\sigma_{ij,j} + \rho g_i = 0 \quad \text{in} \quad \Omega \tag{4.38}$$

subject to

$$u_i = u_i^\star \quad \text{on} \quad \partial_u\Omega \tag{4.39}$$

$$\sigma_{ij}\tilde{n}_j = T_i^\star \quad \text{on} \quad \partial_t\Omega$$

$$\sigma_{ij}^+ n_j^+ = T_i^+ \quad \text{on} \quad \partial_t^d\Omega$$

$$\sigma_{ij}^- n_j^- = T_i^- \quad \text{on} \quad \partial_t^d\Omega$$

The space of admissible solution ($\mathscr{L}_{\dot{u}}$) and its variation ($\mathscr{T}_{\dot{u}}$) are defined in a way similar to that in Equation (4.21). In this case, multiplying Equations (4.38) by $\delta\dot{u}_i$, integrating over the entire domain Ω, and applying the Gauss theorem together with

the Neumann boundary conditions (Equations (4.39)), leads to the following weak statement

$$\int_{\Omega} \left[\delta\dot{\epsilon}_{ij}\sigma_{ij} - \rho(\delta\dot{u}_i)g_i\right]\, d\Omega - \int_{\partial_t\Omega} (\delta\dot{u}_i)T_i^{\star}\, d\Gamma - \int_{\partial_t^d\Omega} (\delta\dot{u}_i)^{+}T_i^{+}\, d\Gamma \tag{4.40}$$
$$- \int_{\partial_t^d\Omega} (\delta\dot{u}_i)^{-}T_i^{-}\, d\Gamma = 0$$

where $T_i^{-} = -T_i^{+}$ because of the balance of linear momentum. Then,

$$\int_{\Omega} \left[\delta\dot{\epsilon}_{ij}\sigma_{ij} - \rho(\delta\dot{u}_i)g_i\right]\, d\Omega - \int_{\partial_t\Omega} (\delta\dot{u}_i)T_i^{\star}\, d\Gamma + \int_{\partial_t^d\Omega} [\![\delta\dot{u}_i]\!]T_i^{D}\, d\Gamma = 0 \tag{4.41}$$

where T_i^D is the traction at the interface ($T_i^{+} := T_i^D$) and $[\![\delta\dot{u}_i]\!] = (\delta\dot{u}_i)^{-} - (\delta\dot{u}_i)^{+}$ is the jump in the velocity variation. The operators σ_{ij}, T_i^D, and u_i appearing in Equation (4.41), can be expressed as

$$\sigma_{ij} = \sigma_{ij}^{(i)} + D_{ijkl}\dot{\epsilon}_{kl}dt \tag{4.42}$$
$$T_i^D = T_i^{D(i)} + \dot{T}_i^D dt$$
$$u_i = u_i^{(i)} + \dot{u}_i dt$$

where $\sigma_{ij} := \sigma_{ij}^{(i+1)}$, $T_i^D := T_i^{D(i+1)}$, and $u_i := u_i^{(i+1)}$. Furthermore, by analogy to Equation (4.14), $\dot{T}_i^D$ may be defined as

$$\dot{T}_i^D = S_{ij}[\![\dot{u}_j]\!] \tag{4.43}$$

where $[\![\dot{u}_j]\!] = [\![v_j]\!]$ represents the velocity jump, and S_{ij} denotes the tangential stiffness of the macrocracks. Substituting now Equation (4.42) into Equation (4.41), the following statement is obtained

$$\int_{\Omega} \Big[\delta\dot{\epsilon}_{ij}\ D_{ijkl}\ \delta\dot{\epsilon}_{kl}dt + \delta\dot{\epsilon}_{ij}\sigma_{ij}^{(i)}\Big]\ d\Omega \tag{4.44}$$
$$+ \int_{\partial_t^d\Omega} \Big[[\![\delta\dot{u}_i]\!]S_{ij}[\![\dot{u}_j]\!]dt + [\![\delta\dot{u}_i]\!]T_i^{D(i)}\Big]\ d\Gamma - \int_{\Omega}\rho\delta\dot{u}_i g_i\ d\Omega - \int_{\partial_t\Omega}\delta\dot{u}_i T_i^{\star}\ d\Gamma = 0$$

According to the calculus of variations, the weak form of the Equation (4.38) requires finding $\dot{u}_i \in \mathscr{L}_{\dot{u}}$ such that

$$\delta F_{\dot{u}} = \delta\Bigg(\int_{\Omega}\Big[\tfrac{1}{2}\delta\dot{\epsilon}_{ij}\ \bar{D}_{ijkl}\ \delta\dot{\epsilon}_{kl}dt + \delta\dot{\epsilon}_{ij}\sigma_{ij}^{\prime(i)}\Big]\ d\Omega \tag{4.45}$$
$$+ \int_{\partial_t^d\Omega}\Big[\tfrac{1}{2}[\![\dot{u}_i]\!]S_{ij}[\![\dot{u}_j]\!]dt + [\![\dot{u}_i]\!]T_i^{D(i)}\Big]\ d\Gamma - \int_{\Omega}\rho\dot{u}_i g_i\ d\Omega - \int_{\partial_t\Omega}\dot{u}_i T_i^{\star}\ d\Gamma\Bigg) = 0$$

Equation (4.44) can be transformed into a discrete linear system of equations by spatial discretization of the domain Ω, i.e. by using non-overlapping finite elements for partitioning the domain Ω. Non-overlapping finite elements conformal to the fracture surfaces are used when the interfaces are at the edge of two adjacent elements [13]. In this case, the standard Galerkin approximation [13,42] is typically employed, which takes the form

$$\{\boldsymbol{u}\} = [\boldsymbol{N_u}]\{\widetilde{\boldsymbol{u}}\};\quad \{\boldsymbol{du}\} = [\boldsymbol{N_u}]\{\dot{\widetilde{\boldsymbol{u}}}\}dt = [\boldsymbol{N_u}]\{\widetilde{\boldsymbol{du}}\} \tag{4.46}$$
$$\{[\![\boldsymbol{u}]\!]\} = [\boldsymbol{B}]\{\widetilde{\boldsymbol{u}}\};\quad \{[\![\boldsymbol{du}]\!]\} = [\boldsymbol{B}]\{\dot{\widetilde{\boldsymbol{u}}}\}dt = [\boldsymbol{B}]\{\widetilde{\boldsymbol{du}}\}$$

where $\{\widetilde{\boldsymbol{u}}\}$ and $\{\widetilde{\boldsymbol{du}}\}$ denote the nodal values of the respective variables, while $[\boldsymbol{N_u}]$ is an interpolation (shape) function, and $[\boldsymbol{B}]$ denotes a matrix relating the displacement jump to the nodal displacement. In the context of Newton-Raphson scheme, for $t : t^{(n)} \to t^{(n)} + \Delta t$ the following system of linear algebraic equations at iteration (i) is obtained by substituting Equation (4.46) into Equation (4.44)

$$\Big[\boldsymbol{K}\Big]^{(i)}\Big\{\widetilde{\boldsymbol{du}}\Big\} = \Big\{\boldsymbol{R_G}\Big\}^{(i)};\quad \Big\{\widetilde{\boldsymbol{u}}\Big\}^{(i+1)} = \Big\{\widetilde{\boldsymbol{u}}\Big\}^{(i)} + \Big\{\widetilde{\boldsymbol{du}}\Big\} \tag{4.47}$$

where

$$\Big\{\boldsymbol{R_G}\Big\}^{(i)} = -\int_{\partial_t^d\Omega}[\boldsymbol{B}]^T\{\boldsymbol{T}^D\}^{(i)}\ d\Gamma + \int_{\partial_t\Omega}[\boldsymbol{N_u}]^T\{\boldsymbol{T}^\star\}\ d\Gamma + \int_\Omega \rho[\boldsymbol{N_u}]^T\{\boldsymbol{g}\}\ d\Omega - \int_\Omega[\boldsymbol{LN_u}]^T\{\boldsymbol{\sigma'}\}^{(i)}\ d\Omega \tag{4.48}$$

$$\Big[\boldsymbol{K}\Big]^{(i)} = \int_\Omega[\boldsymbol{LN_u}]^T[\boldsymbol{D}][\boldsymbol{LN_u}]\ d\Omega + \int_{\partial_t^d\Omega}[\boldsymbol{B}]^T[\boldsymbol{S}]^{(i)}[\boldsymbol{B}]\ d\Gamma$$

In the expressions above, $[\boldsymbol{L}]$ is a matrix of the gradient operator specifying the kinematic strain-displacement relations. It should be noted that numerical integration in Equation (4.48) was carried out using Gaussian quadrature methods. The governing constitutive relations, viz. Equation (4.42), which incorporate a plasticity formulation, were integrated using an implicit scheme incorporating the cutting-plane algorithm for return-mapping (cf. [39]).

References

[1] B. Duevel and B. Haimson, "Mechanical characterization of pink Lac du bonnet granite: Evidence of nonlinearity and anisotropy," *International Journal of Rock Mechanics and Mining Sciences*, vol. 34, no. 3-4, pp. 117–e1, 1997.

[2] A. Al-Busaidi, J. Hazzard, and R. Young, "Distinct element modeling of hydraulically fractured lac du bonnet granite," *Journal of Geophysical Research: Solid Earth*, vol. 110, no. B6, 2005.

[3] A. Frampton and V. Cvetkovic, "Inference of field-scale fracture transmissivities in crystalline rock using flow log measurements," *Water Resources Research*, vol. 46, no. 11, 2010.

[4] L. Zou and V. Cvetkovic, "Inference of transmissivity in crystalline rock using

flow logs under steady-state pumping: Impact of multiscale heterogeneity," *Water Resources Research*, vol. 56, no. 8, 2020.

[5] W. Noll, "A mathematical theory of the mechanical behavior of continuous media," *Archive for Rational Mechanics and Analysis*, vol. 2, no. 1, pp. 197–226, 1958.

[6] R. de Borst and C. V. Verhoosel, "Damage, material instabilities, and failure," *Encyclopedia of Computational Mechanics Second Edition*, pp. 1–50, 2018.

[7] A. C. Eringen, *Microcontinuum Field Theories: I. Foundations and Solids*. Springer Science & Business Media, 2012.

[8] J. L. Mroginski, G. Etse, and S. M. Vrech, "A thermodynamical gradient theory for deformation and strain localization of porous media," *International Journal of Plasticity*, vol. 27, no. 4, pp. 620–634, 2011.

[9] M. E. Mobasher, L. Berger-Vergiat, and H. Waisman, "Non-local formulation for transport and damage in porous media," *Computer Methods in Applied Mechanics and Engineering*, vol. 324, pp. 654–688, 2017.

[10] H.-B. Mühlhaus and I. Vardoulakis, "The thickness of shear bands in granular materials," *Geotechnique*, vol. 37, no. 3, pp. 271–283, 1987.

[11] W. Ehlers and W. Volk, "On theoretical and numerical methods in the theory of porous media based on polar and non-polar elasto-plastic solid materials," *International Journal of Solids and Structures*, vol. 35, no. 34-35, pp. 4597–4617, 1998.

[12] H. Rattez, I. Stefanou, J. Sulem, M. Veveakis, and T. Poulet, "Numerical analysis of strain localization in rocks with thermo-hydro-mechanical couplings using

cosserat continuum," *Rock Mechanics and Rock Engineering*, vol. 51, no. 10, pp. 3295–3311, 2018.

[13] R. E. Goodman, R. L. Taylor, and T. L. Brekke, "A model for the mechanics of jointed rock," *Journal of the Soil Mechanics and Foundations Division, Proceedings of ASCE*, vol. 94, no. 3, pp. 637–659, 1968.

[14] J. Ghaboussi, E. L. Wilson, and J. Isenberg, "Finite element for rock joints and interfaces," *Journal of the Soil Mechanics and Foundations Division*, vol. 99, no. 10, pp. 833–848, 1973.

[15] M. C. Lobao, R. Eve, D. Owen, and E. A. de Souza Neto, "Modelling of hydrofracture flow in porous media," *Engineering Computations*, 2010.

[16] P. Fu, S. M. Johnson, and C. R. Carrigan, "An explicitly coupled hydro-geomechanical model for simulating hydraulic fracturing in arbitrary discrete fracture networks," *International Journal for Numerical and Analytical Methods in Geomechanics*, vol. 37, no. 14, pp. 2278–2300, 2013.

[17] N. Moës, J. Dolbow, and T. Belytschko, "A finite element method for crack growth without remeshing," *International Journal for Numerical Methods in Engineering*, vol. 46, no. 1, pp. 131–150, 1999.

[18] M. Luege, J. Lucero, C. Torrijos, and A. Orlando, "Coupled mechanical and fluid flow analysis in fractured saturated porous media using the xfem," *Applied Mathematical Modelling*, vol. 40, no. 7-8, pp. 4480–4504, 2016.

[19] E. Mikaeili and B. Schrefler, "XFEM, strong discontinuities and second-order work in shear band modeling of saturated porous media," *Acta Geotechnica*, vol. 13, no. 6, pp. 1249–1264, 2018.

[20] S. Pietruszczak and Z. Mróz, "Finite element analysis of deformation of strain-softening materials," *International Journal for Numerical Methods in Engineering*, vol. 17, no. 3, pp. 327–334, 1981.

[21] E. Haghighat and S. Pietruszczak, "On modeling of discrete propagation of localized damage in cohesive-frictional materials," *International Journal for Numerical and Analytical Methods in Geomechanics*, vol. 39, no. 16, pp. 1774–1790, 2015.

[22] S. Moallemi, S. Pietruszczak, and Z. Mróz, "Deterministic size effect in concrete structures with account for chemo-mechanical loading," *Computers & Structures*, vol. 182, pp. 74–86, 2017.

[23] A. A. Jameei and S. Pietruszczak, "Embedded discontinuity approach for coupled hydromechanical analysis of fractured porous media," *International Journal for Numerical and Analytical Methods in Geomechanics*, vol. 44, no. 14, pp. 1880–1902, 2020.

[24] A. A. Jameei and S. Pietruszczak, "On hydromechanical interaction during propagation of localized damage in rocks," *Minerals, Special Issue: The Hydro-Mechanics of Crystalline Rocks*, vol. 11, no. 2, p. 162, 2021.

[25] R. I. Borja, "On the mechanical energy and effective stress in saturated and unsaturated porous continua," *International Journal of Solids and Structures*, vol. 43, no. 6, pp. 1764–1786, 2006.

[26] C. D. Martin, *The strength of massive Lac du Bonnet granite around underground openings*. Ph.D. Thesis. University of Manitoba, Winnipeg, 1993.

[27] C. D. Martin, "Seventeenth Canadian Geotechnical Colloquium: The effect of

cohesion loss and stress path on brittle rock strength," *Canadian Geotechnical Journal*, vol. 34, no. 5, pp. 698–725, 1997.

[28] J. S. O. Lau and B. Gorski, "The post failure behaviour of Lac du bonnet grey granite. Divisional report MRL 91-079 (TR), CANMET," *Energy Mines and Resources, Ottawa, Canada*, 1991.

[29] S. Pietruszczak, J. Jiang, and F. A. Mirza, "An elastoplastic constitutive model for concrete," *International Journal of Solids and Structures*, vol. 24, no. 7, pp. 705–722, 1988.

[30] S. Pietruszczak, *Fundamentals of Plasticity in Geomechanics*. CRC Press, Taylor & Francis, Boca Raton, London, New York, Leiden, 2010.

[31] J.-F. Shao, K. T. Chau, and X. T. Feng, "Modeling of anisotropic damage and creep deformation in brittle rocks," *International Journal of Rock Mechanics and Mining Sciences*, vol. 43, no. 4, pp. 582–592, 2006.

[32] J. W. Rudnicki and J. R. Rice, "Conditions for the localization of deformation in pressure-sensitive dilatant materials," *Journal of the Mechanics and Physics of Solids*, vol. 23, no. 6, pp. 371–394, 1975.

[33] M. Veiskarami and M. M. Tamizdoust, "Bifurcation analysis in sands under true triaxial conditions with coaxial and noncoaxial plastic flow rules," *Journal of Engineering Mechanics*, vol. 143, no. 10, 2017.

[34] I. G. Vardoulakis and J. Sulem, *Bifurcation Analysis in Geomechanics*. Taylor & Francis, London and New York, 1995.

[35] S. Pietruszczak, "On homogeneous and localized deformation in water-infiltrated

soils," *International Journal of Damage Mechanics*, vol. 8, no. 3, pp. 233–253, 1999.

[36] R. W. Zimmerman and I.-W. Yeo, "Fluid flow in rock fractures: From the navier-stokes equations to the cubic law," *Dynamics of Fluids in Fractured Rock, Geophysical Monograph-American Geophysical Union*, vol. 122, pp. 213–224, 2000.

[37] J. A. White and R. I. Borja, "Stabilized low-order finite elements for coupled solid-deformation/fluid-diffusion and their application to fault zone transients," *Computer Methods in Applied Mechanics and Engineering*, vol. 197, no. 49-50, pp. 4353–4366, 2008.

[38] O. O. Zienkiewicz, A. H. C. Chan, M. Pastor, B. A. Schrefler, and T. Shiomo, *Computational Geomechanics with Special Reference to Earthquake Engineering*. John Wiley & Sons, New York, 1999.

[39] J. C. Simo and T. J. Hughes, *Computational Inelasticity*, vol. 7. Springer Science & Business Media, 2006.

[40] C. Han and I. G. Vardoulakis, "Plane-strain compression experiments on water-saturated fine-grained sand," *Geotechnique*, vol. 41, no. 1, pp. 49–78, 1991.

[41] S. Pietruszczak and M. Oulapour, "Assessment of dynamic stability of foundations on saturated sandy soils," *Journal of Geotechnical and Geoenvironmental Engineering*, vol. 125, no. 7, pp. 576–582, 1999.

[42] J. M. Segura and I. Carol, "Coupled HM analysis using zero-thickness interface elements with double nodes. Part I: Theoretical model," *International Journal for Numerical and Analytical Methods in Geomechanics*, vol. 32, no. 18, pp. 2083–2101, 2008.

Chapter 5

Conclusions

The CLED methodology developed in this thesis for dealing with discontinuities in saturated porous media is computationally efficient as it does not require the use of any additional degrees of freedom. The CLED approach enables the tracing of propagating cracks and also ensures that the solution does not display a pathological sensitivity to FE discretization.

In Chapter 2, an extended version of CLED approach has been developed applicable to coupled hydromechanical analysis of saturated porous media containing pre-existing and newly developing fractures. An equivalent hydraulic conductivity tensor was introduced, and it was mathematically proved that this tensor is symmetric. Implementation of this approach in the context of a finite element analysis was then provided. The solution was compared to the standard FE analysis that employed a very fine mesh together with interface elements (IE). It was demonstrated that the developed methodology is accurate enough to study the response involving the existence of discontinuities in the steady-state flow as well as consolidation problems. It was also shown that this approach is numerically efficient, and a relatively coarse mesh can be used to explicitly model the fractures. In addition, no special integration technique, other than the commonly known Gaussian quadrature, is required to calculate the stiffness operators.

In Chapter 3, the applicability of the proposed CLED approach to modeling tension cracks in the saturated rock-type materials was examined. An evolution law was introduced to describe the change in the equivalent hydraulic conductivity with continuing deformation in the localized regions. In order to verify the predictive abilities of this framework, the simulations of an axial 3D splitting test carried out on a saturated cylindrical sample were performed. The results showed an abrupt transition to brittle response after reaching the ultimate load, which was accompanied by the development of excessive lateral deformation. In the softening regime, an intense outflow flux was captured in the proximity of the localized regions triggered by the increase in permeability. In addition, in the softening range, a rapid dissipation of the excess pore-fluid pressure took place due to the volume expansion of the solid matrix along with the evolving permeability in the cracked regions. The results, in terms of the assessment of ultimate load, the fracture pattern, and the fluid transmissivity were in agreement with the experimental data, thus providing proof of concept in terms of the feasibility of the proposed approach. It should be noted that in the numerical simulations, no special algorithm for the discrete crack tracing was employed and, as a result, the cracks appeared as smeared over a narrow region.

The discrete crack tracing was studied in Chapter 4 which dealt with cracks propagation and coalescence in saturated crystalline rocks. A comprehensive CLED-FE formulation was developed which considered the change in the crack aperture during the ongoing localized damage in the weak statement of the problem. The numerical simulations in this chapter included uniaxial compression tests carried out on an elastoplastic Lac du Bonnet granite. Both single and multiple fractures were considered and the analysis included a dry sample, undrained deformation as well as the conditions of a progressive drainage. The results of the simulations were compared with those generated using a very fine mesh incorporating interface elements

(IE). It was demonstrated that the developed CLED-FE formulation is computationally efficient and accurate in relation to the IE approach. Moreover, it enables the tracing of a crack propagation, which cannot be efficiently done using the interface elements. It was observed that the response under undrained conditions was significantly affected by the type of flow rule, which impacted the rate of generation of the excess pore pressure. In this case, the load-deformation characteristic remained stable, and the most likely source of sample failure was cavitation. The analyses demonstrated that propagation of the macrocracks and their subsequent coalescence was more pronounced under drained rather than undrained regime. The simulations involving drainage under a sustained load showed a progressive increase in settlement triggered by dissipation of the pore pressure gradients. When the load intensity was above the ultimate value corresponding to the dry conditions, the drainage resulted in a rapid increase in the rate of settlement, which was indicative of a spontaneous loss of stability. In general, the numerical studies clearly demonstrated the predictive abilities of the CLED approach in assessing both the flow properties and the coupled HM response of crystalline rocks in the presence of both pre-existing and propagating fractures.

The approach proposed in this thesis can be used to model the response in the presence of discrete fracture networks and to study problems in which the flow characteristics at both meso and macroscales are of importance, e.g., flow around the deep geological repositories in fractured crystalline/sedimentary rocks. It should be noted that the numerical examples provided in this work involved smeared and discrete damage propagation in the 3D and 2D configurations, respectively. The 3D discrete damage propagation in saturated porous media can also be addressed by incorporating advanced tracing algorithms such as the level set methods. The current CLED framework can be enhanced to cover the unsaturated conditions, especially in cases where

fluid cavitation takes place during continuing deformation. In addition, the current CLED formulation can be extended to deal with thermo-hydro-mechanical problems involving the permafrost phenomena in the porous media, where the thawing-freezing cycles affect the propagation of damage in the frozen rocks. The formulation can also be extended to model the hydraulic fracturing. In this case, the traction exerted by the pressurized fluid to the surrounding porous matrix, and the fluid mass transfer must be considered in the extension of the present framework. The effect of the fracture roughness on the hydraulic conductivity can also be considered. Finally, problems such as calcification of salts in the fractured porous media during the transport of saline fluids and sealing of the fractures, can also be studied by using an enhanced form of the current approach.